

**DESIGN AND FABRICATION OF
QUASI-2D PHOTONIC CRYSTAL
COMPONENTS BASED ON
SILICON-ON-INSULATOR
TECHNOLOGY**

Cazimir Gabriel Bostan

The research described in this thesis was carried out at the Integrated Optical Microsystems (IOMS) Group, Faculty of Electrical Engineering, Mathematics and Computer Science, MESA⁺ Research Institute for Nanotechnology, University of Twente, P.O. Box 217, 7500 AE Enschede, The Netherlands.

This work was financially supported by the MESA⁺ Advanced Photonic Structures SRO for the first year and by the Dutch Technology Foundation (STW) for the last three years.

Cover: Free-standing silicon membrane with photonic crystal area of holes directly etched through it by focused ion beam; the projection of the holes onto the substrate is clearly observable.

Copyright © 2005 by Cazimir Gabriel Bostan, Enschede, The Netherlands

ISBN: 90-365-2155-6

**DESIGN AND FABRICATION OF
QUASI-2D PHOTONIC CRYSTAL
COMPONENTS BASED ON
SILICON-ON-INSULATOR
TECHNOLOGY**

PROEFSCHRIFT

ter verkrijging van
de graad van doctor aan de Universiteit Twente,
op gezag van de rector magnificus,
prof. dr. W. H. M. Zijm,
volgens besluit van de College voor Promoties
in het openbaar te verdedigen
op vrijdag 25 februari 2005 om 13.15 uur

door

Cazimir Gabriel Bostan

geboren op 14 augustus 1969

te Boekarest, Roemenië

Dit proefschrift is goedgekeurd door:

de promotor: prof. dr. A. Driessen

de assistant promotor: dr. ir. R. M. de Ridder

To my wife Diana

Contents

Preface.....	1
Chapter 1 Basic physical concepts of photonic crystals	3
1.1. Electromagnetic waves in inhomogeneous media	3
1.2. Properties of photonic crystals.....	7
1.2.1 Crystal lattice	7
1.2.2 Reciprocal lattice and First Brillouin Zone.....	9
1.2.3 Example: 2D triangular lattice.....	10
1.2.4 Bloch-Floquet theorem. Bloch waves.....	12
1.2.5 Photonic band structure and photonic bandgap	13
1.2.6 Symmetry and irreducible Brillouin zone.....	14
1.2.7 Example of band diagram	18
1.2.8 Density of states (DOS)	19
1.2.9 Group velocity (v_g)	20
1.2.10 Wave-vector diagram.....	21
1.2.11 Effective index.....	22
Chapter 2 Computational methods and modeling tools.....	23
2.1. Plane wave expansion method (PWEM)	23
2.1.1 Representation of dielectric function and convergence issues	24
2.1.2 Matrix eigenvalue problem.....	26
2.1.3 Variational formulation.....	28
2.2. Transfer matrix method (TMM)	30
2.3. Diffraction grating approach.....	30
2.4. Eigenmode expansion method (EME).....	32
2.5. Scattering matrix method (SMM).....	33
2.6. Multiple scattering technique (MST).....	35
2.7. Finite element method (FEM).....	35
2.8. Finite difference time-domain (FDTD)	36
2.9. Discussion.....	37
Chapter 3 Design of photonic crystals with 2D periodicity	39
3.1. Two-dimensional photonic crystals	41
3.1.1 Dielectric contrast and material choice.....	41
3.1.2 Filling factor	42
3.1.3 Rotation angle and vein thickness	43

3.1.4	Transmission through finite samples	45
3.2.	Photonic crystal slabs (PCSs)	47
3.2.1	Guiding mechanism	48
3.2.2	Light cone	48
3.2.3	Vertical supercell	49
3.2.4	Types of PCSs.....	50
3.2.5	Band diagrams of guided modes.....	52
3.2.6	Effective index approximation.....	55
3.2.7	Loss mechanisms	56
3.2.8	Discussion	57
 Chapter 4 Design of line-defect waveguides in photonic crystals....		59
4.1.	Waveguiding mechanisms	59
4.2.	Projected band diagram	60
4.3.	Lateral supercell approach to ‘defect’ modes	62
4.4.	Propagation phenomena in line defect waveguides.....	65
4.4.1	Index guiding	65
4.4.2	Crossings and anticrossings	65
4.4.3	Group velocity and transmission bandwidth	66
4.4.4	Out-of-plane radiation loss and quality factor	66
4.5.	Band diagram engineering.....	67
4.6.	Waveguides in hexagon-type photonic crystals.....	69
4.6.1	Two-dimensional calculations based on effective index approximation	69
4.6.2	Three-dimensional FDTD calculations of spectral transmittance	73
4.7.	Bends and Y-junctions.....	74
4.8.	Conclusions and discussion	76
 Chapter 5 Fabrication technologies for SOI photonic crystal components		79
5.1.	Overview of technologies	79
5.2.	Laser interference lithography (LIL)	80
5.2.1	Principle of LIL, design parameters and implementation.. ..	80
5.2.2	Fabrication processes and results.....	84
5.2.3	Possible further developments	88
5.3.	Reactive ion etching (RIE)	88
5.3.1	RIE mechanism for Si.....	89
5.3.2	RIE mechanism for SiO ₂	90
5.3.3	RIE experimental results.....	90
5.4.	Combining conventional lithography with focused ion beam (FIB)	93

5.4.1	Introduction.....	93
5.4.2	FIB milling parameters	95
5.4.3	Basic idea of our approach.....	98
5.4.4	Fabrication processes and results.....	99
5.5.	Discussion	102
Chapter 6 Preliminary characterization.....		105
6.1.	Experimental setup	105
6.2.	Experimental procedure and results.....	106
Chapter 7 Summary and conclusions		109
Samenvatting en conclusies.....		113
Appendix A Proof that $\hat{\Theta}_H$ operator is Hermitian		117
Appendix B Derivation of the PWEM eigenvalue equation		119
Appendix C Example of script used in simulations with MPB program		121
Appendix D Calculation of the dose absorbed in photoresist during the LIL process.....		123
Appendix E Fabrication processes		127
References.....		129
Acknowledgements		141

Preface

An intense research on photonic crystals has been going on during the last decade. In particular, quasi-2D photonic crystals, also known as photonic crystal slabs (PCS) have received a considerable interest as they have the potential to serve as an integration platform for densely packed photonic circuits. By introducing ‘defects’ in a PCS in a controlled manner, one is able to implement passive and active building blocks (e.g. filters [Villeneuve 1996], lasers [Noda 2001]). These can then be combined to form large-scale complex architectures.

In this thesis we consider telecom applications of line defect waveguides in PCS that should act as ‘light pipes’ for directional transmission of signals. What is the motivation of using PCS-based waveguides instead of conventional waveguides? In conventional slab-based waveguides the energy distribution has a tail extending into the claddings and waveguiding relies on ‘total internal reflection’ (TIR). When the waveguide turns a bend the TIR condition is broken and energy leaks away. On the other hand, in a PCS-based waveguide the lateral ‘walls’ are ‘metallic-like’ because the wave is strongly attenuated inside these walls for frequencies in the photonic bandgap (PBG). Consequently, sharp bends in PCS-based waveguides are, in principle possible, because in-plane radiation losses are suppressed.

Being the first PhD thesis on photonic crystals in the Integrated Optical Microsystems Group, the focus of this research is on design and fabrication of PCS-based integrated optical components in silicon-on-insulator substrates.

In Chapter 1 the basic physical concepts of photonic crystals are introduced, in order to aid understanding and interpretation of computational results and design rules.

Chapter 2 presents an overview of the most common computational methods and modeling tools applicable to the analysis and design of photonic crystals. The emphasis is put on strengths and weaknesses of each method. The calculation results and the design rules derived from them are presented in the following two chapters.

Chapter 3 contains applications of the theoretical framework and computational techniques from the previous two chapters. The representative results presented are interpreted in terms of design and optimization criteria of photonic crystals with 2D periodicity as function of geometrical parameters (e.g. filling factor, slab thickness). We introduce a new class of photonic crystals (called “hexagon-type”) that offers flexibility in adjusting the lattice configuration and provides a large PBG.

Chapter 4 contains a study of propagation phenomena in line defect waveguides and their impact on the device performance. After comparing different engineering solutions, we opted for a hybrid design (hexagonal holes plus triangular inclusions) in which the PhC waveguide resembles closely a ridge waveguide.

Preface

Chapter 5 contains fabrication results obtained using available technologies: laser interference lithography, reactive ion etching and focused ion beam.

Chapter 6 contains preliminary measurement results using end-fire coupling.

Five appendices, containing mathematical and technological details, complement the main chapters.

Chapter 1 Basic physical concepts of photonic crystals

At the time of writing of this thesis, there are two main books treating the basics of photonic crystals: *Photonic crystals: Molding the flow of light* by J. D. Joannopoulos, R. D. Meade and J. N. Winn [Joannopoulos 1995] and *Optical properties of photonic crystals* by K. Sakoda [Sakoda 2001]. These books are somewhat complementary. Joannopoulos and his co-workers wrote an intuitive introduction to the field, built around the parallel between solid-state physics and the physics of photonic crystals. On the other hand, Sakoda went deeper into the mathematical formalism associated with the physical phenomena, some chapters being quite difficult to follow due to the high level of abstraction.

In this chapter, the author tries to follow a middle way. That is, to present the basic concepts in an intuitive way, while sacrificing the mathematical rigor as little as possible. Main contributions of the author in this chapter are: (i) addition of intermediate steps in some derivations (e.g. equations (1.23), (1.55), (1.56)) that were found to be missing from the available literature; (ii) exemplification of the connection between the symmetry of the primitive cell and the irreducible Brillouin zone (Figure 1.3 and Figure 1.4).

1.1. Electromagnetic waves in inhomogeneous media

The propagation of electromagnetic waves in an arbitrary medium is described by the macroscopic Maxwell equations:

$$\vec{\nabla} \times \vec{E}(\vec{r}, t) = -\frac{\partial \vec{B}(\vec{r}, t)}{\partial t} \quad (1.1)$$

$$\vec{\nabla} \times \vec{H}(\vec{r}, t) = \vec{J}(\vec{r}, t) + \frac{\partial \vec{D}(\vec{r}, t)}{\partial t} \quad (1.2)$$

$$\vec{\nabla} \cdot \vec{D}(\vec{r}, t) = \rho(\vec{r}, t) \quad (1.3)$$

$$\vec{\nabla} \cdot \vec{B}(\vec{r}, t) = 0 \quad (1.4)$$

Regarding the material properties we make the following assumptions (they are considered valid throughout this thesis):

- There are no free charges nor currents: $\rho = 0$, $\vec{J} = 0$;
- The material is isotropic; then, the dielectric permittivity $\varepsilon(\vec{r}, \omega)$ is a scalar ;
- Material absorption and dispersion are negligible; then ε is real and frequency independent;

- The field intensity is low enough such that there is a linear relationship between \vec{D} and \vec{E} ;
- The material is non-magnetic; then the relative magnetic permeability is $\mu_r(\vec{r}) = 1$;

With all these assumptions, the constitutive equations connecting the field quantities with material properties become:

$$\vec{D}(\vec{r}, t) = \varepsilon_0 \varepsilon_r(\vec{r}) \vec{E}(\vec{r}, t) \quad (1.5)$$

$$\vec{B}(\vec{r}, t) = \mu_0 \vec{H}(\vec{r}, t) \quad (1.6)$$

where ε_0 and μ_0 are the properties of vacuum.

A well-known result from Fourier analysis states that any field solution can be expanded into a set of harmonic modes. Therefore, we consider harmonic waves with sinusoidal time dependence:

$$\vec{E}(\vec{r}, t) = \vec{E}(\vec{r}) e^{-i\omega t} \quad (1.7)$$

$$\vec{H}(\vec{r}, t) = \vec{H}(\vec{r}) e^{-i\omega t} \quad (1.8)$$

Maxwell equations for harmonic waves propagating in media with the properties described above become:

$$\vec{\nabla} \times \vec{E}(\vec{r}) = i\omega \mu_0 \vec{H}(\vec{r}) \quad (1.9)$$

$$\vec{\nabla} \times \vec{H}(\vec{r}) = -i\omega \varepsilon_0 \varepsilon_r(\vec{r}) \vec{E}(\vec{r}) \quad (1.10)$$

$$\vec{\nabla} \cdot (\varepsilon_r(\vec{r}) \vec{E}(\vec{r})) = 0 \quad (1.11)$$

$$\vec{\nabla} \cdot \vec{H}(\vec{r}) = 0 \quad (1.12)$$

Multiplying (1.10) by $\varepsilon_r^{-1}(\vec{r})$, taking the curl, and using (1.9) we obtain the following equation for the $\vec{H}(\vec{r})$ field:

$$\vec{\nabla} \times \left(\frac{1}{\varepsilon_r(\vec{r})} \vec{\nabla} \times \vec{H}(\vec{r}) \right) = \left(\frac{\omega}{c} \right)^2 \vec{H}(\vec{r}) \quad (1.13)$$

where $c = 1/\sqrt{\varepsilon_0 \mu_0}$ is the speed of light in vacuum.

A similar equation can be obtained for the $\vec{E}(\vec{r})$ field:

$$\frac{1}{\varepsilon_r(\vec{r})} \vec{\nabla} \times (\vec{\nabla} \times \vec{E}(\vec{r})) = \left(\frac{\omega}{c} \right)^2 \vec{E}(\vec{r}) \quad (1.14)$$

Using either (1.13) or (1.14) one can prove two important scaling laws in electromagnetism. They state that there is no absolute length scale and there is no fundamental value of the relative dielectric constant.

Suppose a compression or expansion of the original medium, that is a scale transformation $\vec{r}' = s\vec{r}$, $s \in \mathbb{R} \setminus \{0\}$. In the transformed medium we have:

$$\varepsilon_r(\vec{r}) = \varepsilon_r\left(\frac{\vec{r}'}{s}\right) = \varepsilon_r'(\vec{r}')$$

$$\vec{\nabla}' \equiv \frac{\partial}{\partial \vec{r}'} = \frac{1}{s} \vec{\nabla}$$

If we make the change of variables in (1.13) we obtain a new form of eigenvalue equation:

$$\vec{\nabla}' \times \left(\frac{1}{\varepsilon_r'(\vec{r}')} \vec{\nabla}' \times \vec{H}(\vec{r}'/s) \right) = \left(\frac{\omega}{sc} \right)^2 \vec{H}(\vec{r}'/s) \quad (1.15)$$

After changing the length scale by a factor 's', the mode profile and its eigenfrequency are scaled by the same factor: $\vec{H}'(\vec{r}') = \vec{H}(\vec{r}'/s)$ and $\omega' = \omega/s$. This result is of considerable practical importance. Experiments can be carried out in a frequency spectrum (e.g. microwave region) where practical realization is not hampered by technological limitations; then, the results for a smaller length scale (e.g. optical region) can be inferred.

Suppose that we scale down the magnitude of dielectric function by a factor 's²', i.e. $\varepsilon_r'(\vec{r}) = \varepsilon_r(\vec{r})/s^2$, in every point inside the medium, while keeping its spatial distribution unchanged. From (1.13) we obtain:

$$\vec{\nabla} \times \left(\frac{1}{\varepsilon_r(\vec{r})} \vec{\nabla} \times \vec{H}(\vec{r}) \right) = \left(\frac{s\omega}{c} \right)^2 \vec{H}(\vec{r}) \quad (1.16)$$

The spatial distribution of harmonic modes is unchanged, while the frequency is scaled up by a factor 's', $\omega' = s\omega$. The choice of scaling factor in this case is not arbitrary, being limited by the availability of materials in nature and processing technology.

In analogy with the formalism of quantum mechanics, equations (1.13) and (1.14) can be written in operator form:

$$\hat{\Theta}_H \vec{H}(\vec{r}) = \left(\frac{\omega}{c} \right)^2 \vec{H}(\vec{r})$$

$$\hat{\Theta}_E \vec{E}(\vec{r}) = \left(\frac{\omega}{c} \right)^2 \vec{E}(\vec{r}) \quad (1.17)$$

where

$$\hat{\Theta}_H = \vec{\nabla} \times \frac{1}{\varepsilon_r(\vec{r})} \vec{\nabla} \times$$

$$\hat{\Theta}_E = \frac{1}{\varepsilon_r(\vec{r})} \vec{\nabla} \times \vec{\nabla} \times \quad (1.18)$$

In the following sections, we develop the theory in terms of \vec{H} field rather than in terms of \vec{E} or \vec{D} fields based on the following arguments:

- (i) $\vec{H}(\vec{r})$ is transverse (see equation (1.12)); therefore, it is easier to eliminate one field component and reduce the dimensionality of the problem;
- (ii) the normal and longitudinal components of the magnetic field are continuous across the dielectric boundaries;
- (iii) the operator $\hat{\Theta}_H$ is Hermitian (see Appendix A for a detailed proof), whereas $\hat{\Theta}_E$ is not.

The fact that $\hat{\Theta}_H$ is Hermitian means that its eigenvalues are real and its eigenvectors form a complete and orthogonal set that can be normalized to unity.

We take the scalar product of both sides in first equation (1.17) with $\vec{H}(\vec{r})$ (this amounts to multiplication to the left by $\vec{H}^*(\vec{r})$ and integration over space):

$$\langle \vec{H}(\vec{r}), \hat{\Theta}_H \vec{H}(\vec{r}) \rangle = \int d^3r \vec{H}^*(\vec{r}) \cdot \hat{\Theta}_H \vec{H}(\vec{r}) = \left(\frac{\omega}{c}\right)^2 \int d^3r |\vec{H}(\vec{r})|^2 \quad (1.19)$$

Using the vector identity (A1) from Appendix A, we obtain:

$$\begin{aligned} \vec{H}^*(\vec{r}) \cdot \left(\vec{\nabla} \times \frac{1}{\varepsilon_r(\vec{r})} \vec{\nabla} \times \vec{H}(\vec{r}) \right) &= \frac{1}{\varepsilon_r(\vec{r})} (\vec{\nabla} \times \vec{H}(\vec{r})) \cdot (\vec{\nabla} \times \vec{H}^*(\vec{r})) \\ &\quad - \vec{\nabla} \cdot \left(\vec{H}^*(\vec{r}) \times \frac{1}{\varepsilon_r(\vec{r})} (\vec{\nabla} \times \vec{H}(\vec{r})) \right) \end{aligned} \quad (1.20)$$

By a similar argument to that presented in Appendix A, it can be shown that the contribution of the second term in the right hand side of (1.20) to the scalar product integral vanishes. Then, using (1.20) in (1.19) we obtain:

$$\int d^3r \frac{1}{\varepsilon_r(\vec{r})} |\vec{\nabla} \times \vec{H}(\vec{r})|^2 = \left(\frac{\omega}{c}\right)^2 \int d^3r |\vec{H}(\vec{r})|^2 \quad (1.21)$$

For $\varepsilon_r(\vec{r}) > 0$ (as is usually the case in dielectrics and semiconductors at optical frequencies) the integrand in the left hand side of (1.21) is positive and this implies $\omega^2 > 0$, i.e. the eigenfrequencies are real. The positive and negative roots correspond to physically equivalent states, therefore we will take into consideration the positive roots only.

Equation (1.21) can be expressed in terms of electromagnetic energy functional (E_f):

$$E_f = \frac{1}{2} \frac{\int d^3r \frac{1}{\varepsilon_r(\vec{r})} |\vec{\nabla} \times \vec{H}(\vec{r})|^2}{\int d^3r |\vec{H}(\vec{r})|^2} = \frac{1}{2} \left(\frac{\omega}{c}\right)^2 \quad (1.22)$$

The *variational theorem* in electromagnetism ([Joannopoulos 1995] p.16) states that E_f is stationary with respect to variations of H field, then:

$$\delta E_f = \underbrace{\frac{\partial E_f}{\partial H} \delta H}_{=0} + \frac{\partial E_f}{\partial \varepsilon_r} \delta \varepsilon_r = \frac{\partial E_f}{\partial \varepsilon_r} \delta \varepsilon_r \quad (1.23)$$

Therefore, by applying (1.23) in (1.22) we obtain succesively:

$$\delta E_f = \frac{1}{2} \frac{\int d^3 r \delta \left(\frac{1}{\varepsilon_r(\vec{r})} \right) |\vec{\nabla} \times \vec{H}(\vec{r})|^2}{\int d^3 r |\vec{H}(\vec{r})|^2} = \frac{1}{2} \delta \left(\frac{\omega}{c} \right)^2 \quad (1.24)$$

$$\frac{2\omega}{c^2} \delta \omega \int d^3 r |\vec{H}(\vec{r})|^2 = - \int d^3 r \left| \frac{1}{\varepsilon_r(\vec{r})} (\vec{\nabla} \times \vec{H}(\vec{r})) \right|^2 \delta \varepsilon_r(\vec{r}) \quad (1.25)$$

From (1.25) one can see that if we change the amount of dielectric by $\delta \varepsilon_r$, this leads to a shift in frequency $\delta \omega$. The variations $\delta \varepsilon_r$ and $\delta \omega$ have opposite signs. We will revert to this result in Chapter 4, when discussing “defects” in photonic crystals.

1.2. Properties of photonic crystals

1.2.1 Crystal lattice

A photonic crystal is built of a basic block (*unit cell*) repeated infinitely and periodically in space, without overlapping itself or leaving voids. The spatial arrangement of the unit cell is a lattice with *discrete translational symmetry*. The periodicity means that there exist some basis vectors, such that the structure remains invariant under translation by any vector that is a linear superposition of these vectors. The choice of basis vectors is not unique. Among the possible sets, one can find a subset of *primitive vectors* $\{\vec{a}_1, \vec{a}_2, \vec{a}_3\}$ which are the basis vectors with the smallest modulus. An arbitrary lattice site can be defined as origin of the coordinate system. The *lattice vector* connecting the origin with the l^{th} lattice site is:

$$\vec{R}_l = l_1 \vec{a}_1 + l_2 \vec{a}_2 + l_3 \vec{a}_3, \quad l = (l_1, l_2, l_3) \in \mathbb{Z}^3 \quad (1.26)$$

The dielectric permittivity is in general a piecewise constant function, spatially periodic modulo \vec{R}_l :

$$\varepsilon(\vec{r}) = \varepsilon(\vec{r} + \vec{R}_l), \quad \forall \vec{R}_l \quad (1.27)$$

In order to construct the full photonic crystal, we have to specify the characteristics of a single unit cell: dimension, shape, dielectric constant and position within the unit cell of the “atoms”. The choice of unit cell is not

unique and, depending on it, the set of lattice vectors can be complete or not. Three unit cell examples for a two-dimensional (2D) triangular lattice of hexagonal “atoms” are shown in Figure 1.1 .

The *primitive cell* has the smallest possible volume and, regardless the choice of primitive vectors, this volume is:

$$\Omega = \vec{a}_1 \cdot (\vec{a}_2 \times \vec{a}_3) \quad (1.28)$$

Two examples of primitive cells, containing a single “atom”, are (b) and (c) in Figure 1.1. However, there is a difference between them: cell (b) does not display the full symmetry of the lattice considered (does not have 60° rotation symmetry), whereas cell (c) does.

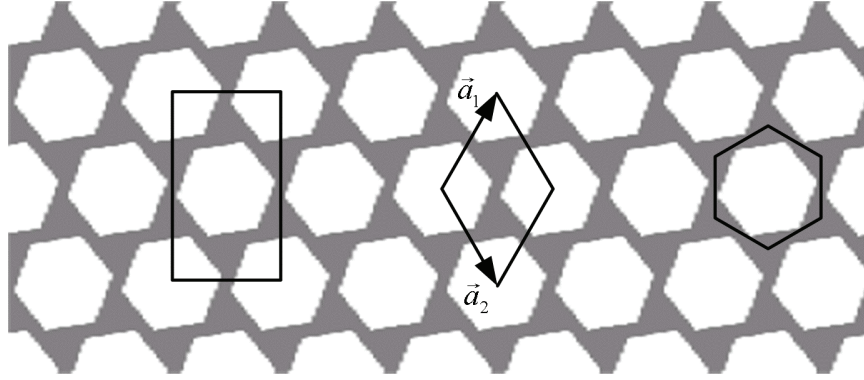


Figure 1.1 Three possible choices of unit cell in a 2D lattice: (a) rectangular unit cell containing two “atoms” (left); (b) rhombus subtended by the primitive vectors (center); (c) primitive Wigner-Seitz cell (right) – see text for details

The rectangular unit cell (Figure 1.1a) is applicable in calculations that rely on a rectangular discretization grid (e.g. standard FDTD, see Chapter 2). Care must be taken in deriving the correct band diagram, because the bands are folded due to the fact that the unit cell contains two “atoms” (this issue will be addressed in Chapter 4).

The rhombus subtended by the primitive vectors (Figure 1.1b) is useful mainly for calculating the volume of the primitive cell.

The Wigner-Seitz primitive cell is the most important choice of unit cell. It is closely related to the basic concept of First Brillouin Zone (1BZ), discussed in the next section. The construction of the Wigner-Seitz cell is the same as the one for 1BZ: we draw perpendicular bisector planes from the chosen lattice point to the nearest equivalent lattice sites. Each bisector plane divides the lattice into half-planes, one of which contains the chosen lattice point. The intersection of all the half-planes that contain the chosen lattice point is the Wigner-Seitz cell.

The position vector inside the Wigner-Seitz cell has a continuous variation:

$$\vec{r} = r_1 \vec{a}_1 + r_2 \vec{a}_2 + r_3 \vec{a}_3, \quad |r_i| \leq 0.5 \quad (1.29)$$

and it is a fractional combination of primitive vectors.

Usually, the primitive cell contains one “atom” which is centered at the lattice site. Sometimes there are several atoms per primitive cell and in this case the lattice is called a *lattice with a basis* (one example is the graphite structure, discussed by Cassagne et al. [Cassagne 1996]).

Suppose a *binary* photonic crystal that consists of two materials: a background material with bulk dielectric constant ε_b and a periodical arrangement of identical “atoms” with bulk dielectric constant ε_a . The shape of “atoms” is described by a function of position: $S(\vec{r}) = 1$ if \vec{r} lies inside the “atom” and $S(\vec{r}) = 0$ elsewhere, distributed periodically at lattice points \vec{R}_l . The dielectric constant at an arbitrary point inside the photonic crystal can be expressed mathematically as:

$$\varepsilon(\vec{r}) = \varepsilon_b + (\varepsilon_a - \varepsilon_b) \sum_l S(\vec{r} - \vec{R}_l) \quad (1.30)$$

This thesis focuses on single-atom binary photonic crystals.

1.2.2 Reciprocal lattice and First Brillouin Zone

Since the dielectric function is periodic (see (1.27)), it can be expanded in Fourier series using a plane wave basis $e^{i\vec{G}\cdot\vec{r}}$:

$$\varepsilon(\vec{r}) = \sum_{\vec{G}} \varepsilon_{\vec{G}} e^{i\vec{G}\cdot\vec{r}} \quad (1.31)$$

It can be shown (see e.g. [Joannopoulos 1995] p.113) that only terms that satisfy

$$e^{i\vec{G}_m \cdot \vec{R}_l} = 1 \Leftrightarrow \vec{G}_m \cdot \vec{R}_l = 2\pi p, \quad p \in \mathbb{Z} \quad (1.32)$$

are contributing to the Fourier series, \vec{R}_l being expressed in (1.26).

The wave vectors \vec{G}_m form a lattice of their own, called *reciprocal lattice*. This lattice can be generated by a set of primitive vectors $\{\vec{b}_1, \vec{b}_2, \vec{b}_3\}$. Similar to the case of crystal lattice, the vectors from the origin to the m^{th} node of the reciprocal lattice have the form:

$$\vec{G}_m = m_1 \vec{b}_1 + m_2 \vec{b}_2 + m_3 \vec{b}_3, \quad m = (m_1, m_2, m_3) \in \mathbb{Z}^3 \quad (1.33)$$

The requirement (1.32) can be fulfilled if:

$$\vec{a}_i \cdot \vec{b}_j = 2\pi \delta_{ij}, \quad \delta_{ij} = \begin{cases} 1, & i = j \\ 0, & i \neq j \end{cases} \quad (1.34)$$

The reciprocal lattice can be generated by the following primitive vectors:

$$\vec{b}_1 = \frac{2\pi}{\Omega} (\vec{a}_2 \times \vec{a}_3), \quad \vec{b}_2 = \frac{2\pi}{\Omega} (\vec{a}_3 \times \vec{a}_1), \quad \vec{b}_3 = \frac{2\pi}{\Omega} (\vec{a}_1 \times \vec{a}_2) \quad (1.35)$$

where Ω is the volume of the primitive cell of the crystal lattice, expressed in (1.28).

The primitive cell of the reciprocal space has a volume $\Omega' = \vec{b}_1 \cdot (\vec{b}_2 \times \vec{b}_3)$ that is related to Ω by:

$$\Omega' = \frac{(2\pi)^3}{\Omega} \quad (1.36)$$

From their definitions, we see that crystal and reciprocal lattices are essentially inverses of each other: lattice basis vectors have dimension of length, while reciprocal lattice basis vectors have dimension of inverse length. Therefore, vectors \vec{b}_j provide a natural basis for wave vectors when analyzing the propagation of electromagnetic waves in photonic crystals.

The primitive Wigner-Seitz cell of the reciprocal lattice is called *First Brillouin Zone (1BZ)*; its construction has been described in detail in the previous section. In 1BZ we cannot get from any point to another by adding any \vec{G}_m . By tiling the 1BZ with all vectors \vec{G}_m one can construct the full reciprocal lattice. However, the points belonging to different Brillouin zones are physically equivalent (they have the same eigenfrequencies and eigenmodes, as shown in the section 1.2.4). In other words, the 1BZ is the polyhedron with the smallest volume in the reciprocal space that contains *all* possible (non-redundant) states of electromagnetic field in an *infinite* photonic crystal.

A generic wave vector inside 1BZ is a fractional superposition of reciprocal space primitive vectors:

$$\vec{k} = k_1 \vec{b}_1 + k_2 \vec{b}_2 + k_3 \vec{b}_3, \quad |k_j| \leq 0.5 \quad (1.37)$$

Different \vec{k} vectors in 1BZ lead, in general, to different field eigenvectors. Therefore, in what follows, we will add a label \vec{k} to the field solutions, i.e. $\vec{H}_{\vec{k}}(\vec{r})$.

1.2.3 Example: 2D triangular lattice

We illustrate the concepts discussed so far by an example that will constitute the main subject of this thesis. Indeed, even the physics of 3D slabs (see Chapter 3) is based upon the 2D triangular lattice.

We consider a 2D lattice spanned by two vectors with equal magnitude $|\vec{a}_1| = |\vec{a}_2| = a$ and having a 60° angle between them. The parameter ' a ' is called *lattice constant*, and represents the distance between a lattice point and its closest neighbor.

The primitive vectors of the crystal lattice are chosen as to fulfill inversion symmetry (see section 1.2.6) :

$$\begin{aligned}\vec{a}_1 &= a(\sqrt{3}/2, 1/2) \\ \vec{a}_2 &= a(\sqrt{3}/2, -1/2)\end{aligned}\tag{1.38}$$

For a 2D lattice the volume of the primitive cell reduces to the area of the parallelogram subtended by the primitive vectors, $\Omega^{2D} = |\vec{a}_1 \times \vec{a}_2|$.

The calculation of the primitive vectors of the reciprocal lattice leads to:

$$\begin{aligned}\vec{b}_1 &= (4\pi/a\sqrt{3})(1/2, \sqrt{3}/2) \\ \vec{b}_2 &= (4\pi/a\sqrt{3})(1/2, -\sqrt{3}/2)\end{aligned}\tag{1.39}$$

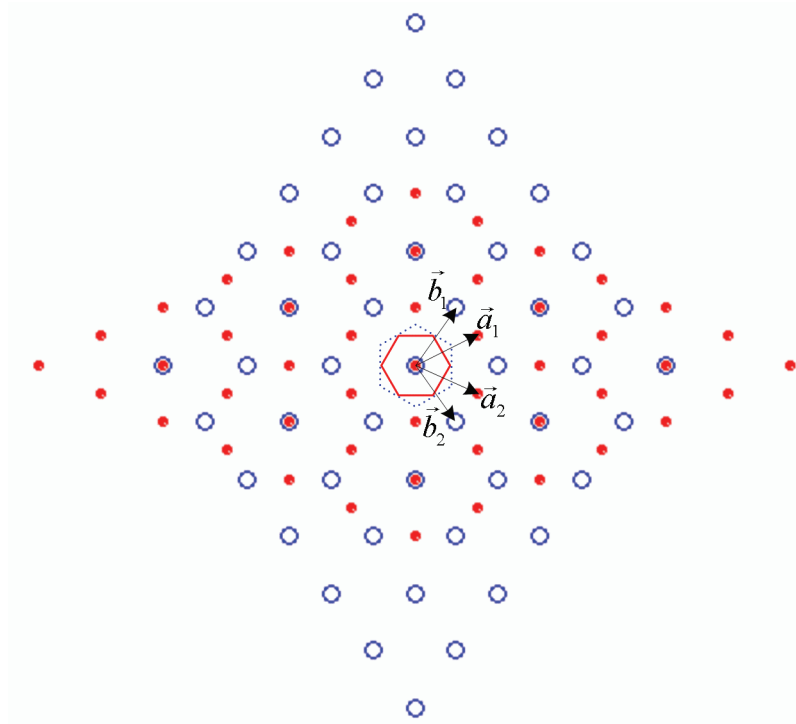


Figure 1.2 Illustration of the overlap between a triangular crystal lattice (solid circles) and Wigner-Seitz cell (solid line hexagon), with reciprocal lattice (open circles) and 1BZ (dotted line hexagon); For the sake of clarity, the crystal lattice has been scaled by 'a', and the reciprocal lattice has been scaled by $2\pi/a$

In order to clarify the scaling and orientation relationship between the crystal lattice and the reciprocal lattice, we plot them in the same figure (see Figure 1.2).

1.2.4 Bloch-Floquet theorem. Bloch waves

Both operators $\hat{\Theta}_H$ and $\hat{\Theta}_E$ in equation (1.18) are invariant under translation by lattice vectors* (e.g. $\hat{\Theta}_H(\vec{r} + \vec{R}) = \hat{\Theta}_H(\vec{r})$), because the spatial derivatives do not change, and $\varepsilon(\vec{r})$ is periodic.

We consider a *translation operator* $\hat{T}_{\vec{R}}$ acting upon a function of position:

$$\hat{T}_{\vec{R}} f(\vec{r}) = f(\vec{r} + \vec{R}) \quad (1.40)$$

(f can be a scalar or vector function)

We show that operators $\hat{\Theta}_H$ and $\hat{T}_{\vec{R}}$ commute:

$$\begin{aligned} \hat{T}_{\vec{R}} \hat{\Theta}_H(\vec{r}) \vec{H}_{\vec{k}}(\vec{r}) &= \hat{\Theta}_H(\vec{r} + \vec{R}) \vec{H}_{\vec{k}}(\vec{r} + \vec{R}) = \\ &= \hat{\Theta}_H(\vec{r}) \vec{H}_{\vec{k}}(\vec{r} + \vec{R}) = \hat{\Theta}_H(\vec{r}) \hat{T}_{\vec{R}} \vec{H}_{\vec{k}}(\vec{r}) \end{aligned} \quad (1.41)$$

thus they share the same eigenvectors $\vec{H}_{\vec{k}}(\vec{r})$.

The translation operators satisfy the composition law $\hat{T}_{\vec{R}} \hat{T}_{\vec{R}'} = \hat{T}_{\vec{R} + \vec{R}'}$, which means that the eigenvalues of $\hat{T}_{\vec{R}}$ should have an exponential form:

$$\hat{T}_{\vec{R}} \vec{H}_{\vec{k}}(\vec{r}) = e^{i\vec{k} \cdot \vec{R}} \vec{H}_{\vec{k}}(\vec{r}) \quad (1.42)$$

From equations (1.42) and (1.40) we obtain the *Bloch-Floquet theorem* in mathematical form:

$$\vec{H}_{\vec{k}}(\vec{r} + \vec{R}) = e^{i\vec{k} \cdot \vec{R}} \vec{H}_{\vec{k}}(\vec{r}) \quad (1.43)$$

Physically, equation (1.43) states that the electromagnetic field changes only by a phase factor when propagating from one unit cell of the crystal lattice to another. There is an equivalent formulation of the Bloch-Floquet theorem: the eigensolutions of partial differential equation (1.13), with periodic coefficients, may be expressed as a product of a plane wave and a lattice-periodic function:

$$\begin{aligned} \vec{H}_{\vec{k}}(\vec{r}) &= e^{i\vec{k} \cdot \vec{r}} \vec{h}_{\vec{k}}(\vec{r}) \\ \vec{h}_{\vec{k}}(\vec{r}) &= \vec{h}_{\vec{k}}(\vec{r} + \vec{R}) \end{aligned} \quad (1.44)$$

In (1.44) \vec{k} is the Bloch vector which belongs to the 1BZ, $\exp(i\vec{k} \cdot \vec{r})$ is a plane wave and $\vec{h}_{\vec{k}}(\vec{r})$ is a lattice-periodic field, completely defined by its values in the unit cell. The fields expressed in (1.43) and (1.44) are *Bloch waves* and represent the normal modes of photonic crystals (like plane waves are normal modes of homogeneous media). Bloch waves form a complete set of

* From this point forward, we omit the subscripts l and m for vectors belonging to crystal and reciprocal lattice, respectively

orthonormal functions and they provide a basis for expanding the field inside photonic crystals.

It is worth noting that the Bloch-Floquet theorem does not restrict \vec{k} to be real. In an infinite lattice \vec{k} has to be real, because only non-divergent field solutions should exist, but this constraint is removed if a surface is introduced.

An important property of the Bloch waves (already hinted at in the section about 1BZ) is that the fields corresponding to wave vectors that differ by a reciprocal lattice vector are identical. Taking a wave vector $\vec{k}' = \vec{k} + \vec{G}$, from (1.43) we obtain:

$$\vec{H}_{\vec{k}'}(\vec{r} + \vec{R}) = e^{i(\vec{k} + \vec{G}) \cdot \vec{R}} \vec{H}_{\vec{k}'}(\vec{r}) = e^{i\vec{k} \cdot \vec{R}} \vec{H}_{\vec{k}'}(\vec{r}) \quad (1.45)$$

($e^{i\vec{G} \cdot \vec{R}} = 1$, see (1.32)). In conclusion, $\vec{H}_{\vec{k}'}(\vec{r})$ satisfies the Bloch-Floquet theorem with wave vector \vec{k} , and states corresponding to \vec{k} and \vec{k}' are equivalent.

By inserting the Bloch wave expression (1.44) into (1.13) we obtain an eigenvalue problem defined over a domain containing a single primitive cell:

$$(\vec{\nabla} + i\vec{k}) \times \left\{ \frac{1}{\epsilon_r(\vec{r})} (\vec{\nabla} + i\vec{k}) \times \vec{h}_{n\vec{k}}(\vec{r}) \right\} = \left(\frac{\omega_{n\vec{k}}}{c} \right)^2 \vec{h}_{n\vec{k}}(\vec{r}) \quad (1.46)$$

with periodic condition $\vec{h}_{n\vec{k}}(\vec{r}) = \vec{h}_{n\vec{k}}(\vec{r} + \vec{R})$.

The eigenvalues form a discrete spectrum (because the volume Ω is finite) and they are labeled by a *band index* "n". The operator acting upon $\vec{h}_{n\vec{k}}$:

$$\hat{\Theta}_{n\vec{k}} = (\vec{\nabla} + i\vec{k}) \times \frac{1}{\epsilon_r(\vec{r})} (\vec{\nabla} + i\vec{k}) \times \quad (1.47)$$

is Hermitian, being derived from $\hat{\Theta}_H$.

Bloch modes are the eigenmodes of photonic crystals. Their propagation direction is definite (given by the direction of *group velocity*) despite the presence of scattering. Photonic Bloch waves can be viewed as stable superpositions of many plane waves having different reciprocal vectors. The resulting electromagnetic energy distribution of Bloch waves matches the periodicity of the lattice.

1.2.5 Photonic band structure and photonic bandgap

In the eigenvalue problem (1.46) the wave vector \vec{k} enters as a parameter that has a continuous variation in the 1BZ. Then, it is expected that each band frequency $\omega_{n\vec{k}}$ (with constant n) is a continuous function of \vec{k} . These band functions are labeled in order of increasing frequency by the band index n . The full set of band functions (dispersion relations) represents the *photonic band structure* of the photonic crystal. In principle, the photonic band structure does

not have an upper bound frequency, so the set is infinite. However, in practice, one is interested in the few lowest order bands (see Chapter 3).

In some cases, it can happen that a range of frequencies is not covered by *any* band function, for *all* \vec{k} and *all* polarization states. This is called a *photonic bandgap* (PBG) and it represents the main concept of photonic crystals.

One remaining question is how to choose appropriate representative \vec{k} points to sample its continuous space? We have to keep in mind two aspects: (i) not to miss some important features of the photonic band structure (e.g. maxima or minima of bands); (ii) to avoid redundant calculations. We will address these issues in the next section.

1.2.6 Symmetry and irreducible Brillouin zone

We will discuss first the *time inversion symmetry* and its consequence. Consider $(\vec{E}_{n\vec{k}}, \vec{H}_{n\vec{k}})$ a solution of Maxwell's equations with real and positive definite frequency $\omega_{n\vec{k}} > 0$. Taking the complex conjugate of the curl equations (1.9) and (1.10):

$$\vec{\nabla} \times \vec{E}_{n\vec{k}}^*(\vec{r}) = -i\omega_{n\vec{k}}\mu_0\vec{H}_{n\vec{k}}^*(\vec{r}) \quad (1.48)$$

$$\vec{\nabla} \times \vec{H}_{n\vec{k}}^*(\vec{r}) = i\omega_{n\vec{k}}\varepsilon_0\varepsilon_r(\vec{r})\vec{E}_{n\vec{k}}^*(\vec{r}) \quad (1.49)$$

we notice that $(\vec{E}_{n\vec{k}}^*, -\vec{H}_{n\vec{k}}^*)$ is also a solution with the same frequency $\omega_{n\vec{k}}$.

Adopting a standard phase convention¹ [Bhat 2001]:

$$\vec{E}_{n\vec{k}}^*(\vec{r}) = \vec{E}_{n(-\vec{k})}(\vec{r}) \quad (1.50)$$

$$-\vec{H}_{n\vec{k}}^*(\vec{r}) = \vec{H}_{n(-\vec{k})}(\vec{r}) \quad (1.51)$$

we get that states corresponding to wave-vectors \vec{k} and $-\vec{k}$ are equivalent (i.e. $\omega_{n(-\vec{k})} = \omega_{n\vec{k}}$), *regardless* the lattice symmetry. For an *arbitrary* lattice, therefore, we need to consider only *half* of the first Brillouin zone.

Now, we refer to the spatial symmetries of the crystal lattice. A detailed treatment of spatial symmetry should be based on group theory. However, this is beyond the scope of this thesis. Instead we will present the symmetry intuitively through some examples and we will underline its consequences on the design of photonic crystals.

So far, we have discussed discrete translational symmetry. Besides this, the unit cell itself is often invariant under a set of transformations (e.g. rotation, mirror-reflection, inversion) defined with respect to the point of highest

¹ This stems from the fact that \vec{E} and \vec{H} fields are odd and even, respectively, under a space inversion)

symmetry of the photonic crystal. These transformations that leave the dielectric function unchanged *within the unit cell* form the so-called ‘point group’. Here, we consider only “atoms” with an inversion center that coincides with the center of Wigner-Seitz (WS) cell; this is the point with the highest symmetry.

Let $\hat{\mathfrak{R}}$ be a rotation operator that transforms a lattice vector into another one. The invariance of $\varepsilon(\vec{r})$ under $\hat{\mathfrak{R}}$ is expressed mathematically as:

$$\varepsilon(\hat{\mathfrak{R}}\vec{r}) = \varepsilon(\vec{r}) = \varepsilon(\hat{\mathfrak{R}}^{-1}\vec{r}) \quad (1.52)$$

A rotation operator $\hat{O}_{\mathfrak{R}}$ acting upon a vector field is composed of two rotations, of the field and of its argument. For example, the rotator of the $\vec{H}_{\vec{k}}(\vec{r})$ field is defined by ([Joannopoulos 1995] p.33):

$$\hat{O}_{\mathfrak{R}}\vec{H}_{\vec{k}}(\vec{r}) = \hat{\mathfrak{R}}\vec{H}_{\vec{k}}(\hat{\mathfrak{R}}^{-1}\vec{r}) \quad (1.53)$$

If $\hat{O}_{\mathfrak{R}}$ leaves the system invariant (rotational symmetry), it can be shown ([Sakoda 2001] p.63) by direct calculation that operators $\hat{O}_{\mathfrak{R}}$ and $\hat{\Theta}_H$ commute, thus:

$$\hat{\Theta}_H(\hat{O}_{\mathfrak{R}}\vec{H}_{\vec{k}}(\vec{r})) = \hat{O}_{\mathfrak{R}}(\hat{\Theta}_H\vec{H}_{\vec{k}}(\vec{r})) = \left(\frac{\omega_{\vec{k}}}{c}\right)^2 (\hat{O}_{\mathfrak{R}}\vec{H}_{\vec{k}}(\vec{r})) \quad (1.54)$$

As a consequence of this commutation relationship, any eigenmode of $\hat{\Theta}_H$ is an eigenmode of $\hat{O}_{\mathfrak{R}}$ as well. This is very convenient, since eigenfunctions and eigenvalues of simple symmetry operators are easily determined, whereas those of $\hat{\Theta}_H$ are not.

Equation (1.54) implies that the rotated field $\hat{O}_{\mathfrak{R}}\vec{H}_{\vec{k}}(\vec{r})$ is an eigenmode of (1.17) with the same eigenfrequency as $\vec{H}_{\vec{k}}(\vec{r})$, i.e. $\vec{H}_{\vec{k}}(\vec{r})$ and $\hat{O}_{\mathfrak{R}}\vec{H}_{\vec{k}}(\vec{r})$ are degenerate (note that they are not necessarily orthogonal).

Moreover, $\hat{O}_{\mathfrak{R}}\vec{H}_{\vec{k}}(\vec{r})$ is an eigenmode with the wave vector $\hat{\mathfrak{R}}^{-1}\vec{k}$, as shown in detail below. Recall the actions of translation operator (1.40) and field rotator (1.53). Then:

$$\hat{T}_{\vec{R}}(\hat{O}_{\mathfrak{R}}\vec{H}_{\vec{k}}(\vec{r})) = \hat{T}_{\vec{R}}(\hat{\mathfrak{R}}\vec{H}_{\vec{k}}(\hat{\mathfrak{R}}^{-1}\vec{r})) = \hat{\mathfrak{R}}\vec{H}_{\vec{k}}(\hat{\mathfrak{R}}^{-1}\vec{r} + \vec{R}) \quad (1.55)$$

$$\hat{O}_{\mathfrak{R}}(\hat{T}_{\hat{\mathfrak{R}}\vec{R}}\vec{H}_{\vec{k}}(\vec{r})) = \hat{O}_{\mathfrak{R}}\vec{H}_{\vec{k}}(\vec{r} + \hat{\mathfrak{R}}\vec{R}) = \hat{\mathfrak{R}}\vec{H}_{\vec{k}}(\hat{\mathfrak{R}}^{-1}\vec{r} + \vec{R}) \quad (1.56)$$

which means $\hat{T}_{\vec{R}}(\hat{O}_{\mathfrak{R}}\vec{H}_{\vec{k}}(\vec{r})) = \hat{O}_{\mathfrak{R}}(\hat{T}_{\hat{\mathfrak{R}}\vec{R}}\vec{H}_{\vec{k}}(\vec{r}))$. By using this result, equation (1.42) and the scalar product property $\vec{v} \cdot \hat{\mathfrak{R}}\vec{w} = \hat{\mathfrak{R}}^{-1}\vec{v} \cdot \vec{w}$, we get:

$$\hat{O}_{\mathfrak{R}}(\hat{T}_{\hat{\mathfrak{R}}\vec{R}}\vec{H}_{\vec{k}}(\vec{r})) = e^{i\vec{k} \cdot \hat{\mathfrak{R}}\vec{R}} (\hat{O}_{\mathfrak{R}}\vec{H}_{\vec{k}}(\vec{r})) = e^{i\hat{\mathfrak{R}}^{-1}\vec{k} \cdot \vec{R}} (\hat{O}_{\mathfrak{R}}\vec{H}_{\vec{k}}(\vec{r})) \quad (1.57)$$

$$\hat{T}_{\vec{R}} \left(\hat{O}_{\mathfrak{R}} \vec{H}_{\vec{k}}(\vec{r}) \right) = e^{i\mathfrak{R}^{-1}\vec{k} \cdot \vec{R}} \left(\hat{O}_{\mathfrak{R}} \vec{H}_{\vec{k}}(\vec{r}) \right) \quad (1.58)$$

Equation (1.58) proves that $\hat{O}_{\mathfrak{R}} \vec{H}_{\vec{k}}(\vec{r})$ is an eigenmode of the translation operator $\hat{T}_{\vec{R}}$ with eigenvalue $\exp(i\mathfrak{R}^{-1}\vec{k} \cdot \vec{R})$, thus $\hat{O}_{\mathfrak{R}} \vec{H}_{\vec{k}}(\vec{r})$ has the wave vector $\mathfrak{R}^{-1}\vec{k}$. Then the eigenvalues corresponding to $\mathfrak{R}^{-1}\vec{k}$ and \vec{k} are equal:

$$\omega_{n(\mathfrak{R}^{-1}\vec{k})} = \omega_{n\vec{k}} \quad (1.59)$$

Next, we discuss the symmetry operations that leave the WS cell invariant. For example, in Figure 1.3a) we have invariance under a mirror reflection in the x-axis, $\varepsilon(x, y) = \varepsilon(-x, y)$ or under a rotation by $\pi/3$. These two symmetry operations are called σ_x and C_6 , respectively. (Generally, C_n is defined as a rotation by $2\pi/n$ radians and σ_i denotes a mirror reflection in the axis i). A rotation by π (C_2) is known as *inversion*.

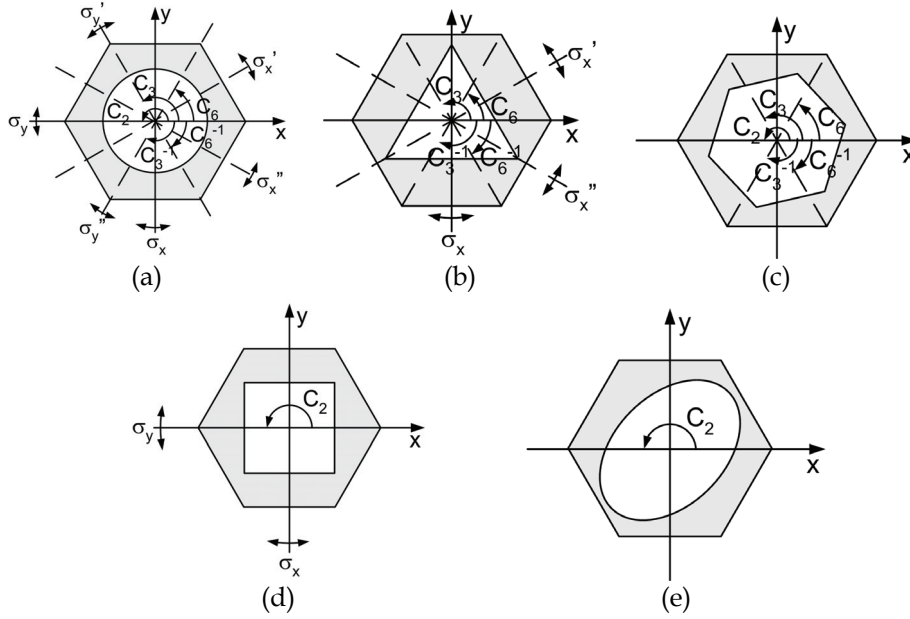


Figure 1.3 Symmetry operations for a hexagonal lattice for several “atom” shapes: (a) circle; (b) equilateral triangle; (c) rotated hexagon; (d) square; (e) rotated ellipse

So, the point group is composed of mirror, rotation and inversion symmetry operations that depend on the lattice and “atom” shape. Several illustrative examples are shown in Figure 1.3. A circle exhibits full rotational symmetry, therefore the 12 symmetry operations that map the hexagon WS cell to itself are preserved. An equilateral triangle with the same mirror symmetries as the hexagonal lattice breaks only the inversion symmetry. A rotated hexagon can break the mirror symmetries. A square breaks C_3 rotation and two mirror

symmetries. A rotated ellipse can break all rotational and mirror symmetries of the lattice and only preserves inversion symmetry.

As pointed out in equation (1.59), two \vec{k} vectors connected via a symmetry operation of the crystal lattice are equivalent. This means that the 1BZ might contain some redundant points. By eliminating these points we obtain the *irreducible Brillouin zone* (IBZ), which contains only those \vec{k} points that cannot be connected by symmetry. For the 2D case the IBZ is a polygon while for the 3D case it is a polyhedron. The vertices are called high-symmetry points (denoted by standard letters) and the lines connecting these points are high-symmetry directions. For example, the high-symmetry points of the hexagonal lattice (see Figure 1.4a) have Cartesian coordinates: $\Gamma = (0,0)$; $K = (2\pi/a)(2/3,0)$; $M = (2\pi/a)(1/2, \sqrt{3}/6)$. Then the high-symmetry directions are: ΓM , MK and ΓK . In Figure 1.4 we show IBZs (light grey) corresponding to configurations in Figure 1.3. When only inversion symmetry is present (Figure 1.4c) the IBZ is almost half of the 1BZ (only ΓK_3 is redundant, being obtained from ΓK through a C_2 rotation). In the case of mirror symmetry (Figure 1.4b) the IBZ is a quarter of the 1BZ, due to additional equivalencies $\Gamma K_1 \equiv \Gamma K_2$ and $\Gamma M \equiv \Gamma M_2$. When the WS cell has C_6 symmetry (Figure 1.4a), all ΓK and ΓM directions differing by a 60° rotation are equivalent and IBZ is reduced to the ΓMK triangle.

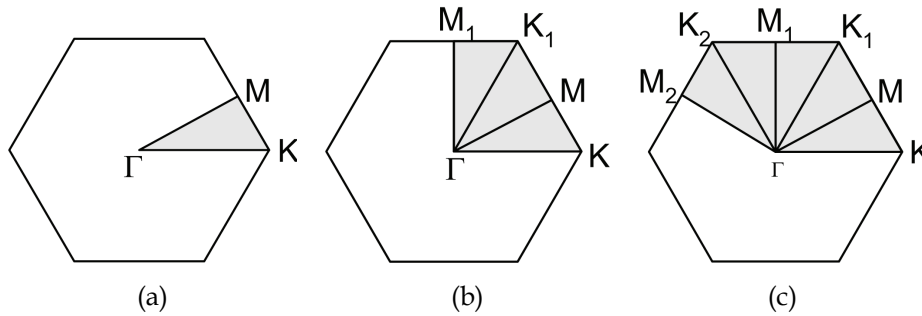


Figure 1.4 Irreducible Brillouin zone (IBZ) for several symmetries of hexagonal lattice (a) C_6 symmetry (see Figure 1.3a, b, c); (b) mirror symmetry (see Figure 1.3 d); (c) inversion symmetry (see Figure 1.3e))

It is worth noting that the symmetry depends only on the shape and not on the size of the “atom”. Therefore, the symmetry of the modes in a nearly-uniform medium (which can be found analytically, via perturbation theory) is preserved when increasing the modulation of dielectric function.

Symmetry mismatch can explain the existence of uncoupled (inactive) modes and low transmittance observed experimentally [Sakoda 1995].

Padjen *et al.* [Padjen 1994] have investigated the influence of the “atom” shape on the band structure. They concluded that a high symmetry of both Brillouin zone and filling pattern is required for obtaining a reasonably large absolute photonic bandgap. Anderson and Giapis [Anderson 1997] discussed the symmetry-induced degeneracy that is “guilty” for closing some potential

gaps between higher-order bands. They showed that lifting this degeneracy can open these gaps. However, being situated at higher frequencies, these gaps are more susceptible to fabrication disorder.

Mirror symmetry is an important concept in the physics of photonic crystal slabs [Johnson 1999] and line-defect waveguides [Notomi 2001] and it will be discussed in Chapters 3 and 4.

1.2.7 Example of band diagram

An important result of group theory [Ochiai 2001] tells us that the extreme points (i.e. maxima and minima) of *all* bands must occur along the high-symmetry directions, most of the time exactly at high-symmetry points. Therefore, when looking for a gap in the band structure, we need to consider only sampling a \vec{k} path that connects the high-symmetry directions in the IBZ. The band structure is calculated along these lines and displayed as a single graph.

In order to obtain the band diagram we need to solve equation (1.46) through some analytical or numerical method. A description of computational methods is given in Chapter 2.

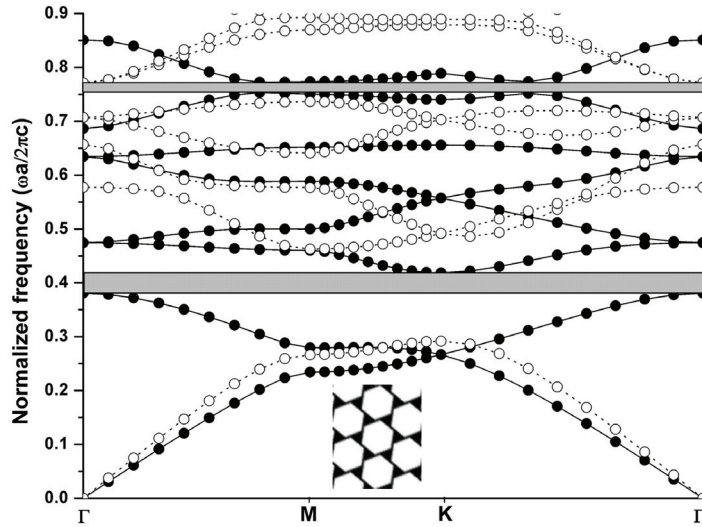


Figure 1.5 Example of band diagrams for 2D PhC made of rotated hexagonal air-holes ($n_{air}=1$) arranged in a triangular lattice (shown in inset); the background material is silicon ($n_{Si}=3.45$); filled and open circles are bands for E-modes and H-modes, respectively; the PBG is shaded grey

The band diagram of a triangular lattice of rotated hexagons (Figure 1.3c) with corresponding IBZ in Figure 1.4a is shown in Figure 1.5. This is presented here only as an illustration of band diagram concept, a detailed discussion of design parameters for such a structure is postponed for Chapter 3. The

convention adopted for labeling the polarization in 2D (E-modes and H-modes) will be explained in Chapter 2.

It can be shown (see Chapter 2) that, by dividing both sides by $(2\pi/a)^2$ in equation (1.46), one obtains an eigenvalue problem for the square of normalized frequency $\omega a/2\pi c = a/\lambda$, in which the normalized wavevector $\vec{k}a/2\pi$ enters as a parameter.

The photonic bandgap is a frequency region $\omega \in (\omega_1, \omega_2)$ that is not covered by any band, whatever \vec{k} and polarization state. In Figure 1.5 we notice the presence of a PBG between the 2nd and 3rd E-pol bands, having the edges at Γ and K points. We can define the PBG width $\Delta\omega = \omega_2 - \omega_1$ and the center frequency $\omega_0 = (\omega_2 + \omega_1)/2$. Usually the PBG width is normalized $(\Delta\omega/\omega_0)$ and expressed as a percentage.

1.2.8 Density of states (DOS)

The DOS is a measure for the number of allowed states in a certain differential energy interval and is of particular interest in quantum optical calculations. While in homogeneous media the DOS is proportional to ω^2 , in PhCs it can have peculiar variations, with applications in controlling atom-photon interactions.

The total DOS is defined mathematically as [Busch 1998]:

$$\rho(\omega) = \sum_n \int_{\text{IBZ}} d^3k \cdot \delta(\omega - \omega_n(\vec{k})) \quad (1.60)$$

In order to calculate the integral in (1.60) it is necessary to discretize the IBZ uniformly. Photonic DOS can be calculated in a similar manner as the electronic DOS once the dispersion relations $\omega_n(\vec{k})$ are known.

An example is shown in Figure 1.6. Sharp dips and peaks in the DOS coexist. Regions of zero DOS are photonic bandgaps, where no allowed states exist throughout the IBZ. On the other hand, peaks in the DOS curve correspond to a vanishing group velocity and can have applications e.g. in enhancement of nonlinear interactions.

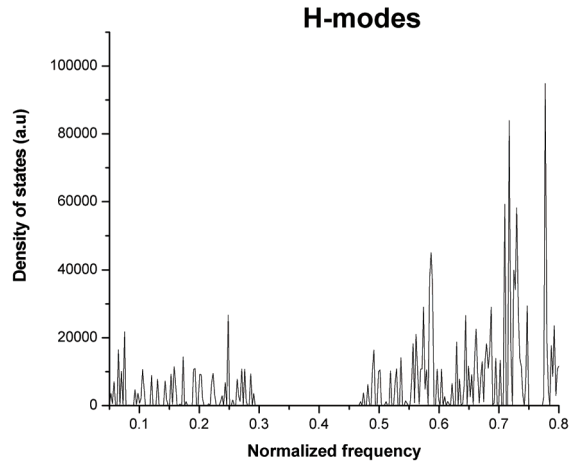


Figure 1.6 Density of states of the H-modes for the structure shown in the inset of Figure 1.5; for the PBG region in Figure 1.5 DOS is zero

1.2.9 Group velocity (v_g)

The group velocity of the eigenmodes is given by the gradient of the dispersion curves that is the derivative of ω with respect to the wave vector:

$$\bar{v}_g = \frac{\partial \omega}{\partial \vec{k}} \quad (1.61)$$

An example of group velocity calculation is shown in Figure 1.7. The group velocity of the electromagnetic waves is very small (typically 1/50 or 1/100 of the light velocity of free space) at the IBZ high-symmetry points and at those points where two modes of the same symmetry have avoided crossings (anti-crossings).

A small group velocity causes both an increase of the field amplitude [Ohtaka 1996] and a long interaction time between the electromagnetic field and matter.

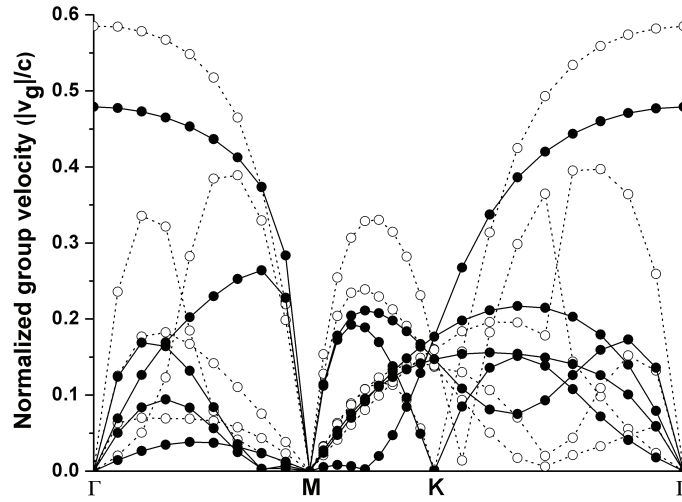


Figure 1.7 Normalized group velocity calculation, corresponding to the band structure in Figure 1.5

1.2.10 Wave-vector diagram

We consider a 2D photonic crystal, for which the band structure $\omega(k_x, k_y)$ is 3D (see Figure 1.8a).

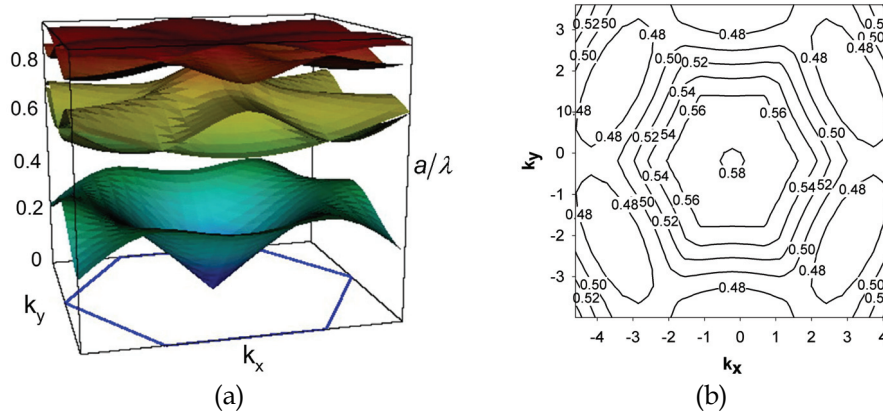


Figure 1.8 (a) Band surfaces and (b) Wave-vector contour plot for the frequency range covered by the 2nd band for H-modes of the same structure as in Figure 1.5

A section $\omega = \text{const.}$ through the band structure, possibly intersecting several bands, will result in a so-called *wave-vector diagram* (see Figure 1.8b). This is a contour map of allowed \vec{k} vectors for given photon energy and polarization.

The wave-vector diagram reveals interesting propagation phenomena in photonic crystals: negative refraction [Luo 2002], superprism effect [Baba 2002], beam collimation [Wu 2003].

1.2.11 Effective index

Looking at the example band structure shown in Figure 1.5, one notices that the first bands of both E-modes and H-modes are quasi-linear when the normalized frequency is close to zero, i.e. $a/\lambda \ll 1$. This is the long-wavelength limit where the photonic crystal can be regarded as an *effective homogeneous medium* with an effective index:

$$n_{\text{eff}} = \lim_{\omega \rightarrow 0} \frac{c|\vec{k}|}{\omega} \quad (1.62)$$

which is the inverse of the slope of the first band close to Γ point..

The E-modes and H-modes have different effective indices (in the present case $n_{\text{eff}}^E = 2.09$ and $n_{\text{eff}}^H = 1.72$) that depend on the direction of \vec{k} , and this means that the effective medium is anisotropic. A more detailed discussion of applications of photonic crystals as anisotropic meta-materials can be found e.g. in [Halevi 1999].

It is worth mentioning that a different definition of effective index is applicable for photonic crystal slabs (see Chapter 4).

Chapter 2 Computational methods and modeling tools

Theoretical calculations of PhCs are, in principle, exact, because Maxwell's equations are derived from first principles. Therefore, the power of computations is comparable to that of experiments in characterization of PhCs.

Fabrication processes of PhCs are expensive in general*, especially in the optical and near-IR regions of the spectrum. For this reason, it is important to start with a judicious design, taking into account fabrication tolerances. Such a design should be based on rigorous modeling. Rules of thumb can provide only trends in PhC properties, not exact numbers needed to embark into the fabrication.

The aim of this chapter is to present an overview of most common computational methods and modeling tools applicable to PhC analysis and design. The emphasis will be put on strengths and weaknesses of each method. The plane wave expansion method will be discussed in greater level of detail, because it reveals the main physical properties of PhCs, introduced in Chapter 1. The calculation results, their physical interpretation and the design rules derived from them will be presented in the next two chapters.

2.1. Plane wave expansion method (PWEM)

PWEM consists in expanding the periodic functions in appropriate Fourier series and inserting the expansions into the wave equation. The result is an infinite matrix-eigenvalue problem, which has to be truncated for numerical calculations. Through solving the eigenproblem one obtains the spectrum of eigenfrequencies (i.e. band structure) and expansion coefficients for the Bloch eigenmodes. An early PWEM implementation [Leung 1990a] was not successful due to the fact that vector nature of the EM field was ignored. Shortly after, this mistake was corrected [Leung 1990b], and PWEM has become the most popular method of analyzing PhCs.

* an exception is the case of self-organizing materials, which can be relatively low cost

2.1.1 Representation of dielectric function and convergence issues

The representation of $\varepsilon_r(\vec{r})$ in Fourier space can be done in two ways. The *direct method* implies computing the Fourier coefficients of the inverse dielectric function $1/\varepsilon_r(\vec{r})$ *:

$$\eta(\vec{G}-\vec{G}') = \frac{1}{\Omega} \int_{\Omega} d^3r \frac{1}{\varepsilon_r(\vec{r})} e^{-i(\vec{G}-\vec{G}')\cdot\vec{r}} \quad (2.1)$$

where \vec{G} and \vec{G}' are arbitrary vectors of the infinite reciprocal lattice (see (1.33)) and Ω is the volume of the Wigner-Seitz cell (see (1.28)).

The *HCS method* (named after its authors, Ho, Chan and Soukoulis [Ho 1990]) is based on Fourier transforming $\varepsilon_r(\vec{r})$:

$$\varepsilon(\vec{G}-\vec{G}') = \frac{1}{\Omega} \int_{\Omega} d^3r \varepsilon_r(\vec{r}) e^{-i(\vec{G}-\vec{G}')\cdot\vec{r}} \quad (2.2)$$

and using the Fourier expansion $1/\varepsilon_r(\vec{r}) = \sum_{\vec{G}, \vec{G}'} \varepsilon^{-1}(\vec{G}-\vec{G}') e^{i(\vec{G}-\vec{G}')\cdot\vec{r}}$ in equation (1.13).

Matrix inversion and Fourier transformation commute. Therefore for a complete (i.e. infinite) set of plane waves the results provided by the direct method and by HCS method must coincide. However numerical computations are performed in a finite subspace of the reciprocal lattice, so the results will be different. In practice, the *convergence* rates of the two methods described above are very different, the HCS method performing much better than the direct method.

For regular 'atom' shapes (e.g. circle, rectangle, hexagon) the Fourier coefficients from (2.1) and (2.2) can be calculated analytically [Wang 2001]. In the general case, these coefficients can only be evaluated numerically. We consider the parallelepiped primitive cell built on lattice vectors \vec{a}_k and a $N_1 \times N_2 \times N_3$ grid along these directions, the total number of discretization points being $N=N_1N_2N_3$; then, the position vector inside the primitive cell can be expressed using three indices, n_k , ($k=1,2,3$), which each can take N_k different values $n_k=0, \dots, N_k-1$, so that:

$$\vec{r} = \sum_k \frac{n_k}{N_k} \vec{a}_k, \quad k=1,2,3 \quad (2.3)$$

A reciprocal lattice vector can be expanded using a planewave set with number of terms $N_{PW}=N$, with zero-centered wave-vectors [Johnson 2001]:

* The reason why we use reciprocal lattice vectors $(\vec{G}-\vec{G}')$ in the expression of $\varepsilon_r(\vec{r})$ can be understood intuitively from the expression of (1.10) in Fourier space: Fourier expression of the product $\varepsilon_r(\vec{r})\vec{E}(\vec{r})$ implies convolution of Fourier coefficients.

$$\vec{G} = \sum_j m_j \vec{b}_j, \quad j = 1, 2, 3 \quad (2.4)$$

Using (2.3) and (2.4) in (2.2) we obtain the Fourier coefficients:

$$\varepsilon_r(m_1, m_2, m_3) = \frac{1}{N} \sum_{k_1=1}^{N_1} \sum_{k_2=1}^{N_2} \sum_{k_3=1}^{N_3} \varepsilon_r \left(\sum_{j=1}^3 \frac{n_{k_j}}{N_j} \mathbf{a}_j \right) e^{-i2\pi \sum_{j=1}^3 \frac{n_{k_j} m_j}{N_j}} \quad (2.5)$$

This is a *discrete Fourier transform (DFT)* which can be computed by an efficient fast Fourier transform (FFT) algorithm in $O(N \log N)$ time [Johnson 2001].

In practical structures of interest inversion symmetry of the dielectric function (i.e. $\varepsilon_r(-\vec{r}) = \varepsilon_r(\vec{r})$) is very common and this simplifies the numerical algorithm (factor of two savings in storage, more than a factor of two in calculation time).

Most of the photonic crystals considered have a piecewise constant dielectric function. It is well known that Fourier representation of step discontinuities at the boundaries suffers from poor convergence [Sözüer 1992]. Because the discontinuous step function is reconstructed from a series of continuous sine and cosine functions, the Fourier series cannot be uniformly convergent. While yielding convergence of the mean, the Fourier series leads to overshoots and undershoots of the actual values close to discontinuities; this is known as the *Gibbs phenomenon*. When the number of expansion terms increases (for a better representation of the step dielectric function) the overshoots and undershoots increase while moving closer to the discontinuity and the dielectric function can be much larger or smaller than the actual values at the interface (can even become locally negative).

This convergence problem has been noticed long ago in diffraction grating theory, a field closely related to photonic crystals. Li solved the convergence problem for diffraction gratings with rectangular profile [Li 1996]. He introduced three theorems for the correct factorization of products of discontinuous functions. Shen and He analyzed the PWEM convergence [Shen 2002] for different formulations in the simplest case of 1D photonic crystals. It turned out that the formulation based on Li's factorization rules performs much better than HCS method for any polarization. Lalanne [Lalanne 1998] applied Li's results to 3D photonic crystals with permittivity discontinuities perpendicular to the principal dielectric axes (e.g. simple cubic) and showed a significant improvement of the convergence, especially for the low order bands. Popov and Nevrière [Popov 2000] generalized the work of Li for arbitrary grating profiles, naming their technique "fast Fourier factorization". For 1D and 2D these factorization rules can be easily applied, while for arbitrary 3D photonic crystals it is still cumbersome.

Another way to improve convergence is by smoothing the dielectric function along the boundary between dielectrics. For example, one can think about approximating a discontinuous step function for a circular "atom" with a continuous super-Gaussian [Villeneuve 1994] [Pottage 2001] as follows:

$$\varepsilon(r) = \varepsilon_b + (\varepsilon_a - \varepsilon_b) \exp\left[-(r/R)^{2n}\right] \quad (2.6)$$

where $\varepsilon_a, \varepsilon_b$ are the dielectric permittivities of “atom” and “background”, respectively, r is the radial position, R is the circle radius and n is a positive integer (the order of super-Gaussian).

High-order super-Gaussians are smooth and approximate a step-discontinuity very well, and can be made to go from maximum to minimum in a small fraction of the electromagnetic wavelength. The order of the super-Gaussian must be large (on the order of 100) for the higher-order bands to converge within an acceptable accuracy. But then, super-Gaussians will lead to similar spatial fluctuations and overshoots as those produced by step functions.

Besides the analytical super-Gaussian functions, the smoothing of dielectric function across boundary can be done numerically using an average procedure based on the effective-medium theory [Meade 1993], [Johnson 2001].

The discretization grid in equation (2.3) divides the volume of the primitive cell in elements called *voxels*, centered on the grid points. For a voxel surrounding a grid point that lies on or near an interface, different parts of the voxel lie in different materials. To calculate accurately the average value of the dielectric function (i.e. refractive index) we *oversample* the boundary voxels on a much denser grid. Effective-medium theory tells us that the average ε depends upon the polarization of the incident wave relative to the surface normal \hat{n} . For an electric field $\vec{E} \parallel \hat{n}$, one averages the inverse of ε ; for $\vec{E} \perp \hat{n}$, one takes the inverse of the average of ε . But the local orientation of the fields is not known in advance and varies from one mode to another. Therefore, to improve convergence for all polarization states, an appropriate solution is to define a *dielectric tensor* at the boundary grid point. This takes into account the orientation of the boundary – the material is modeled as if it were anisotropic, even though the physical materials on either side of the boundary are isotropic. By using this averaging the error decreases with the square of the resolution.

2.1.2 Matrix eigenvalue problem

Since $\vec{h}(\vec{r})$ is periodic, it can be expanded in Fourier series:

$$\vec{h}(\vec{r}) = \sum_{\vec{G}} \vec{h}_{\vec{G}} e^{i\vec{G}\cdot\vec{r}} \quad (2.7)$$

which is a sum over all harmonics of the primitive lattice spatial frequencies.

The dependence on n and \vec{k} is implicitly assumed, but the subscripts are suppressed for simplicity. Because the basis functions are scalar, the Fourier coefficients need to be vector.

Using the Fourier expansions (2.2) and (2.7) we obtain the matrix eigenvalue equation of PWEM (the calculation is presented in detail in Appendix B)

$$\sum_{\vec{G}'} |\vec{k} + \vec{G}| |\vec{k} + \vec{G}'| \varepsilon^{-1}(\vec{G} - \vec{G}') \begin{bmatrix} \hat{e}_{2\vec{G}} \cdot \hat{e}_{2\vec{G}'} & -\hat{e}_{2\vec{G}} \cdot \hat{e}_{1\vec{G}'} \\ -\hat{e}_{1\vec{G}} \cdot \hat{e}_{2\vec{G}'} & \hat{e}_{1\vec{G}} \cdot \hat{e}_{1\vec{G}'} \end{bmatrix} \begin{bmatrix} h_{1\vec{G}'} \\ h_{2\vec{G}'} \end{bmatrix} = \left(\frac{\omega}{c}\right)^2 \begin{bmatrix} h_{1\vec{G}} \\ h_{2\vec{G}} \end{bmatrix} \quad (2.8)$$

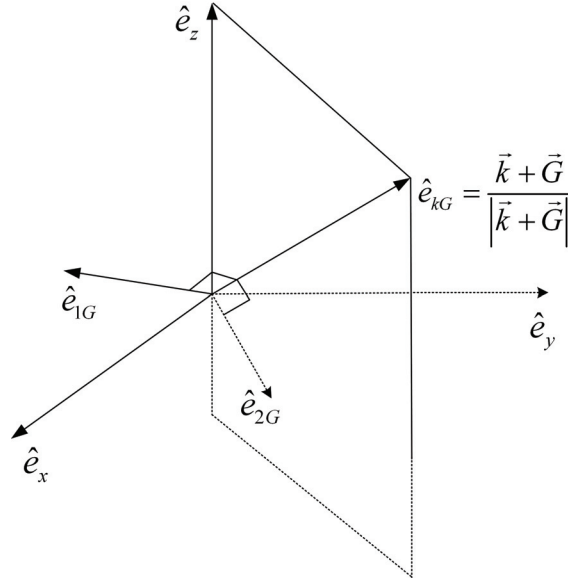


Figure 2.1 Cartesian triad formed by propagation vector of plane wave and polarization vectors of \vec{h} (see text for details)

Unit vectors $\hat{e}_{1\vec{G}}$, $\hat{e}_{2\vec{G}}$ are polarization vectors. In principle they can have arbitrary orientations in the plane perpendicular to $(\vec{k} + \vec{G})$, there is an unlimited number of possibilities in choosing their directions. For example, as shown in Figure 2.1, $\hat{e}_{1\vec{G}}$ can be in the (\hat{e}_x, \hat{e}_y) plane, then $\hat{e}_{2\vec{G}}$ is in the plane spanned by \hat{e}_z and \hat{e}_{kG} .

In the case of 2D photonic crystals and in-plane propagation \hat{e}_{kG} is in the (\hat{e}_x, \hat{e}_y) plane. Then:

$$\hat{e}_{1\vec{G}} \cdot \hat{e}_{1\vec{G}'} = \frac{(\vec{k} + \vec{G}) \cdot (\vec{k} + \vec{G}')}{|\vec{k} + \vec{G}| |\vec{k} + \vec{G}'|}$$

$$\hat{e}_{2\vec{G}} = \hat{e}_{2\vec{G}'} = \hat{e}_z$$

$$\hat{e}_{2\vec{G}} \cdot \hat{e}_{1\vec{G}'} = \hat{e}_{2\vec{G}'} \cdot \hat{e}_{1\vec{G}} = 0$$

and equation (2.8) decouples in :

$$\sum_{\vec{G}'} |\vec{k} + \vec{G}| |\vec{k} + \vec{G}'| \varepsilon^{-1} (\vec{G} - \vec{G}') h_{1\vec{G}'} = \left(\frac{\omega}{c}\right)^2 h_{1\vec{G}} \quad (2.9)$$

$$\sum_{\vec{G}'} (\vec{k} + \vec{G}) \cdot (\vec{k} + \vec{G}') \varepsilon^{-1} (\vec{G} - \vec{G}') h_{2\vec{G}'} = \left(\frac{\omega}{c}\right)^2 h_{2\vec{G}} \quad (2.10)$$

Equations (2.10) and (2.9) correspond to H-modes and E-modes, respectively[#].

Instead of using a variable coordinate system in the reciprocal space, one could use the Cartesian system $(\hat{e}_x, \hat{e}_y, \hat{e}_z)$ and eliminate one \vec{H} -field component from the transversality equation (1.12) [Suzuki 1995], [Lalanne 1998]. The disadvantage of this approach is that the symmetry of the final matrix is lost and its diagonalization is more complicated.

Because in standard formulation of PWEM, factors $O(|\vec{k} + \vec{G}|^2)$ appear in the numerator of the matrix in the eigenvalue problem (see (2.8)), there can be large elements outside the truncated matrix. Ohfuti *et al.* [Ohfuti 1997] developed a new formulation in which the matrix to be diagonalized has eigenvalues $1/\omega^2$. They called it ‘P-formulation’, because the eigenvalue problem determines the polarization. The factors $O(|\vec{k} + \vec{G}|^2)$ appear in the denominator this time, leading to a better convergence behavior for large reciprocal lattice vectors.

For large 3D systems, solving the matrix eigenproblem becomes a significant computational burden, in terms of memory and time (storage resources scale as $O(N^2)$ and CPU time necessary for matrix diagonalization scale as $O(N^3)$).

2.1.3 Variational formulation

Fortunately, in practice only lowest p bands are typically desired, with $p \ll N$. Iterative methods are available to compute the bands with only $O(pN)$ storage and $O(i_c p N \log N) + O(i_c p^2 N)$ operations, where i_c is the number of iterations for the eigensolver to converge. This number is difficult to predict, but in practice is often seen that it grows only very slowly with p and N . Thus, the number of operations in the algorithm can be much smaller compared to conventional PWEM. Unlike the conventional PWEM, the variational method does not require storage of a dense matrix.

The electromagnetic energy functional (known also as “Rayleigh quotient”):

$$E_f[\vec{h}_{\vec{k}}(\vec{r})] = \frac{\int_{\Omega} d\vec{r} \cdot \vec{h}_{\vec{k}}^*(\vec{r}) \cdot [\hat{\Theta}_{\vec{h}\vec{k}} \vec{h}_{\vec{k}}(\vec{r})]}{\int_{\Omega} d\vec{r} \cdot \vec{h}_{\vec{k}}^*(\vec{r}) \cdot \vec{h}_{\vec{k}}(\vec{r})} \quad (2.11)$$

is real and positive for any function $\vec{h}_{\vec{k}}(\vec{r})$. It can be proven that the field pattern that minimizes $E_f[\vec{h}_{\vec{k}}(\vec{r})]$ is the eigenvector of $\hat{\Theta}_{\vec{h}\vec{k}}$ with minimum eigenfrequency. Each of the next eigenmodes (i.e. upper bands) are found by

[#] The convention adopted in this thesis for mode classification: in 2D, modes which have the E(H) field oriented along the infinite axis are called ‘E-modes’ and ‘H-modes’, respectively

the same minimization, while being orthogonalized against previously found modes (this procedure is called *deflation*).

The variational algorithm (implemented in the freely available program ‘MIT Photonic Bands Package-MPB’ by Steven Johnson [Johnson]) is divided in the following steps [Meade 1993], [Johnson 2001]:

1. start with a trial vector field $\vec{h}_{\vec{c}}$ and compute its *curl* (this is just the cross-product with $(\vec{k} + \vec{G})$, a diagonal operator in wave-vector space);
2. transform the result in the direct space by a fast-Fourier-transform (FFT);
3. multiply by a smoothed dielectric tensor $\widetilde{\epsilon}^{-1}$ calculated based on effective medium theory; this multiplication is diagonal in real space, since it affects each real-space location independently; the number of plane waves per polarization (N) is equal to the number of grid points on which the dielectric function is sampled (N_{FFT}).
4. transform back to reciprocal space by performing an inverse-fast-Fourier-transform (IFFT);
5. calculate the *curl* once again this provides the next generation of $\vec{h}_{\vec{c}}$ and obtain the ‘Rayleigh quotient’;
6. repeat steps 1-5 iteratively, in order to minimize the ‘Rayleigh quotient’ within a desired accuracy, based on a systematic algorithm (e.g. preconditioned conjugate-gradient descent)

Since all the matrix operations are diagonal in this scheme the storage is only $O(N)$. The computer time required is dominated by the Fourier transform step which is $O(N \log(N))$.

The MPB program can be applied for calculating localized ‘defect’ states in the PBG (e.g. modes guided along a line-defect in a photonic crystal) by using a supercell. The supercell is a domain composed of many unit cells that surround the ‘defect’ region (see Chapter 4). The increase in domain size leads to the increase of memory requirements and calculation time. The band folding effect produces many redundant bands below the PBG that will all be computed through the standard eigensolver in MPB (the band folding effect is discussed in more detail in Chapter 4). A shortcut to the ‘defect’ states would be to use a ‘targeted’ eigensolver that can shift the frequency origin in the PBG region. Unfortunately, the targeted eigensolver in MPB seems to have convergence problems for line-defects.

A potential disadvantage of the planewave basis is that it corresponds to a *uniform* spatial grid. A set of localized functions on an unstructured mesh (e.g. finite-element) can provide a more economical solution.

In the case of a dispersive material (i.e. dielectric function depends not only on position, but also on frequency), the frequency ω cannot be factorized, and solving for it means finding the roots of a nonlinear and transcendental function. This represents a very difficult numerical task.

In PWEM the structure is supposed to be of infinite extent and only propagative Bloch states are calculated. Evanescent states are *a priori* excluded.

2.2. Transfer matrix method (TMM)

This method has been introduced by Pendry and MacKinnon [Pendry 1992] in analogy with *on-shell* (i.e. fixed frequency) methods in low-energy electron diffraction theory. Instead of transforming to Fourier space, TMM is based on representing Maxwell's equations on a discrete lattice (Cartesian, in general) of real space points. The resulting discrete equations are recast into the form of a transfer matrix that connects the electric and magnetic fields in one layer of lattice points to those in next layer.

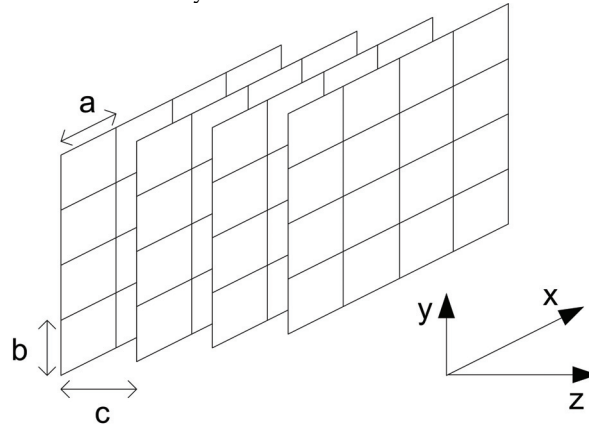


Figure 2.2 Cartesian spatial discretisation applied in TMM

By taking products of transfer matrices one can find the fields at every point of the domain. But it is well-known that the multiplication of transfer matrices can suffer from serious numerical instabilities, due to exponentially growing terms. The solution to this problem is to divide the domain in “slices” thin enough so that these instabilities do not occur, then combine these slices using a stable recursion algorithm (e.g. scattering matrix). However, stability comes at the price of reduced speed, because the simple multiplication of sparse transfer matrices is replaced by a more involved recursion.

TMM yields the transmission spectrum directly (this can then be compared with experimental data) and Bloch wavevectors via the eigenvalues of the matrix. TMM uses a uniform Cartesian grid, but it can be better adapted by a coordinate transformation [Pendry 1996].

The original computer code developed by the group of John Pendry has been re-written by Andrew Reynolds who added a graphical user interface, and is freely available under the name “*Translight*” [Reynolds].

2.3. Diffraction grating approach

Photonic crystals can be regarded as multilayer diffraction gratings with sub-wavelength periodicity. For example, a 2D PhC is a stack of identical 1D gratings, while a 3D PhC is a stack of crossed gratings. The vast research

carried out in the field of diffraction gratings can be applied to modeling and design of photonic crystals.

Dansas and Paraire [Dansas 1998] applied the classical rigorous coupled-wave analysis (RCWA also known as “Fourier modal method” [Lalanne 2000]) to 2D PhCs, considering an arbitrary profile as a stack of lamellar gratings. But the staircase approximation of the geometrical profile raises convergence problems [Popov 2002]. Maystre [Maystre 1994] and Botten *et al* [Botten 2001] applied the integral method that uses the assumption of no interpenetration of successive layers (i.e. the grating regions are separated by homogeneous thin layers). However, this does not apply for some interesting configurations (e.g. triangular lattice of circular holes with high filling factor).

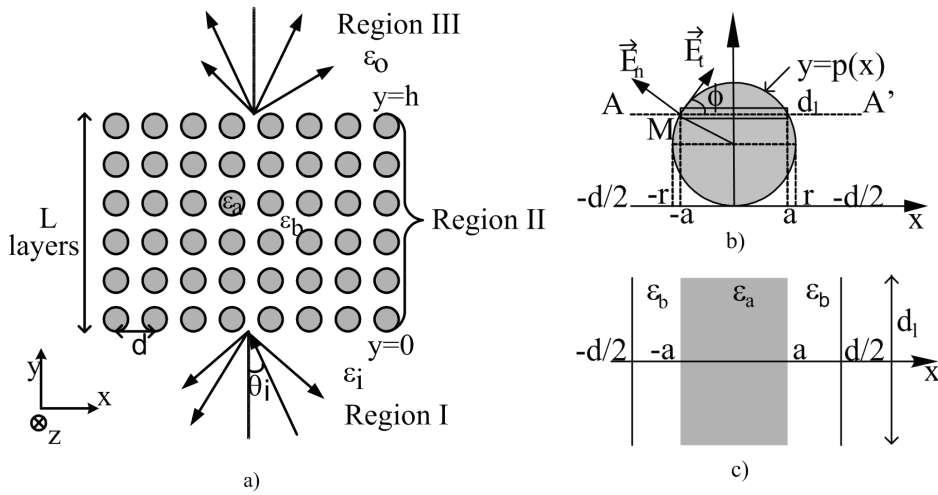


Figure 2.3 (a) Two-dimensional square array of cylinders; the entire domain is divided into 3 regions: I, III – semi-infinite homogeneous layers; II – array of cylinders periodic along x , there are L layers along direction y ; the cylinders have infinite height (along z) and their cross-section in the x - y plane is described by a function $y=p(x)$; (b) detailed view of one ‘atom’; a slicing line intersects the profile in $x=\pm a$, in these points the in-plane component of the E-field is decomposed in E_t (tangential) and E_n (normal); $\phi=\tan^{-1}[p'(a)]$ is the angle between E_t and x -axis; (c) zoom view of the slice with thickness d_i determined by the slicing line A - A' ; the filling factor (i.e. duty cycle) depends on the y position of slicing line [Bostan 2002b]

Popov and Neviere [Popov 2000] reformulated the differential theory of diffraction gratings with arbitrary profile and solved the convergence problems for H-polarization by a technique they called “fast Fourier factorization” (FFF). The main idea is to decompose the fields in components that are *locally* tangent and normal to the grating profile (see Figure 2.3b). Although the resulting equations are more complicated, the reward is a reduced dimensionality of the problem (because convergence is obtained with a significantly smaller number of Fourier components) and a shorter computation time. Bostan and de Ridder [Bostan 2002b] applied the FFF rules

in the framework of RCWA method and obtained new expressions for the eigenvalue problem and the scattering matrix algorithm.

Lalanne and Benisty [Lalanne 2001] formulated a 3D RCWA method for quasi-2D photonic crystals (having 2D periodicity and finite thickness). Briefly, the method relies on an artificial periodization along the vertical y direction and approximating the real continuous profile along the propagation direction z by a stack of slices with piecewise-constant refractive indices (Figure 2.4). In the vertical direction the slabs are separated by absorbing layers (e.g. “perfectly matched layers”-PMLs [Bérenger 1994]) so that the interaction between neighboring slabs is minimized and out-of-plane scattering into the substrate and the air is accurately taken into account. PMLs give reflectionless absorption of the incident field regardless of wavelength, polarization or incidence angle. PMLs are made of a nonphysical absorbing material, which strongly attenuates the incoming electromagnetic waves, while the phase velocity remains unchanged.

The electromagnetic fields and the refractive index in the transverse plane (x, y) are expressed as Fourier series. In every slice, the modes and their propagation constants are computed exactly. The scattering matrix, relating the input and output fields, is computed recursively by matching the boundary conditions at the slice interfaces. This method, however, has a couple of shortcomings: (i) combining PMLs with Fourier expansions leads to more complicated eigenvalue problems (even truly guided modes will have complex propagation constants); (ii) the staircase approximation has convergence problems [Popov 2002].

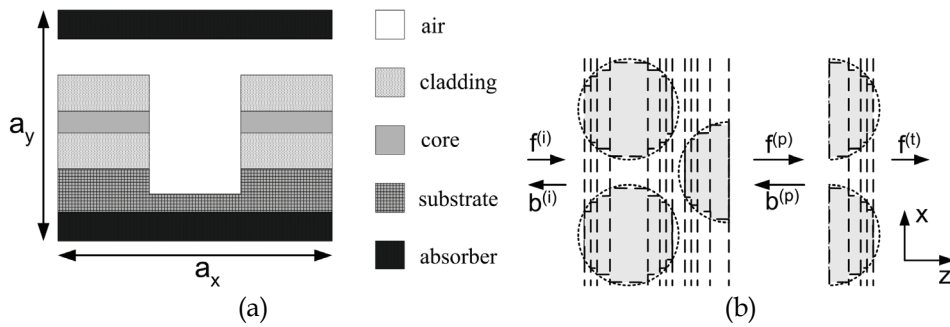


Figure 2.4 (a) 2D periodic computational domain: natural periodicity along x direction, artificial periodization along the vertical y direction; (b) staircase approximation of refractive index along the propagation direction z [Lalanne 2000]

2.4. Eigenmode expansion method (EME)

The eigenmode expansion method (also called “mode-matching method”) [Bienstman 2001] is somewhat related to the diffraction grating approach: the same staircase approximation of the refractive index profile (Figure 2.4b) is applied and an S-matrix algorithm makes connection between layers.

However, this time the structure is finite in the transverse direction, not infinitely periodic. We do not use Fourier expansions, instead, in each of the longitudinally invariant slices we find the local eigenmodes of the 1D multilayer slab waveguide (for a 2D structure, infinite in the y direction). The set of vectorial eigenmodes can be calculated quasi-analytically. In order to include a discrete set of radiation modes, the structure under study has to be enclosed by metal walls (“perfect electric conductor”-PEC or “perfect magnetic conductor”-PMC). This has a disadvantage: instead of freely escaping towards infinity, the radiated fields are reflected back into the structure, disturbing the simulation results. A solution is to coat the metal boundaries with PMLs that will absorb the incident radiation, simulating the open space [Bienstman 2002]. The presence of PML gives rise to an imaginary component in the propagation constants (without PML they would have been real for lossless materials). Calculating the complex eigenvalues is quite tricky and choosing the right PML “strength” in order to avoid numerical problems is a matter of trial-and-error, there is no well-established recipe.

Metal walls alone are useful for exploiting symmetries (e.g. calculating the band structure of photonic crystals that extend infinitely in both the longitudinal and transverse direction).

Both diffraction grating approach and EME are well suited for cases in which a single “building block” is repeated many times within the structure under study (this happens often with photonic crystal devices). One needs only to compute the scattering matrix of the building block, and iterate it to build the global S-matrix. This way, the computational complexity scales logarithmically with the longitudinal dimension of the structure.

By using EME with a PML transverse boundary condition one is able to calculate the radiation losses in Bloch modes of structures that are only periodic in the z -direction.

The computational complexity of EME scales as $O(N^3)$, where N is the number of eigenmodes. By introducing PMLs, the transversal size of computational domain can be reduced, which allows a decrease in N .

The principles of EME have been implemented by Peter Bienstman from Ghent University-Belgium in a freely available program called ‘*Cavity Modelling Framework*’ (CAMFR) [Bienstman].

2.5. Scattering matrix method (SMM)

This method, introduced by Whittaker and Culshaw [Whittaker 1999] is applicable to 3D modeling of multilayer dielectric waveguides with two-dimensional lattices of holes (i.e. *photonic crystal slabs-PCS* that will be discussed in Chapter 3). The optical confinement in the third dimension, perpendicular to the plane of periodicity is ensured by conventional *total internal reflection*.

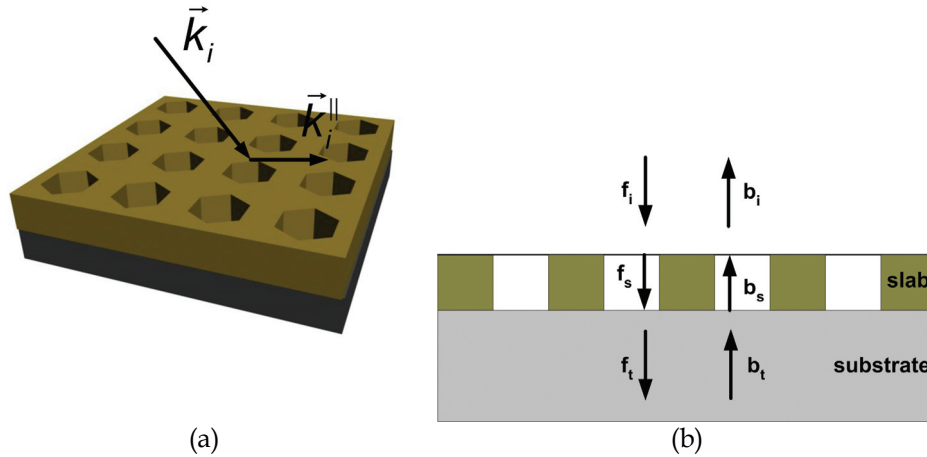


Figure 2.5 (a) Configuration used in ‘variable angle spectroscopy’ (perspective view of PCS); the magnitude and direction of the parallel component of the incident wave-vector are tunable; (b) Amplitudes of forward and backward propagating waves (section view of PCS)

SMM involves the following steps:

- Divide the system into layers that are homogeneous along the vertical z -axis; each layer can be either homogeneous or patterned;
- suppose each layer infinite (i.e. ignore its boundaries) and solve an eigenvalue problem for the vertical momentum k_z (the in-plane momentum (k_x, k_y) and the frequency ω are taken as inputs into Maxwell’s equations);
- use the truncate set of plane waves $\exp(ik_z z)$ as a basis to expand the total field in each layer as a superposition of forward and backward propagating plane waves;
- apply electromagnetic boundary conditions at the interfaces and construct propagation and interface transfer matrices that connect amplitudes in different parts of the structure (see Figure 2.5b);
- construct the total scattering matrix S of the whole structure, via an iterative procedure;
- calculate, from the components of the S matrix: (i) optical properties of the system (e.g. transmission, reflection, emission, absorption) and the corresponding spatial distributions of the electromagnetic fields; (ii) both guided and leaky eigenmodes (band structure) of multilayered photonic crystal slab [Tikhodeev 2002]

SMM has the important advantage that the calculated spectra can be directly compared with measurements obtained by *variable angle reflectance spectroscopy* [Astratov 1999] (see Figure 2.5a). These measurements probe the coupling of scattering modes to external fields. The reflectance spectra show dips whose energy position and width provide information on the frequency and inverse radiative lifetime of the quasiguided eigenmodes.

SMM, like PWEM, is based on Fourier expansions, so it can suffer from convergence problems.

2.6. Multiple scattering technique (MST)

MST is applicable when the ‘atoms’ have cylindrical or spherical shape [Wang 1993]. The basis set best suited for these geometries is composed of Bessel-Hankel functions. Then, only a few modes are enough to account properly for the field continuity at the interfaces between dielectric discontinuities. On the downside, the main disadvantage of MST is that its matrix scales linearly with N , the number of ‘atoms’ in the domain, which leads to $O(N^3)$ complexity.

2.7. Finite element method (FEM)

FEM uses an unstructured mesh for representing the domain, which is broken down into many elements of simple shape and different size and orientation (e.g. triangles in 2D-see Figure 2.6, tetrahedra in 3D). This kind of mesh brings up two main improvements with respect to e.g. a uniform Cartesian grid: (i) regions of arbitrary shape are represented better (no staircase approximation); (ii) the FEM mesh can use *locally* a higher density of nodes in key regions that require it (e.g. narrow veins of high refractive index, typical in photonic crystals), without refining the discretisation of the whole domain. Moreover, since the discontinuous refractive index is handled in real space, FEM does not have the convergence problems of classical PWEM.

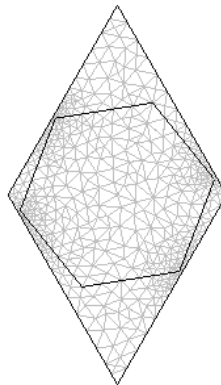


Figure 2.6 Primitive cell of triangular lattice of rotated hexagons discretised with a FEM mesh

Briefly, FEM goes as follows. Maxwell’s equations are cast into a set of linear equations which approximate the field over an element: some interpolation function is chosen and its coefficients are computed for each element and stored as elemental matrices; these matrices are then assembled into global

matrices that form an eigenvalue problem whose dimension depends on the number of elements. A detailed description of FEM technique applied to photonic crystals can be found in [Hielt 2002].

The eigenproblem matrices appearing in FEM are very sparse, leading to an algorithm complexity $O(N)$, where N is the number of degrees of freedom, proportional with the number of nodes. Despite this favorable scaling, FEM runs into trouble for large 3D domains, due to huge memory requirements. Still, FEM can be successfully applied for 2D finite-sized photonic crystals and 3D primitive-cell problems with Bloch boundary conditions.

2.8. Finite difference time-domain (FDTD)

The FDTD method reproduces numerically the propagation in real space of time-varying electromagnetic waves. FDTD has been widely used for calculating the radiating properties of finite-sized photonic crystals (e.g. quality factors [Miyai 2001]) and their transmission spectra [Qiu 2001]. Moreover, FDTD has been combined with Bloch boundary conditions for calculating the band structure of a photonic crystal [Loncar 2000].

The most common implementation of FDTD is the Yee algorithm [Yee 1966]. The real space is discretized in a cubic grid that stores the dielectric constant and the fields. \vec{E} and \vec{H} field components are interleaved at intervals $1/2\Delta h$ in space and $1/2\Delta t$ in time (Δh and Δt are the side of the cubic grid and the time step, respectively). Every \vec{E} component is surrounded by a circulating \vec{H} component and viceversa. The space and time derivatives are expressed through central differences, and a leap-frog time marching scheme is used for recursively updating the fields on every grid point. PMLs are used at the outer edge of the FDTD mesh in order to simulate the open space.

After setting up the domain geometry and materials properties, one has to specify the spatial and temporal excitation of electromagnetic fields and spatial positions and geometry of detectors.

Very often the temporal excitation is *pulsed* - expressed by a Gaussian envelope modulation of a harmonic wave. The pulse width is chosen such that its spectrum covers the frequency spectrum of interest; for example, in a photonic crystal one usually looks at the photonic bandgap region. FDTD can obtain the desired spectral response through a single simulation, applying Discrete Fourier Transform (DFT) or Fast Fourier Transform (FFT) to the temporal response. For a detailed description of the FDTD method we refer to the monograph by A. Taflove [Taflove 1995].

Important issues in FDTD are: accuracy, numerical dispersion, and stability. These are influenced by the spatial step (mesh size) and time step. Mesh size should be chosen such that $\Delta h \leq 0.1\lambda_{\min}$ (λ_{\min} is the minimum wavelength inside the computational domain). A stability condition (Courant) establishes a proportionality relation between Δt and Δh . In other words, a finer mesh leads to a shorter time step. On the other hand, FFT gives the spectral response from zero to the cut-off frequency ($1/2\Delta t$).

The computer memory required by FDTD, is proportional to N – the total number of cells in the computational domain. Another component of the computational cost is the calculation time ($i_t \Delta t$), where i_t is the number of time steps. The sampling resolution in the frequency domain is $(1/2i_t \Delta t)$. This implies a dramatic increase of i_t in order to resolve the fine details of the frequency spectrum (by the uncertainty principle of the Fourier transform: $i_t \Delta t \Delta f \sim 1$). Besides, i_t must increase linearly with the spatial resolution to maintain stability. Overall, the complexity of FDTD is $O(i_t N)$ to find the frequency spectrum, and $O(p i_t N)$ to solve also for the fields of p modes [Johnson 2001]. In some cases the complexity scales worse than $O(N)$. Consider for example a waveguide bend, made of two arms connected at an angle. Multi-reflection of the pulse takes place at waveguide exits and bend and this could result in pulse interference, preventing retrieval of bend properties (e.g. transmission coefficient). The waveguide arms should be sufficiently long to be able to separate transmitted and reflected pulses. Then, the computational resources scale as the square of arm length [Li 2003b].

In order to probe all the eigenmodes of a structure, the source and detector have to be placed away from the symmetry planes (because null positions of eigenmodes are localized there).

2.9. Discussion

After this brief overview of modeling methods, now we discuss our choice criteria, including availability. In the design process of photonic crystals considered in this thesis, two kinds of problems need to be addressed:

1. band diagrams of unbounded photonic crystals with 2D periodicity;
2. wave propagation in finite-sized photonic crystals, including their coupling to the outside world.

PWEM calculates the eigenfrequency spectrum of photonic crystals with the abilities of quickly identifying a possible PBG and resolving degenerate modes. Mode degeneracy occurs often in band diagrams of photonic crystals. Time-domain methods (e.g. FDTD) and on-shell frequency-domain methods (e.g. TMM, diffraction grating approach, EME) have difficulties in resolving it.

Although PWEM is not immediately applicable to materials with loss or dispersion, this is not of much concern here: as mentioned in Chapter 1, the materials of choice are lossless and dispersionless in the spectral range of interest. Therefore, the freely available MPB program has been used extensively for the band diagram calculations in this thesis and the results obtained will be presented in the next two chapters. While MPB is able to compute quite accurately the guided modes in photonic crystal slabs, it fails for leaky modes (see Chapter 3 for a detailed discussion). SMM is of special interest in the context of photonic crystal slabs: it can calculate both guided and leaky eigenmodes with less effort than MPB. The possible convergence problems due to Fourier expansion of the dielectric function may be solved by

one of the methods described in section 2.1.1. Unfortunately, an SMM code was not available.

Propagation and coupling phenomena in finite-sized photonic crystals can be tackled by any of the methods presented, except PWEM. Besides, all these methods are on-shell frequency-domain, except FDTD. Evanescent modes are included in the analysis, and absorption or dispersion may be accounted for (this is more easily done in frequency-domain, though). Calculated transmission and reflection spectra can be related to the band structures. Moreover, one can quantify the influence of specific design parameters (number of PhC layers, PhC orientation, incidence angle).

The author has tested the available programs and selected FEM and FDTD as giving the best performance. The other methods have been found to suffer from instabilities and convergence problems already mentioned in this chapter. A commercially available FEM program, FEMLAB from Comsol A.B. [Comsol] was used in this thesis. In author's experience, FEM proved to perform better than FDTD for 2D PhC problems, in terms of calculation time. However, FDTD scales better than FEM in terms of memory requirements and this render most of 3D PhC problems intractable by FEM. Therefore, the finite-sized PhC structures presented in this thesis were analyzed in 2D by FEM and in 3D by FDTD.

Chapter 3 Design of photonic crystals with 2D periodicity

This chapter contains applications of the theoretical framework and computational techniques. From the main calculation results we will draw design and optimization criteria of 2D PhCs and ‘photonic crystal slabs’ (PCS).

Loosely speaking, a PCS is obtained from its 2D PhC counterpart by truncating the infinite thickness down to a fraction of the lattice constant. A more complete PCS definition will be given in Section 3.2. The modes of the PCS-structure have a lower effective index, resulting in a shift of its band diagrams towards higher frequencies. Then, if the original 2D PhC has a PBG, this may be preserved in the PCS [Bostan 2002a], depending on its thickness. On the other hand, one can infer that a 2D PhC that does not have a gap in either E or H polarizations can be discarded for practical purposes, since the resulting PCS will not have a gap in guided modes. Therefore, calculations of 2D PhCs provide a good starting point in selecting promising structures for PCSs. Moreover, the calculation time is orders of magnitude shorter than that for 3D structures.

To engineer the PhC with the optimum PBG is very difficult, because it involves solving a multiparametric inverse problem. There are countless combinations of lattice symmetry, scattering object shape, filling factor and refractive index contrast, but it is impossible to predict which one gives the largest absolute PBG. A systematic algorithm is still lacking, and the PhC design is based on several *rules of thumb*, which help reducing the dimensionality of the problem. It is known that absolute PBGs are favored in PhCs that satisfy the following criteria [Joannopoulos 1995], [Wang 2001]:

- Refractive index contrast is as high as possible;
- Brillouin zone is close to a circle;
- Shape of scattering objects matches the symmetry of Brillouin zone;
- The PhC is comprised of dielectric islands connected by narrow veins (this implies a high filling-factor for the low-index material)

Instead of an inefficient and costly trial and error approach, it would be better to apply an algorithmic process to solve the mathematical inversion problem. Then, one could find an optimum that physical intuition failed to recognize. The quality of the solution can also be assessed with respect to fabrication limitations and tolerances. Shen *et al* [Shen 2003] applied a genetic algorithm as a global optimization method and demonstrated large PBGs in 2D PhCs with square lattice. However, the implementation of such an advanced algorithm is beyond the scope of this thesis.

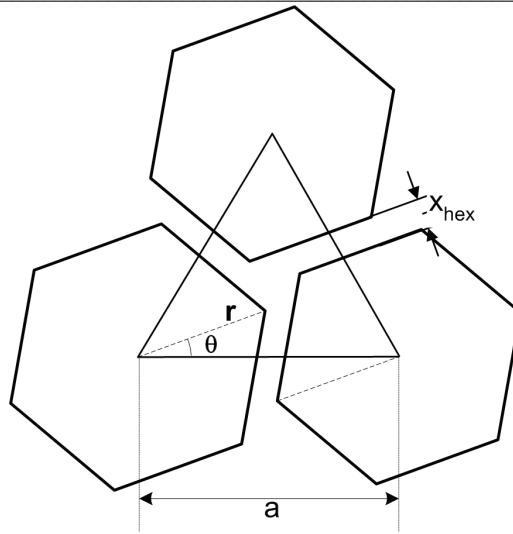


Figure 3.1 Hexagon-type PhC configuration – rotated hexagons arranged in a triangular lattice (for $\theta=0$, the vertices of neighboring hexagons are pointing towards each other, the rotation is taken counter-clockwise); geometrical parameters are indicated: lattice constant (a), radius (r), rotation angle (θ), vein thickness (x_{hex})

In this thesis, we consider mainly the “hexagon-type” PhC (see Figure 3.1) that has some advantages:

- it preserves the hexagonal lattice symmetry;
- offers flexibility in adjusting the configuration (i. e. size and orientation of veins and islands) of the lattice;
- provides a large PBG, similar to that produced by the circular “atom”

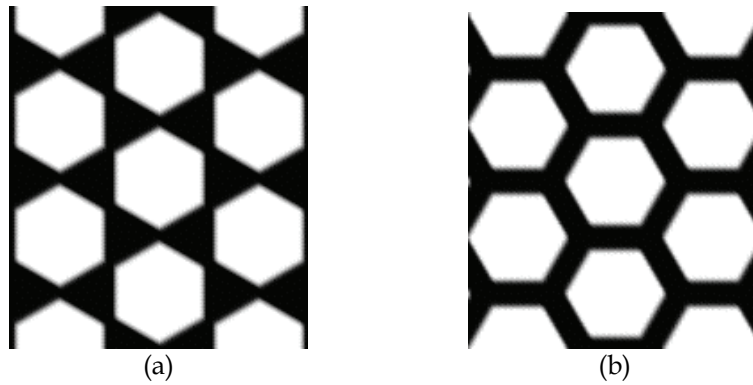


Figure 3.2 Two possible orientations of the hexagons: (a) $\theta=0^\circ$, (b) $\theta=30^\circ$

The lattice configuration can be adjusted via the rotation angle θ , going from dielectric islands (Figure 3.2a) to thin veins (Figure 3.2b) through all the intermediate configurations.

3.1. Two-dimensional photonic crystals

In this section we will discuss the conditions of opening a PBG in 2D PhCs and the variations of its position and size as a function of refractive index contrast, “atom” size and orientation. We will also address the propagation of electromagnetic waves through finite-sized PhCs.

3.1.1 Dielectric contrast and material choice

The dielectric contrast (also known as refractive index contrast) in a binary PhC can be defined as the modulus of the difference between the refractive indices of the background (n_b) and of the “atom” (n_a) media:

$$\Delta n = |n_b - n_a| \quad (3.1)$$

where the refractive index is $n = \sqrt{\epsilon_r}$.

There is a minimum value Δn_{min} that is needed to open a PBG, which depends on lattice and “atom” shape (here $\Delta n_{min} \approx 1.6$, see Figure 3.3a). The size of the PBG increases strictly monotonous with Δn (Figure 3.3b), when all the other PhC parameters are fixed. In addition, when increasing Δn the gap edges are shifting towards lower frequencies (see Figure 3.3a) and the bands are flattening (this flattening means that, for a range of wave-vectors near the gap edges, the group velocity decreases very much).

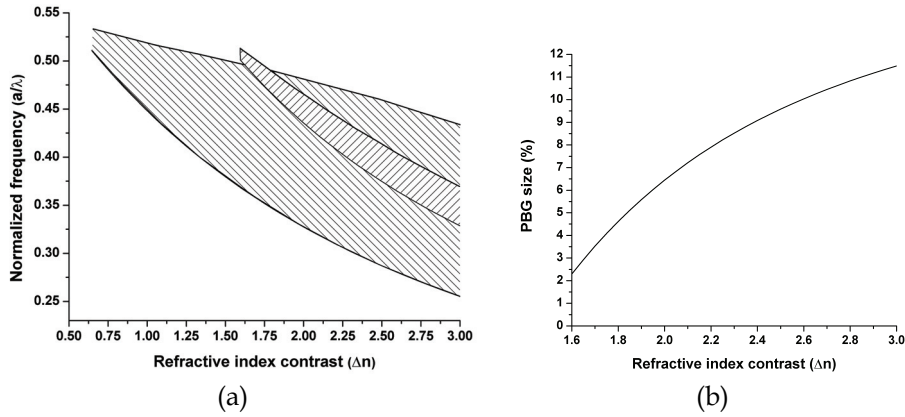


Figure 3.3 (a) Gaps map for hexagon-type PhC as function of Δn ; right-hatched and left-hatched are the gaps for E and H polarizations*, respectively and the overlap between E and H gaps is the PBG; (b) PBG versus Δn for $r=0.48a$ and $\theta=9^\circ$

* The convention adopted in this thesis for mode classification: in 2D, modes which have the E or H field oriented along the infinite axis are called ‘E-modes’ and ‘H-modes’, respectively

Our material of choice for fabricating PhCs is silicon (Si), for the following reasons:

1. Si has a high refractive index ($n_{Si}=3.45$) in the IR range of the electromagnetic spectrum; the dielectric contrast between Si and air is large enough to open sizable PBGs;
2. Si is transparent in the IR range, covering both the low-dispersion ($\lambda=1.3\mu\text{m}$) and low-loss ($\lambda=1.55\mu\text{m}$) transmission windows of silica optical fibers;
3. high-quality silicon-on-insulator (SOI) wafers are commercially available and the processing technology is standard in MESA+

3.1.2 Filling factor

We consider the case of non-overlapping “atoms”. The filling factor (f) is defined as the ratio between the “atom” area (A) and the area of the primitive cell:

$$f = \frac{A}{|\vec{a}_1 \times \vec{a}_2|}, \quad 0 \leq f \leq 1 \quad (3.2)$$

It is clear that for extreme values ($f=0, f=1$) the PhC reduces itself to a homogeneous medium. Practically, the filling factor has an upper limit given by the “close-packed” condition, which depends on lattice topology. The hexagon-type lattice in Figure 3.2 has a filling factor:

$$f_{hex} = 3 \left(\frac{r}{a} \right)^2 \quad (3.3)$$

where the “close-packed” condition for $\theta=0^\circ$, gives $r_{max}=0.5a$ and $f_{hex}^{max} = 0.75$. While the choice of constituent materials is somewhat limited, one has more freedom in tuning the filling factor. In the present case, the tuning can be done by selecting r and θ and apply nanometer resolution lithography, as shown in Chapter 5.

The filling factor depends directly on the “atom” size (e.g. radius r). Since the “atom” size is the tuning parameter in the fabrication process, we express the gap-map in Figure 3.4a as a function of (r/a) . A PBG opens up for $r \geq 0.45a$ (Figure 3.4a) and increases quasi-linearly with r (Figure 3.4b), while the gap edges are shifting to higher frequencies.

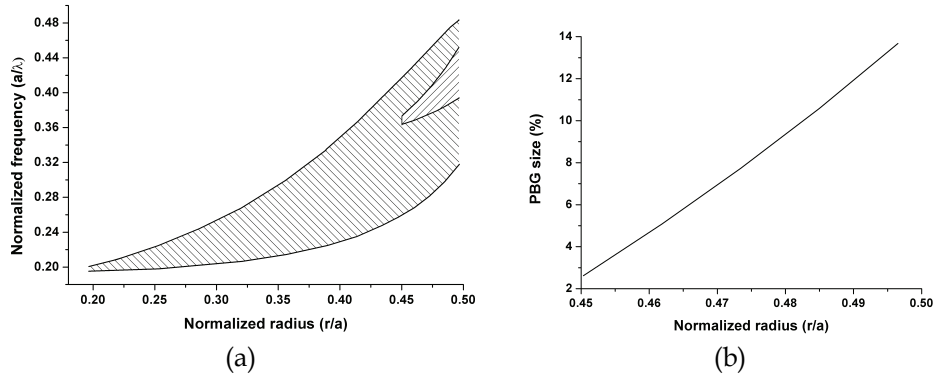


Figure 3.4 (a) Gaps map for hexagon-type PhC as function of normalized radius; right-hatched and left-hatched are the gaps for E and H polarizations, respectively and the overlap between E and H gaps is the PBG (b) PBG versus the normalized radius; the background material is Si ($n_{Si}=3.45$) and $\theta=9^\circ$

The low-index material should have a high filling factor, in order to open a large PBG in a 2D PhC.

3.1.3 Rotation angle and vein thickness

The PBG is open for rotation angles between 0° and 22° (Figure 3.5a) and its size decreases monotonously with θ (Figure 3.5b), while the gap for H polarization increases reaching its maximum at $\theta=30^\circ$. The PBG center frequency remains approximately constant with θ . By means of the rotation angle one can adjust the topology of the PhC, while keeping the filling factor constant.

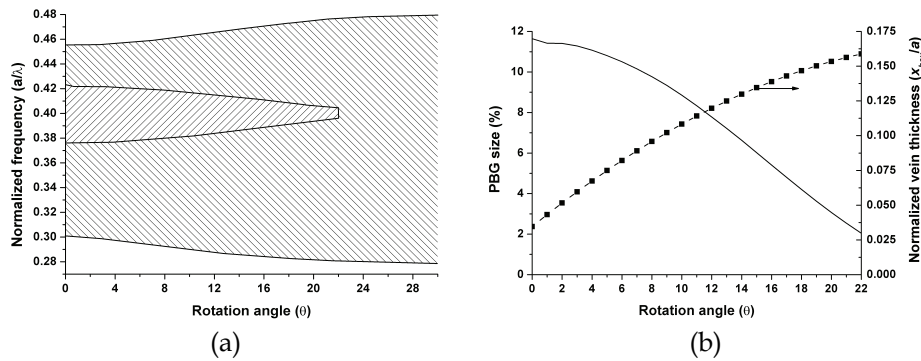


Figure 3.5 (a) Gaps map for hexagon-type PhC as function of rotation angle; right-hatched and left-hatched are the gaps for E and H polarizations, respectively and the overlap between E and H gaps is the PBG; (b) PBG versus the rotation angle; the background material is Si ($n_{Si}=3.45$) and $r=0.48a$

An important parameter from the fabrication point of view is the veins' thickness that is given by an analytical formula:

$$x_{\text{hex}} = a \sin(60^\circ + \theta) - 2r \sin 60^\circ \quad (3.4)$$

From Figure 3.5b we see that this thickness is increasing with θ . Therefore, there is a tradeoff between the PBG size and vein thickness. A reasonable choice is e.g. $x_{\text{hex}}=0.1a$ which gives $\theta=9^\circ$ and a PBG of about 9.5%. The resulting band diagram is shown in Figure 3.6. There are two PBG regions in the considered frequency range. The lower PBG has the edges at $\omega_1=0.38$ and $\omega_2=0.418$; the resulting midgap frequency and the PBG width are $\omega_0=0.4$ and $\Delta\omega/\omega_0=9.5\%$, respectively. From the normalized parameters we can retrieve the dimensions of the real PhC. For this, we require that the midgap frequency corresponds to the wavelength $\lambda_0=1.55\mu\text{m}$ and obtain consequently for the lattice constant:

$$\frac{a}{\lambda_0} = \frac{a}{1.55\mu\text{m}} = 0.4 \Rightarrow a = 620\text{nm} \quad (3.5)$$

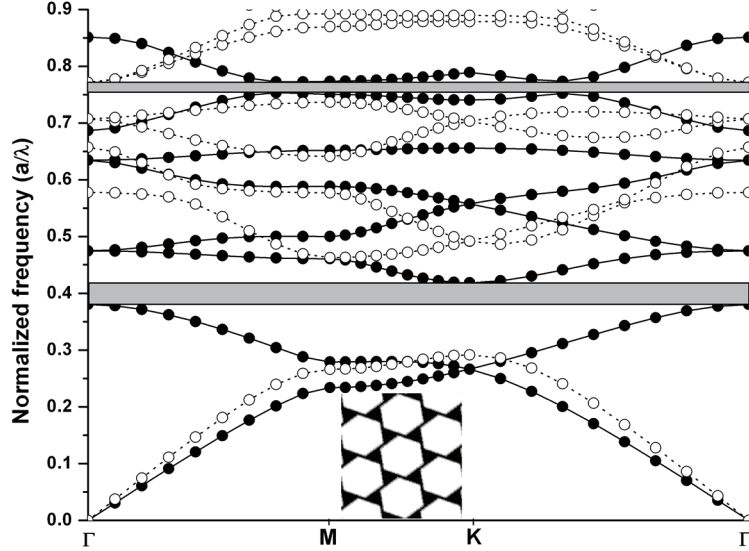


Figure 3.6 Band diagram for hexagon-type PhC made of air holes in silicon (shown in inset); E-modes and H-modes are represented with filled and open circles, respectively; geometrical parameters: $r=0.48a$, $\theta=9^\circ$

The hole radius is $r = 0.48 \cdot 620\text{nm} \approx 298\text{nm}$. The vein thickness is 62nm , a value that can be achieved with nanoscale lithographic techniques. These design parameters are valid for a 2D PhC that has an infinite height. For a PCS with a height on the order of $0.5a$ they need to be adjusted, because the PBG position shifts. This topic will be discussed in more detail in the next section.

Why didn't we choose the second PBG that is situated at higher normalized frequencies? All the geometrical dimensions would have been scaled up and this would have been advantageous from the fabrication point of view. There are a few reasons why the lowest PBG is preferable in practice: (i) higher order PBGs are generally smaller than the first PBG (this conclusion has been drawn

after many numerical calculations) [Johnson 2003]; (ii) higher order PBGs are more susceptible to fabrication disorder; (this can be shown by applying perturbation theory [Johnson]); (iii) the scattering losses of guided modes in PCs are proportional to the square of the normalized frequency [Ferrini 2003].

3.1.4 Transmission through finite samples

All the real-life PhC samples are finite. Then the question arises about the connection between the band diagrams of Bloch modes in infinite PhCs and the properties of finite-sized PhCs. It is therefore necessary to study the evanescent modes and their role in matching the boundary conditions.

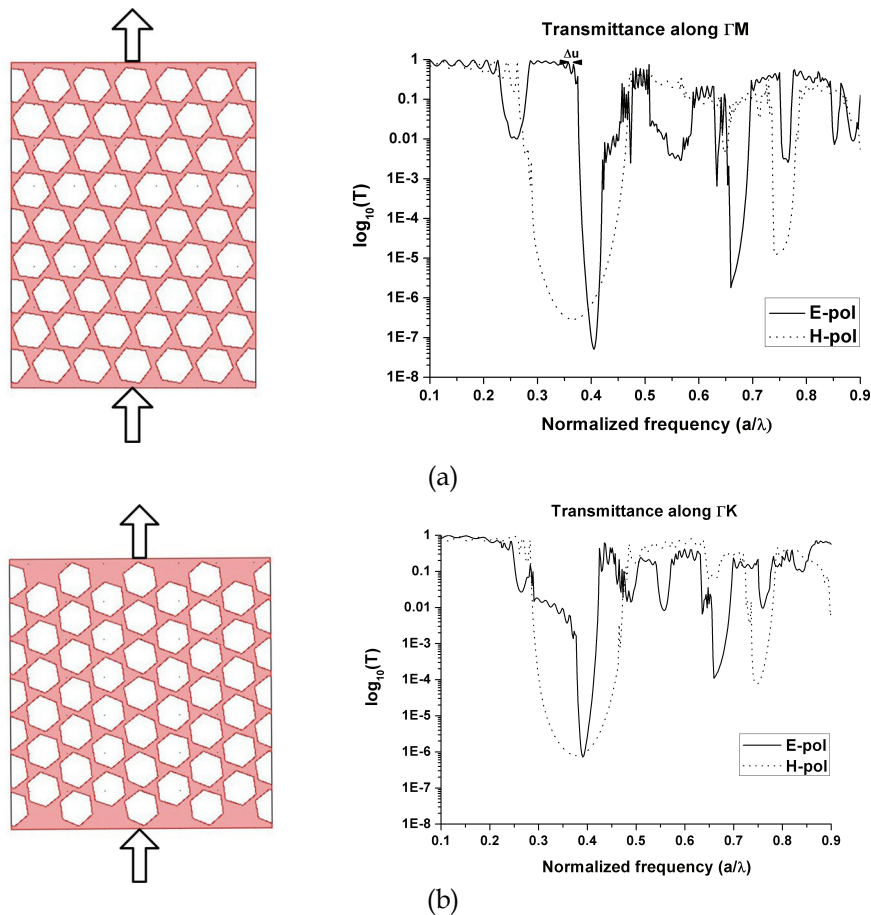


Figure 3.7 Finite-element calculations of transmittance along two main symmetry directions (ΓM and ΓK) of finite-sized hexagon-type samples (the same parameters as in Figure 3.6 are used here); results for E-modes and H-modes are represented with continuous and dotted lines, respectively

In the following we consider the transmission and reflection of electromagnetic waves coupled from an outside homogeneous medium into a

PhC made of a few layers of holes (Figure 3.7). The angle of incidence is along a given symmetry direction. If the frequency lies in the gap, the incident wave will be almost totally back-reflected, with extremely low transmission.

The computational domain has periodical boundary conditions in the lateral directions for E(H) polarizations, a matched boundary at the input interface and a 'low-reflecting' boundary at the output interface. At the input interface we apply a plane wave. The power outflow is monitored at the output interface. The transmittance is given by the ratio between the power outflow at the output interface and power inflow at the input interface. The frequency is scanned in the range $u=a/\lambda=0.1\dots0.9$ with 400 steps.

By comparing Figure 3.7 with Figure 3.6 we notice that the position and size of the PBGs are the same. However, for the higher-order PBG (at a normalized frequency of about 0.75), the transmittance dips (Figure 3.7) are several orders of magnitude smaller than for the first-order PBG (at a normalized frequency of about 0.4). This is another reason for considering the first-order PBG in the design.

Due to the interference between the electromagnetic wave reflected by the front and back surfaces of the sample a Fabry-Perot effect can be observed in the calculations of Figure 3.7. The high-frequency, low-amplitude fringes superimposed on the high transmission parts of the spectrum correspond to standing waves along the propagation direction in the photonic crystal. The number of transmission fringes is proportional to the PhC length. The free spectral range of the fringes (Δu) is directly related to the group velocity (v_g) and the cavity length (L) by [Moll 2003]:

$$\Delta u = \frac{v_g a}{2cL} \quad (3.6)$$

As the group velocity depends on the normalized frequency (u), equation (3.6) shows the dispersive character of PhCs. When u approaches the PBG edges where v_g decreases very much, Δu decreases, too (Figure 3.7). For example, at the lower gap edge for E-modes (around $u=0.376$) in Figure 3.7a, we determined numerically $\Delta u=8*10^{-3}$. The cavity length for the structure in Figure 3.7a is $L = (4\sqrt{3} + 1)a$; then, from (3.6) we obtain $v_g=0.127c$, value that is very close to the one calculated from the slope of the 2nd E-mode near Γ point (Figure 3.6).

Because the number of layers in the propagation direction is finite, the transmission will never be exactly zero*. The transmittance in the PBG drops exponentially with the number of layers. From Figure 3.7 is apparent that 6 layers give a transmittance of about 10^{-6} , which means an attenuation of about 10dB/layer. The major transmission dips outside the PBG in Figure 3.7 coincide with the partial gaps along ΓM and ΓK in Figure 3.6.

* This is the optical analogue of the phenomenon of tunneling in quantum mechanics that does not allow complete blocking by a finite potential barrier.

3.2. Photonic crystal slabs (PCSs)

Some of the most important applications of photonic crystals are based on introducing ‘defects’ in an otherwise perfect lattice by locally breaking the translational symmetry. A point defect can be a wavelength-scale resonant cavity with small modal volume and high quality factor [Villeneuve 1996]. A line defect can represent a waveguide that transfers light around sharp corners with high efficiency [Mekis 1996]. We will concentrate on the design of line-defect waveguides in Chapter 4.

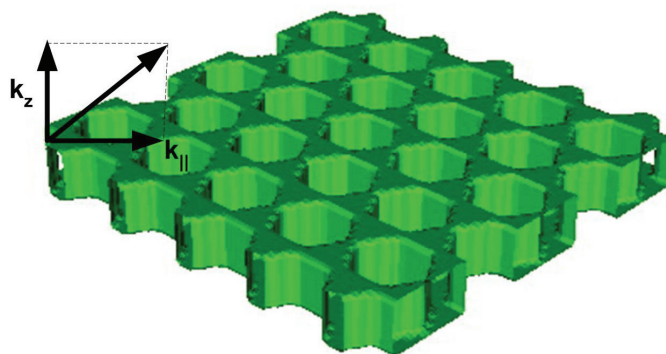


Figure 3.8 *Perspective view of a photonic crystal slab; in-plane and out-of-plane wave-vector components are indicated*

Anyway, the defects need to be shielded from the outside world to prevent radiation losses. Perfect shielding requires PhCs with full 3D PBGs. However, it is still extremely difficult to integrate 3D PhCs in the existing planar technology and to align them with optical coupling structures. Instead, the goal of 3D control of light propagation can be accomplished by using quasi-2D PhCs, known also as ‘photonic crystal slabs’ (PCS) [Meade 1994]. This kind of structures can be realized at submicron length-scales by using advanced lithographic and etching techniques.

A typical PCS structure (Figure 3.8) consists in a high-refractive index plate (e.g. Si, GaAs) perforated with a 2D periodic lattice of air holes and having a thickness around half-wavelength. The plate is sandwiched between two semi-infinite* regions that can be either homogeneous or patterned. Different examples of photonic crystal slabs are shown in Figure 3.11.

We have seen that in a 2D PhC the low-index material should have a high filling factor, in order to open a large PBG. The situation is different in 3D slabs intended for waveguiding applications. It has been shown [Ferrini 2003] that the scattering loss for in-plane propagation in PCSs is proportional to the area of air-holes. Therefore, in this case one should consider medium-sized holes that provide tradeoff between the gap size and scattering loss.

* considering the regions as a cladding it is sufficient that its thickness is much larger than the wavelength

3.2.1 Guiding mechanism

There are two coexisting confinement mechanisms in a PCS: in-plane confinement-given by the PBG effect- and vertical confinement-given by refractive index contrast between the PCS and its cladding. Because of its finite thickness, a PCS can support guided modes. The analysis of these modes should be three-dimensional and their properties depend on slab thickness, index contrast between the core and cladding, and vertical mirror symmetry.

3.2.2 Light cone

The dispersion relation in a homogeneous cladding with refractive index n_{cl} is:

$$\left(\frac{\omega}{c}n_{cl}\right)^2 = \left|\vec{k}_{\parallel} + \vec{G}\right|^2 + k_z^2 \quad (3.7)$$

where \vec{k}_{\parallel} is the wave-vector component in the plane of periodicity, belonging to the IBZ, \vec{G} is a reciprocal lattice vector and k_z is the wave-vector component perpendicular to the plane of periodicity (in the vertical direction).

The modes that obey the relation $(\omega n_{cl}/c) < k_{\parallel}$ ** have a purely imaginary k_z , so they decay exponentially in the cladding and they are confined into the core plane. These are *guided modes*, with a discrete spectrum. On the other hand, modes with real k_z are allowed to propagate infinitely in the cladding. These are *radiation modes* and they have a continuous spectrum sometimes referred to as ‘background’ [Johnson 1999]. It is apparent that, theoretically, there is no interaction between modes guided in PCS and radiation modes of the cladding.

The upper boundary of the region occupied by guided modes in the ω - k plane is called *light cone*, and is defined by $(\omega n_{cl}/c) = k_{\parallel}$. The area available to guided modes, which we call *transmission window*, scales roughly as $\sim (1/n_{cl})$. Figure 3.9 shows an example for a triangular lattice PCS with homogeneous claddings. A linear k -scale is applied parallel to each of the directions of the outer rim of the IBZ, leading to straight lines along the Γ -M and Γ -K directions and an approximately quadratic curve along the M-K direction. For a patterned cladding (e.g. Figure 3.11d) the light cone is the lowest band of the corresponding 2D photonic crystal.

** the higher-order Fourier components with $\vec{G} \neq 0$ have larger modulus and they automatically satisfy the inequality

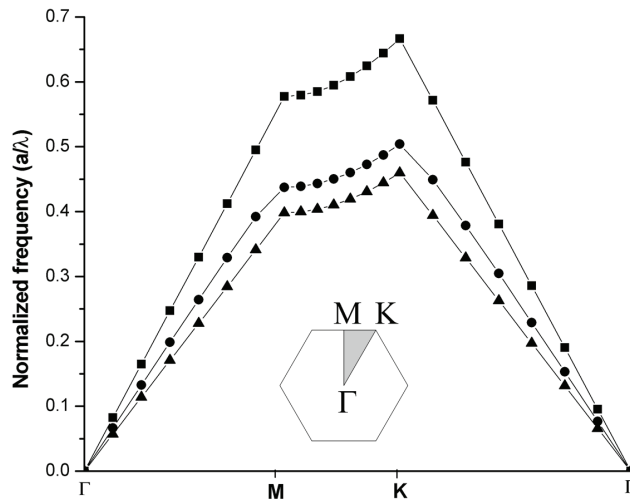


Figure 3.9 Light cone for three claddings: air (squares), homogeneous silicon dioxide (triangles), silicon dioxide patterned with hexagonal air holes having $r=0.41a$ (circles)

Modes above the light-cone are leaking into the cladding and they are subject to losses due to possible coupling with the radiation modes. These are called *leaky modes* or *guided resonances* [Fan 2002] and they are resonant states with a finite lifetime that translates into a finite quality factor (Q). In the next chapter we will refer in more detail to the quality factor of leaky modes in a line-defect waveguide.

In practice, one should consider all the modes (i.e. both guided and leaky) existing at a given frequency in a given propagation direction, because an incident wave can couple into any of them (symmetry matching should be considered, too).

3.2.3 Vertical supercell

The computational method used by MPB program requires a periodic cell. The PCS is patterned with a 2D periodic lattice and, in order to ensure 3D periodicity, we take a sequence of slabs periodical in the vertical direction. The primitive cell of the 3D periodical domain is called *supercell* (Figure 3.10). This encloses the PCS core and large portions of the claddings.

Guided modes are localized within the PCS core. Therefore, by taking the vertical period large enough (typically, equal to a few lattice constants), one can reduce the coupling among guided modes in adjacent slabs to a negligible level and calculate the frequencies of guided modes with high precision. The magnitude of the vertical wavenumber k_z is inversely proportional to the vertical period and establishes the phase relationship between adjacent slabs. This has a negligible influence on the eigenfrequencies of guided modes. Therefore, the path along which we calculate the band diagrams in PCSs is the same as in the 2D case (it corresponds to $k_z=0$).

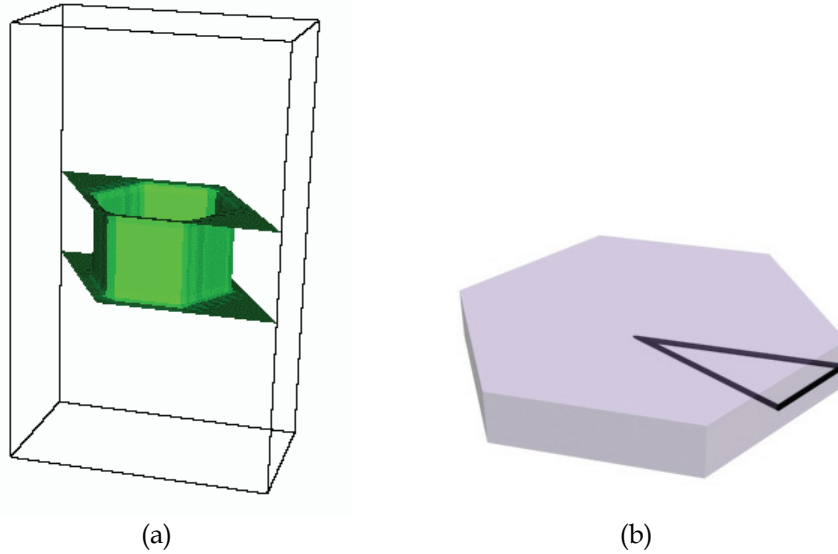


Figure 3.10 (a) Vertical supercell for air-bridge structure in Figure 3.11a; (b) 1BZ associated with the supercell, and the 2D path considered for calculating band diagrams in PCSs (see text for details)

However, the coupling between leaky modes is non-negligible, whatever the size of supercell. Thus, only guided modes dispersion curves can be calculated correctly by the supercell method. In order to calculate the leaky modes, one can use some of the methods presented in Chapter 2: SMM, FEM or FDTD. FEM and FDTD make use of PMLs on the top and the bottom of the calculation domain (which can be significantly smaller than a supercell).

3.2.4 Types of PCSs

The vertical index contrast of the slab system can be either low (e.g. GaAs-AlGaAs heterostructures) or high (e.g. SOI) depending on the technology. Low-index contrast structures do not have a gap in guided modes and operate usually above the light-cone. Their losses are quite high because the field is more extended into the claddings and is affected more strongly by the sidewall roughness (as shown in numerical calculations by Bogaerts *et al* [Bogaerts 2003]). High-index contrast structures can have gaps in guided modes, below the light-cone. Their intrinsic diffraction losses are relatively high, too.

An important aspect of PCSs is the vertical symmetry. When the cladding layers above and below the core are the same, the PCS is symmetric with respect to the centre plane of the core layer. Examples of symmetric PCSs are shown in Figure 3.11a, d. On the other hand, when the cladding layers are different (i.e. different materials and/or patterning) the PCS is asymmetric (Figure 3.11b,c). In symmetric PCSs the modes can be classified as even or odd with respect to the center plane of the core. The individual field components

have even or odd parity, but they do not have all the same parity. This follows from the transformation properties of E and H fields under spatial inversion. (i.e. E is a polar vector, whereas H is an axial vector). For example, if $z=0$ is the symmetry plane, the individual field components of an even mode will have the following parities: $E_x, E_y = \text{even}$, $E_z = \text{odd}$, $H_x, H_y = \text{odd}$, $H_z = \text{even}$. In the $z=0$ plane, even and odd modes are polarized in the same way as H-modes and E-modes in 2D PhCs, respectively (for example, the non-zero components of an even mode in $z=0$ plane are all even - H_z, E_x, E_y - like in a H-mode in 2D). Based on this analogy, we call even and odd modes H-like and E-like modes, respectively*.

The most common implementation of high-index contrast PhC slabs is the ‘air-bridge’ (Figure 3.11a). It consists of a 2D lattice of holes in a thin high-index membrane surrounded by air. This structure has a very good field confinement, vertical symmetry (in theory; in practice, however, this is very difficult to achieve) and largest transmission window (i.e. area in the band diagram available to guided modes, in the gap below the light cone). However, the fabrication technology is quite involved and large area slabs may have a low mechanical stability.

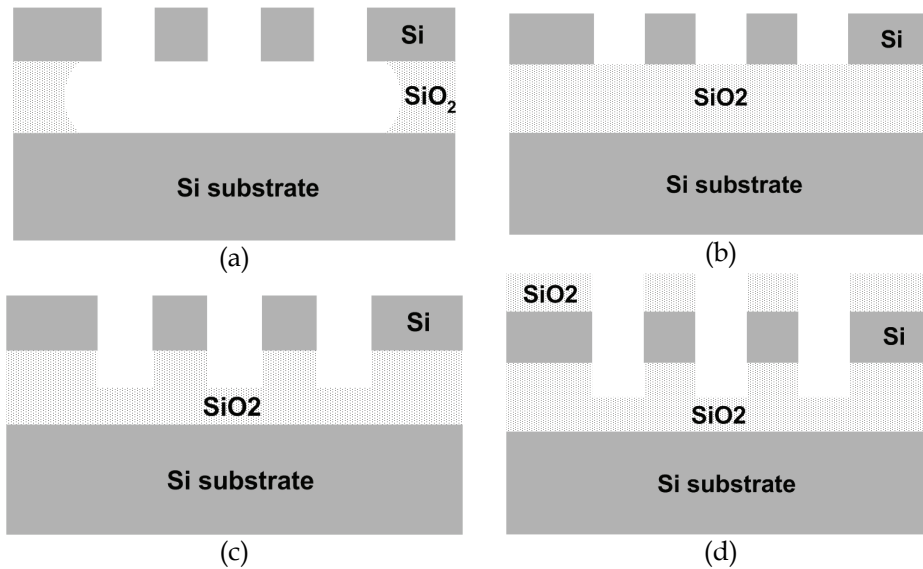


Figure 3.11 Four configurations of PCS based on SOI: (a) air-bridge, bottom cladding removed; (b) solid bottom cladding; (c) etched bottom cladding; (d) core sandwiched between etched claddings

A different configuration consists in a silicon PhC slab on solid silicon dioxide cladding (Figure 3.11b). Even though mechanical stability is much improved and fabrication technology is simplified, this structure has a high

* in a 3D slab with weak asymmetry modes are classified as ‘quasi H-like’ or ‘quasi E-like’

degree of asymmetry and a lower transmission window. Moreover, higher losses due to radiation towards the substrate are to be expected; a thick SiO₂ buffer layer is required for bringing the losses down to an acceptable level. A compromise solution, combining the advantages of the two variants discussed above is to use a quasi-2D SiO₂ slab as a bottom cladding (i.e. the air holes penetrating both Si and SiO₂ layers of a SOI wafer)-see Figure 3.11c. Etching the air holes into the bottom cladding has beneficial effects: it decreases the asymmetry and increases the frequency range below the light cone, available for truly guided modes. Moreover, the etch depth can be moderate, because of the high-index contrast. Finally, another possibility would be to use two quasi-2D SiO₂ slabs as claddings (Figure 3.11d), in order to ensure both vertical symmetry and mechanical stability. However, the fabrication of such a structure poses serious fabrication problems, mainly due to the necessary alternating etching steps.

3.2.5 Band diagrams of guided modes

Up till now, theoretical and experimental studies have almost exclusively concentrated on the mirror-symmetric slab with a triangular lattice of circular air holes. This configuration is known to have a large gap in guided H-like modes between the first two bands and a smaller gap for E-like guided modes. Under certain circumstances [Jamois 2002], these gaps can be made to overlap, leading to an absolute gap of about 8.5%. In general, E-like modes did not receive much attention. In practice it is very difficult to achieve *perfect* vertical symmetry and mode coupling due to symmetry breaking may be critical [Tanaka 2003].

Here, a gap is a range of frequencies in which no guided modes exist. It is not a complete gap, because of the radiation modes present above the light-cone. Still, a gap in guided modes is useful for introducing, in a controlled way, 'defect' states. An absolute gap, independent of mode symmetry, would be a desirable feature [Bostan 2002a]. There are several reasons to support this statement. First, coupling between modes of opposite symmetry is possible in real structures. Because of intrinsic fabrication imperfections, the boundaries are neither smooth nor straight. Roughness-induced scattering at the boundaries is important in a PCS where the number of boundaries is large. Second, a reasonable coupling efficiency between PCS and a ridge waveguide would need careful control over the polarization state. Third, the condition of mirror symmetry leads to an increase in the complexity of the fabrication process in certain cases (for example, when using silicon-on-insulator -SOI wafers).

Unlike guided modes in homogeneous slab waveguides, the guided modes in a PCS have both a lower and a higher cutoff frequency. The fundamental mode lies in the long wavelength range.

An important parameter in the design of PCSs is the core height (h). When the height is very small compared with the wavelength the slab modes are only very weakly guided (this implies that a larger vertical supercell is required). There may be only one guided band just beneath the light line. On

the other hand, if the slab is made too thick, higher order modes are shifting down in frequency and can enter the gap, reducing its size or even closing it. During the numerical experiments we observed that, when h is varied, the frequencies of odd modes are shifting at a higher rate than the frequencies of the even modes. Besides, for a fixed parity, higher order modes are shifting faster than the lower order ones. Thus, h can be used for optimizing the absolute gap size.

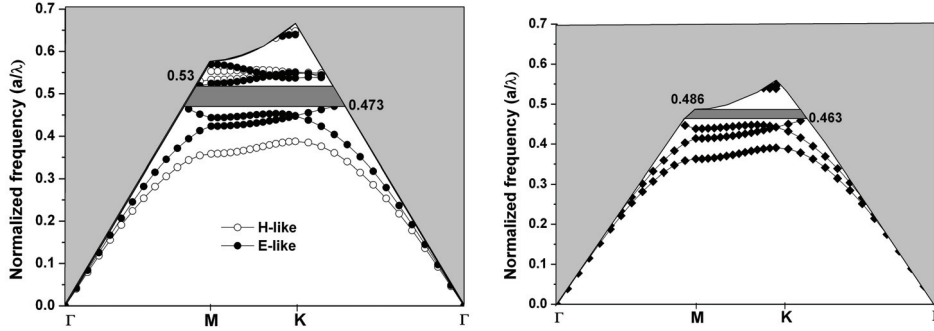


Figure 3.12 Band diagram of guided modes in a SOI hexagon-type PCSs: (a) air-bridge; (b) asymmetric structure with air upper cladding and SiO_2 bottom cladding with air holes etched through it; parameters: $r=0.5a$, $\theta=9^\circ$, $h=0.59a$

Large absolute gaps are achievable in hexagon-type mirror-symmetric PCSs [Bostan 2002a]. Depicted in Figure 3.12a are band diagrams of guided modes in a hexagon-type air-bridge PCS with optimum thickness $h=0.59a$. The absolute PBG is bounded by the second and third odd modes and the light cone and has 11.3% width. When the hexagon-type PCS is asymmetric, with air and deeply etched silicon-dioxide ($n_{\text{SiO}_2}=1.45$) upper and bottom claddings, respectively, the holes need to be etched through, deeply into the SiO_2 in order to maximize the bandgap. The resulting PBG for this case is reduced to 4.84%, as shown in Figure 3.12b. This happens because the light cone, which acts as a filter, is shifted towards lower frequencies.

However, these absolute gaps manifest themselves only below the light cone. As soon as the dispersion curves of guided modes reach the light cone boundary and become guided resonances, they cross the gap; then mode coupling between guided and leaky modes is likely and this leads to propagation losses. The absence of guided modes in a frequency region has potential applications in light extraction enhancement from a point-like cavity, through increasing the in-plane quality factor. The gaps in guided modes obtained for high air filling factors are situated at higher frequencies. This has a number of practical disadvantages when linear defects are introduced: (i) The higher frequencies in the band diagram are more sensitive to small variations in geometry parameters (due to e.g. fabrication imperfections); (ii) Propagation losses are roughly proportional with the area of air holes [Ferrini 2003].

Instead of aiming at an absolute gap, we can focus on the spectral range bounded by the fundamental E-like and H-like modes [Qiu 2002a] This region

is pretty large even for moderate sized air holes and is suitable for introducing 'defect' states. Because there are no resonances in this range, it is possible, in principle, to obtain lower propagation losses [Tanaka 2003].

We choose medium-sized holes with $r=0.41a$ and $\theta=0^\circ$. The resulting band diagram is presented in Figure 3.13. There are two gaps in guided modes: one between the 1st and the 2nd H-like modes, and one between 4th and 5th E-like modes.

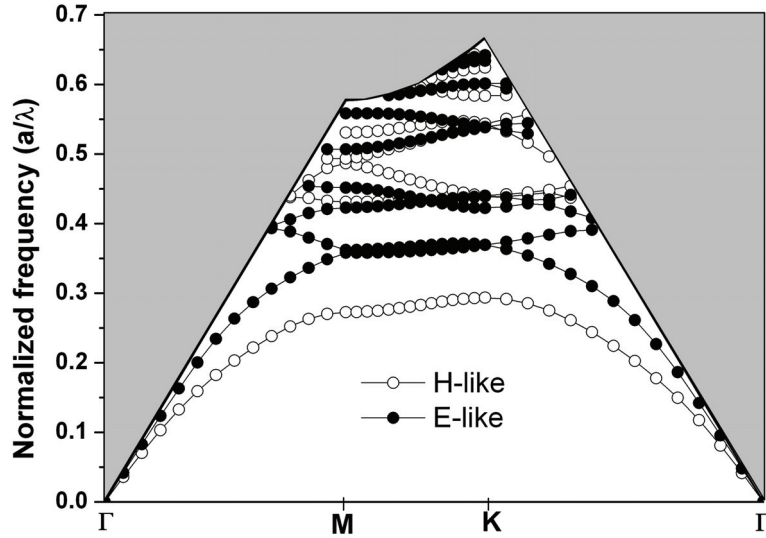


Figure 3.13 Band diagram of guided modes in a silicon air-bridge hexagon-type PCS; $r=0.41a$, $\theta=0^\circ$, $h=0.59a$

For the reasons mentioned above, we choose our working wavelength in the range $u=(0.29\dots0.35)$ which is in the gap of guided H-like modes. The tolerance of gap width with respect to h is addressed in Figure 3.14

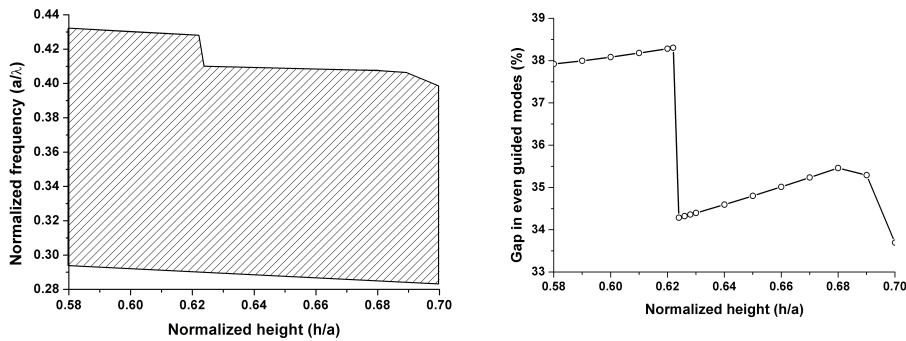


Figure 3.14 Variation of even modes' gap position (a) and size (b) with respect to core height for the structure considered in Figure 3.13;

For $h>0.62a$ the 3rd H-like mode suddenly falls into the gap of E-like modes, reducing its size with about 4%. The bands are shifting continuously with h ,

but upper bands are shifting faster. That is why the drop of gap width is step-like.

3.2.6 Effective index approximation

Rigorous modeling of PCS structures requires 3D calculations that are very demanding in terms of time and memory requirements. Effective index approximation of the PCS has been used for relieving these requirements by reducing the full 3D calculations to simpler, though approximate 2D calculations [Qiu 2002b]. The PCS is essentially a slab system perforated with a lattice of holes. In the effective index method, the PCS is replaced by a 2D system with the background dielectric medium having the effective refractive index of the fundamental guided mode of the slab system.

In high-index contrast systems (like SOI) the effective index approximation is valid for a narrow frequency range in which the guided mode dispersion is small enough. To avoid complications due to possible coupling to higher order modes, we choose a slab system that supports only a single mode for each polarization. For an asymmetric slab system consisting in a core with refractive index n and height h , sandwiched between two claddings with refractive indices n_1 and n_2 ($n_1 < n_2$), the single-mode condition for a free space wavelength λ_0 is [Yariv 1984]:

$$h_{\max} = \frac{\lambda_0}{2\pi} \cdot \frac{1}{\sqrt{n^2 - n_2^2}} \cdot \left[\pi + \tan^{-1} \left(\sqrt{\frac{n_2^2 - n_1^2}{n^2 - n_2^2}} \right) \right] \quad (3.8)$$

Our design parameters are: $\lambda_0 = 1.55 \mu\text{m}$, $n = 3.45$ (Si), $n_1 = 1$ (air) and $n_2 = 1.45$ (SiO₂). Then the maximum thickness for single-mode, according to equation (3.8) is $h_{\max} = 273 \text{nm}$. We choose a core thickness $h = 260 \text{nm}$. The effective indices of H and E guided modes will be: $n_{\text{eff}}^H = 2.924$ and $n_{\text{eff}}^E = 2.24$.

The lattice constant, $a = 500 \text{nm}$, is chosen to correspond to a normalized frequency $u = 0.322$, approximately in the middle of the gap between fundamental H-like and E-like modes. The band structure of the PhC slab for $r = 0.41a = 205 \text{nm}$ and $\theta = 0^\circ$ has been calculated in 2D using this effective index approximation. The results are shown in Figure 3.15 where the results from a full 3D calculation are included for comparison.

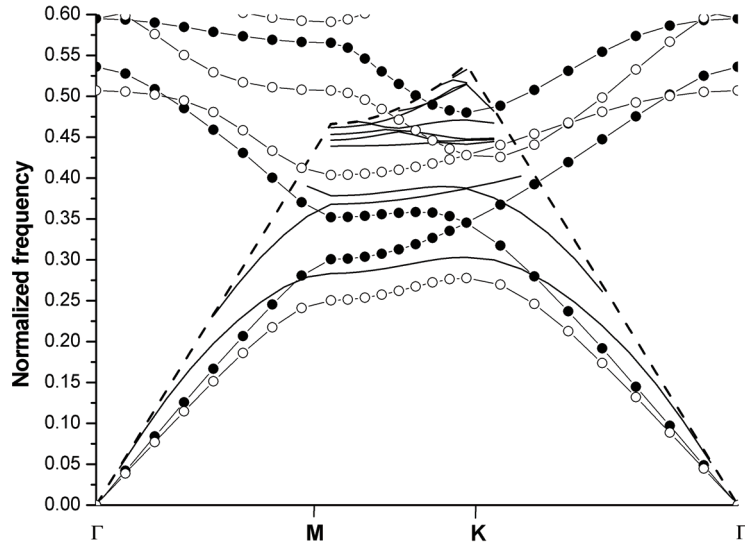


Figure 3.15 Comparison between the 2D bands calculated using effective index and 3D bands of the PCS shown in Figure 3.11c (open circles-H modes, filled circles-E modes, continuous line-3D bands, dashed line-light cone)

Although bands are shifted upwards in frequency in the 3D case, the shape of the lowest order bands is roughly preserved, allowing conclusions regarding the quasi-symmetry of modes in 3D. The effective index approximation can be efficiently applied for qualitative design of 3D photonic crystal structures (slabs and line defect waveguides).

3.2.7 Loss mechanisms

The real-world PCSs are not perfect and this has an impact on their performance especially with regard to losses. There are several loss mechanisms. First, there are the *intrinsic losses* due to diffraction produced by the lattice of holes. These losses are the lower limit one might expect. The *extrinsic losses* due to fabrication imperfections are typically one order of magnitude higher than the intrinsic ones. There are many factors contributing to the extrinsic losses: limited etch depth (e.g. when holes are penetrating the bottom cladding, see Figure 3.11c,d), roughness, tapered sidewalls, disorder. The extrinsic factors may be controlled by improving the fabrication technology (e.g. lithography, dry etching). How all these loss factors are reinforcing or are counteracting each other is very difficult to say. Instead, researchers have considered one loss mechanism at a time.

Intrinsic losses have been analyzed by Bogaerts *et al* [Bogaerts 2002a]. They found that in a high-index contrast PCS the losses drop suddenly when a lossless Bloch mode is excited. This is possible in SOI structures considered in this thesis. Tanaka *et al* [Tanaka 2003] have tackled the losses induced by tapered sidewalls. The vertical symmetry is broken and coupling between E-

like and H-like modes gives rise to losses that are approximately proportional to the square of taper angle. Nevertheless, the losses can be very much reduced when the working frequency is between the fundamental E-like and H-like modes. Ferrini *et al* [Ferrini 2003] developed further an analytical model for out-of-plane scattering, originally proposed by Benisty *et al* [Benisty 2000]. This model treats scattering from individual holes incoherently and translates the losses into an effective imaginary index in the air holes, to be used in a 2D calculation. The effective imaginary index scales approximately linearly with the filling factor f and quadratically with the normalized frequency u : $\varepsilon'' \sim u^2 f$. Light is not guided in the holes but is scattered and might be lost. This gives another reason why we should select the working frequency close to the lowest band edge where the modes have their minima in the holes.

Scattering losses due to sidewall roughness have been studied by Bogaerts *et al* [Bogaerts 2003] in a simplified 2D model. The irregularities on the sidewalls are seen as radiating dipoles excited by the guided modes. The emission from these dipoles depends both on index contrast and on the interaction area. In high-index contrast the scattering is strong, but there are other factors that can give a lower overall scattering than in low-index case: (i) the slab waveguide has a higher numerical aperture, thus it can re-capture a significant part of the scattered light; (ii) the guided mode has a stronger confinement, thus the rough area exposed to interaction is smaller.

The discussion in this section refers to PCSs without ‘defects’. The situation is somewhat different when line defects are introduced. The overlap between the guided mode in a dielectric channel and neighboring air holes can be smaller than in a PCS. However, the main conclusions of this section (i.e. use a lower working frequency and moderate-sized holes in order to reduce the losses) are valid for line defect waveguides, too. We will refer to the losses in line defect waveguides in the next chapter.

3.2.8 Discussion

An SOI-based PCS can be used as a platform for integrating “defects”, e.g. point-like cavities and line-defects. Depending on application, the design rules might differ. Here we address them briefly.

Vertical symmetry of a PCS is desirable because it allows more freedom in controlling mode coupling and selective mode excitation.

The air-bridge PCS seems to have the best performance for all application, despite its lower mechanical stability as compared to other types of PCS: the substrate leakage loss is minimum, it is vertically symmetric, the transmission window is the largest achievable.

The choice of the lattice configuration depends on the application. With high air filling factors achieved by rotating the hexagonal “atoms” one can obtain absolute gaps in guided modes situated at higher frequencies in the band diagram. Then, a “defect” mode of a point-like cavity emitter will couple only to leaky and radiation modes and the extraction efficiency will be increased.

For line-defect waveguides it is essential to keep the losses down to a level as low as possible. This asks for a low working frequency and a moderate

filling factor. Then an absolute gap is not possible, and one has to rely on a partial gap (the gap between fundamental E-like and H-like modes seems the most promising alternative).

The slab thickness has an optimum value, which gives the best mode confinement in the PCS core layer.

Chapter 4 Design of line-defect waveguides in photonic crystals

4.1. Waveguiding mechanisms

What is the motivation of using PhC-based waveguides instead of conventional waveguides? In conventional slab-based waveguides the energy distribution has a tail extending in the claddings and the waveguiding relies on ‘total internal reflection’ (TIR). When the waveguide turns a bend TIR condition is broken and energy leaks away from the waveguide. On the other hand, in a PhC-based waveguide the lateral ‘walls’ are ‘metallic-like’ because the wave is strongly attenuated inside them for frequencies in the PBG. Then, sharp bends in PhC-based waveguides are possible, in principle, because in-plane radiation losses are suppressed.

A line defect waveguide* can be made, for example, by omitting an entire row of holes from a 2D crystal lattice of air holes in silicon (see Figure 4.1 and Figure 4.8)

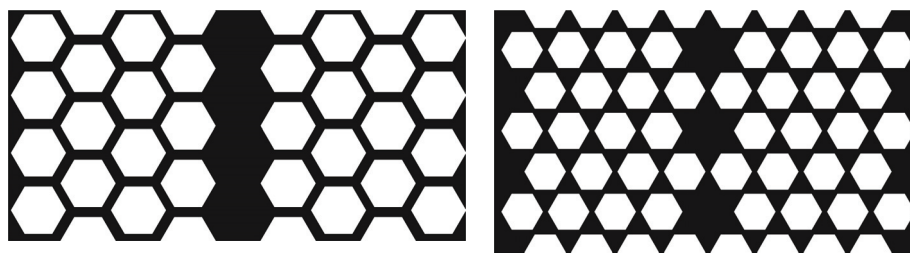


Figure 4.1 Two examples of line-defect waveguides along high symmetry directions Γ -K (left) and Γ -M (right)

Because we are increasing locally the amount of high-index material, the frequencies of some modes from the upper PBG edge will be reduced, and they will be pulled down into the PBG region, forming ‘defect’ states. These states (which can be called ‘donor-type’ in analogy with semiconductor physics) will be localized along the line defect, because of the PBG effect that prohibits propagation in the lateral direction. This phenomenon is called ‘gap confinement’ (GC) [Yamada 2001]. But even for frequencies outside PBG light localization along the line defect is possible, due to the effective index contrast between the waveguide and its lateral ‘walls’. This is called ‘index

* Strictly speaking, a line defect waveguide in a 2D PhC would consist of a single modified (infinitely long) hole, so it would be a “plane” defect in 2D; however, since “line defect” is a well-established term in the literature, we will use it both in 2D and 3D

confinement' (IC) [Yamada 2001] and is independent on the existence of a PBG. For a line defect waveguide in a PCS, the confinement in the vertical direction is of the IC-type, provided by the refractive index contrast between the slab core and its claddings.

4.2. Projected band diagram

A line defect waveguide has 1D translational symmetry along its axis. The 1BZ collapses to a line interval because the only meaningful wave-vector component (named here β) is the one parallel to the line defect. The 1BZ's for line-defect waveguides along Γ -K and Γ -M are $(0, \pi/a)$ and $(0, \pi/a\sqrt{3})$, respectively.

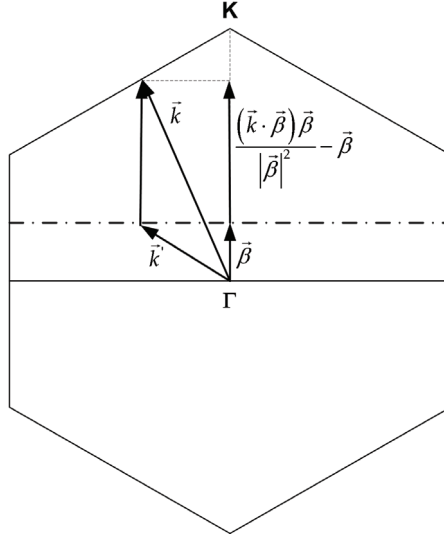


Figure 4.2 Illustration of the projection procedure for obtaining the wave-vectors in the case of a line-defect along Γ -K (see text for details)

The analysis of guided modes requires a new representation of the band structure. We call this the *projected band diagram*. The projection procedure is shown in Figure 4.2. First, we fix $\vec{\beta}$. Then, the \vec{k} -vectors belonging to the edge of the *full* 1BZ of the original lattice (without 'defect') are projected onto the line that is orthogonal to $\vec{\beta}$ and passes through it (dash-dotted line in Figure 4.2). In this way, the point \vec{k} on the edge of the original 1BZ is mapped into a new point \vec{k}' , which can be expressed as function of \vec{k} and $\vec{\beta}$:

$$\vec{k}' = \vec{k} - \frac{(\vec{k} \cdot \vec{\beta})\vec{\beta}}{|\vec{\beta}|^2} + \vec{\beta} \quad (3.9)$$

The significance of equation (3.9) is that we take all the interior points of the 1BZ that have their projection on $\vec{\beta}$ equal to β . Finally, the wave-number β is scanned in the 1BZ of the line-defect and the normalized frequencies corresponding to $k'(\beta)$ in the defect-free PhC are plotted as a function of normalized β ($= \beta a / (2\pi)$).

Introduction of a line defect can break all the symmetries of the original lattice. That is why we have to consider the full 1BZ. Waveguides along high-symmetry directions Γ -K and Γ -M (Figure 4.1) can still have mirror symmetry with respect to their middle axis; their modes can be classified as ‘even’ or ‘odd’ with respect to this axis. In 3D, the light cone of a PCS will be projected and become the *light line*. In the 1BZ of the line defect the light line is a line passing through the origin, with an inverse slope given by the effective index of the highest-index cladding.

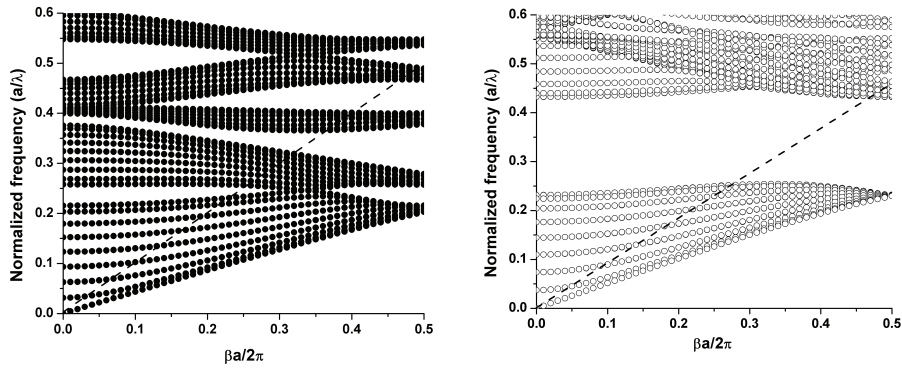


Figure 4.3 Projected band diagrams along Γ -K for hexagon-type 2D PhC with $r=0.45a$ and $\theta=30^\circ$: E-modes (left) and H-modes (right); the air light line is dashed. The bands indicate PhC slab modes that can be excited by a given β in a predetermined direction (Γ -K here).

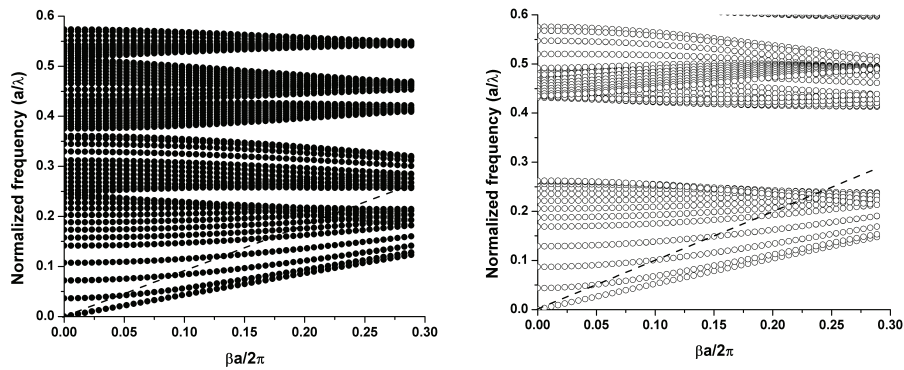


Figure 4.4 Projected band diagrams along Γ -M for hexagon-type 2D PhC with $r=0.45a$ and $\theta=0^\circ$: E-modes (left) and H-modes (right); the air light line is dashed

The projection creates continua of states (combinations of $\omega-k$) that are allowed to propagate in the bulk photonic crystal and reveals the projected gap between these states. The band projection can be done along $\Gamma-K$ (Figure 4.3) or $\Gamma-M$ (Figure 4.4). For the projection along $\Gamma-M$, the gap region below the light line is very much reduced in comparison with the projection along $\Gamma-K$. Since this region is the window of lossless waveguiding, in what follows we will consider only waveguides along $\Gamma-K$.

The existence of a projected gap does not require the original crystal to have a complete bandgap. In other words, an incomplete gap is sufficient for straight waveguides. However, when straight waveguides are combined into more complex devices, like bends and Y-junctions, only an omnidirectional gap can prevent scattering losses into the surrounding photonic crystal.

4.3. Lateral supercell approach to ‘defect’ modes

Line defect waveguides can be modeled by using a lateral supercell approximation. Unlike the ‘vertical’ supercell used for PCS’s, here the supercell is ‘lateral’*. For convenience, in this section we will use the term supercell alone and suppress the term ‘lateral’.

The supercell is a rectangular domain with a width (transverse to the line defect) equal to a few lattice constants and a length of one period (along the line defect). A proper choice of the supercell should contain an integer number of primitive cells of the original lattice.

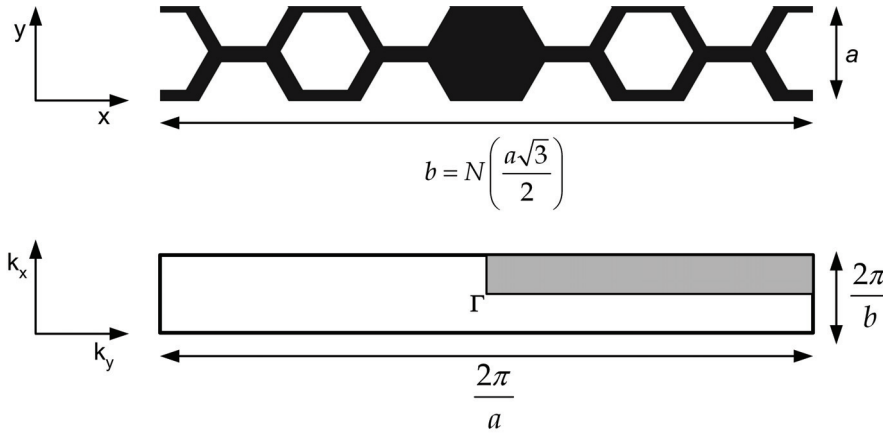


Figure 4.5 Example of a supercell and its related 1BZ, for a line defect along $\Gamma-K$; the supercell contains $N=8$ primitive cells; the 1BZ has been rescaled, for clarity, and the shaded grey region is its irreducible part

In the computation, we apply Bloch boundary conditions on the supercell sides. This means that we are practically considering a periodic array of waveguides, where the separation between them is determined by the

* For line defect waveguides in 3D PCS’s, the supercell is a combination between ‘vertical’ and ‘lateral’ supercells

supercell width. The width should be large enough in order to minimize the coupling between guided modes in neighboring waveguides.

As explained in Chapter 1, the unit cell and its associated 1BZ are the inverse of each other. Then, if a supercell is N times bigger than a primitive cell, its 1BZ will be N times smaller than the 1BZ of the original crystal (see Figure 4.5). An example of supercell and its related 1BZ is shown in Figure 4.5. Because the wavevectors that differ by $(2\pi/b)$ are equivalent, the bands of the primitive cell are folded back and forth N times at the edge of the 1BZ. At the limit $N \rightarrow \infty$ the supercell 1BZ reduces to a line ($k_x \rightarrow 0$) and the band folding produces continua of bulk states, plus discrete ‘defect’ states, corresponding to localized modes. The number of bands one needs to calculate in order to reach the projected gap region is N times more than in the case of perfect periodic lattice (due to the band folding effect).

The band folding obtained by using the supercell approach is equivalent to the primitive cell band projection. For a finite supercell the bulk states’ frequencies are slightly shifted. The exact location of the projected gap should be obtained by projecting the primitive cell bands in the direction of line defect waveguide. If the supercell is large enough, a guided mode’s frequency will not depend on k_x . Therefore, in a supercell calculation k_x can be taken zero.

Projected band diagrams of line defect waveguide along Γ -K are shown in Figure 4.6.

By comparing Figure 4.6 with Figure 4.3 we notice the presence of several discrete ‘defect’ bands in the projected gap below the light line. This is clearer for H-modes, for which there are 3 well-separated guided modes.

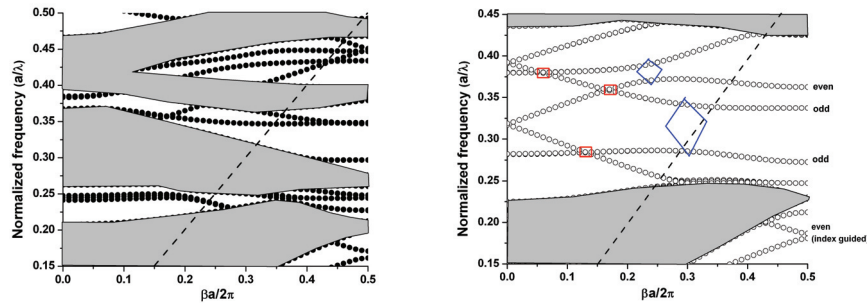


Figure 4.6 Projected band diagrams obtained by supercell calculations of a line defect in a 2D PhC (the lattice parameters are equal to those of Figure 4.3): E-modes (left) and H-modes (right); guided modes appear in the projected gap region; crossings and anticrossings between dispersion curves are marked with rectangles and rhombuses, respectively.

A waveguide made by omitting a row of holes in an otherwise periodic slab (so-called W1 waveguide) is symmetric with respect to its middle axis, and the guided modes can be classified as odd and even with respect to it. The field patterns of these modes show localization along the ‘defect’ (Figure 4.7 first three panels). A peculiar mode is the one below the projected continuum in Figure 4.6 right panel. This is an index-guided mode whose field profile

(Figure 4.7 bottom panel) resembles closely the fundamental guided mode in the equivalent ridge waveguide.

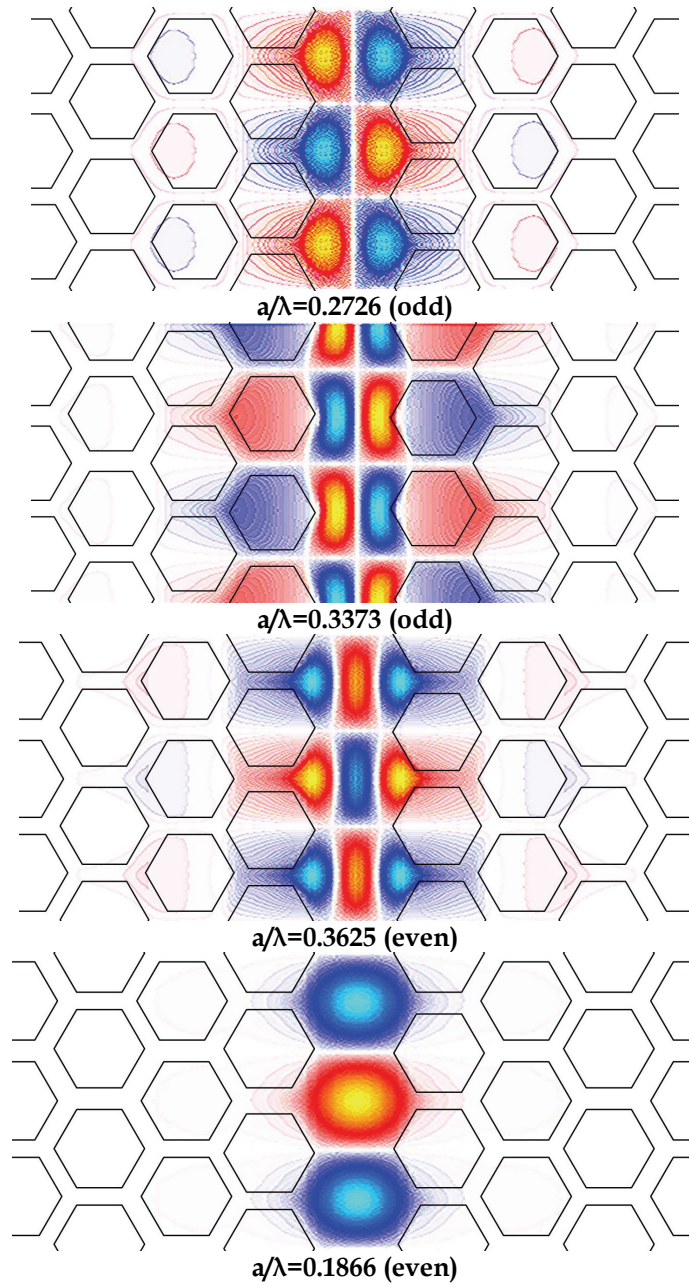


Figure 4.7 Field profiles of H modes: gap-guided (first 3 panels) and index-guided (bottom panel); parity is defined with respect to the middle axis along the waveguide; normalized frequencies at the edge of IBZ are indicated

4.4. Propagation phenomena in line defect waveguides

4.4.1 Index guiding

Index-confined (guided) E and H modes exist below all the bulk states of the photonic crystal surrounding the ‘defect’ waveguide (Figure 4.6). For these modes the photonic crystal is a medium described by an average refractive index lower than the silicon core [Loncar 2000]. For a more specific discussion, we refer here to the index-guided H mode in Figure 4.6–right panel. The index-guided mode does not have an upper cutoff frequency. Therefore, its frequency increases monotonically and its dispersion curve is folded back and forth in the IBZ. The dispersion curve reaches the edge of the IBZ at $(\beta a/2\pi, a/\lambda)=(0.5, 0.1866)$ where it is folded back, then the frequency continues to increase and at $(0, 0.319)$ folding takes place once again. Along its trajectory, the index-guided mode encounters the bulk modes and interacts with them by leaking energy into the surrounding PhC, and has crossings and avoided crossings (anticrossings) with gap guided modes (Figure 4.6 right panel): (i) crossing with the first gap guided odd mode at $(0.13, 0.284)$; (ii) crossing with the second gap guided odd mode at $(0.17, 0.36)$; (iii) anticrossing with the gap guided even mode $\beta a/2\pi = 0.23$.

4.4.2 Crossings and anticrossings

In a W1 waveguide along a Γ -K direction, the lateral walls of the dielectric channel are corrugated by the neighboring rows of air holes. The corrugation is a periodic modulation of the refractive index along the waveguide axis, with periodicity a , and associated reduced Brillouin zone $(0, \pi/a)$. Therefore, a W1 waveguide looks like a 1D photonic crystal. The mechanism of gap opening and band flattening (i.e. zero group velocity) at $\beta a/2\pi = \pi/a$ can be explained in terms of destructive interference between the forward propagating waves and the waves that are contra-directionally Bragg coupled by the corrugation [Agió 2001]. Partial back-reflections from individual corrugations interfere constructively (effect known as ‘distributed Bragg reflection’ – DBR), gradually converting the forward propagating wave into a backward propagating one. The energy cannot flow along the waveguide, a phenomenon known as *mode gaps* or *ministop bands*. This also explains the low group velocity, especially at the edge of the line-defect Brillouin zone (which is below the light line). The DBR effect depends on the interaction length but, for line defect waveguides longer than some minimum length, it does not significantly change with the length of the waveguide [Adibi 2001b].

Being symmetrical, the corrugation can couple only the modes with the same parity propagating in both directions along the waveguide. Dispersion curves of modes with opposite parity can cross, regardless of mode order, while the ones of modes of same parity and different order repel each other, producing anticrossings. These anticrossings give rise to mode gaps [Agió 2001]. When the corrugation is non-symmetric (e.g. when two rows of holes

are removed, in a W2 waveguide) coupling between modes of opposite parity becomes possible and this produces anticrossings at their virtual intersection points.

4.4.3 Group velocity and transmission bandwidth

Usual W1 waveguides have several guided modes in the gap, so that there is no truly single-mode range available [Loncar 2001]. These modes are pulled down from the upper gap edge and are flat at the Brillouin zone boundary. Thus, they span a narrow frequency range and have a low group velocity, features that are not desirable in applications that require efficient transmission of light signals in telecom applications. It is worth mentioning that a low group velocity is useful for enhancing nonlinear optical interactions and for special functions like delay lines. A small transmission window means that the mode is susceptible to structural disorder [Notomi 2002] that can shift its dispersion curve. Optical fibers or ridge waveguides are characterized by dispersion curves with pretty steep slopes. This means that their modal refractive indices are relatively low compared to those of gap-guided modes in Figure 4.6. There is a quite large impedance mismatch between ridge waveguides and photonic crystal W1 waveguides, which makes coupling of light into the photonic crystal waveguide difficult.

4.4.4 Out-of-plane radiation loss and quality factor

In a line defect waveguide the electromagnetic energy flows along its direction with a speed given by the projection of the group velocity \bar{v}_g along this axis (suppose v_{gy}). A leaky mode (i.e. situated above the light line) travels* a distance L in the time interval (L/v_{gy}) , and, simultaneously, is subjected to out-of-plane loss (coupling to radiation modes). Then, the electromagnetic energy decays exponentially as a function of traveled distance [Moll 2003]:

$$U(L) = U(0) \exp\left(-\frac{\omega_0 L}{Q v_{gy}}\right) \quad (3.10)$$

where ω_0 is the central frequency of the mode and Q is its quality factor (inversely proportional with mode's lifetime)

The propagation loss per unit length is given by the damping factor:

$$\alpha = \frac{\omega_0}{Q v_{gy}} \quad [m^{-1}] \quad (3.11)$$

Several design rules for loss minimization can be inferred from equation (3.11):

* A different situation occurs in point defect cavities, where standing waves are formed

- the photonic bandgap should be situated at low normalized frequencies;
- the leaky mode should have a group velocity as high as possible;
- the coupling with the radiation modes should be as low as possible, in order to increase the quality factor.

It is difficult to control and predict the quality factor Q ; it may be evaluated using involved 3D FDTD calculations and data postprocessing. However, it is intuitively clear that, in order to get a high Q , the mode should be well confined in the waveguide core and should have only a weak overlap with the air holes. The index-guided mode satisfies these criteria and can be practically used for efficient propagation above the light line [Desieres 2002] along short distances (on the order of 100 μm).

4.5. Band diagram engineering

Practical applications of line defect PhC waveguides in telecom require the fulfillment of several conditions [Yamada 2002] [Loncar 2001]:

- The waveguide should have a single-mode behavior in the frequency range of interest, in order to avoid mode mixing that complicates signal coupling and transmission;
- The frequency range to be used for transmission should be positioned below the light line; then, the mode is theoretically lossless
- The dispersion curve of the guided mode should have a reasonably steep slope; this is important for efficient energy transport and loss reduction;
- The guided mode should be positioned at lower frequencies, at the same time far enough from the gap edges; in this way, the losses are reduced and coupling between the guided mode and bulk states is avoided;
- Unwanted leaky modes should not intersect the projected gap; the external source characterized usually by a fixed frequency may excite these modes, leading to a decrease in coupling efficiency.

In a W1 PhC waveguide not all these conditions are satisfied. Therefore, engineering the 'defect' waveguide should be done, along the following lines:

1. reducing the amount of high-index material in the waveguide core; this has the effect of pushing the higher-order 'donor-type' modes at higher frequencies, out of the gap and a single mode regime might be achieved; care must be taken to not pull up in the gap some undesired 'acceptor-type' modes from the lower band edge;
2. reducing the refractive index modulation along the waveguide by changing the corrugations size, shape and/or position; this will lead to increased group velocity, reduced losses and enhanced coupling with the ridge waveguides.

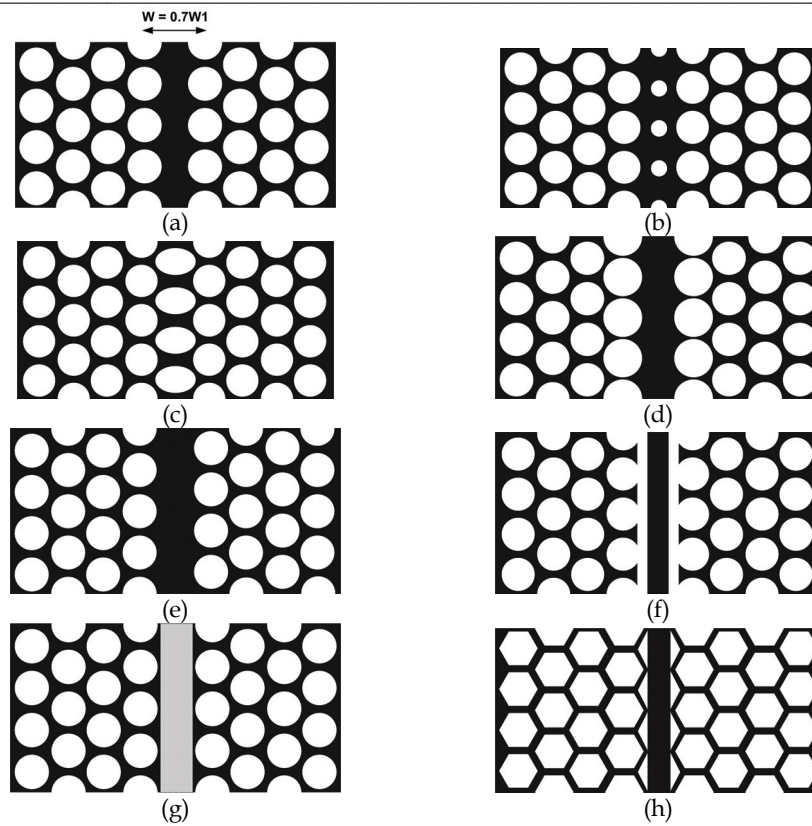


Figure 4.8 Means of tuning the mode dispersion in a line-defect waveguide:

- (a) reducing the waveguide width by displacing blocks of holes with respect to the original lattice [Notomi 2002];
- (b) reducing the hole-size and shifting with half-period the holes along the waveguide axis [Yamada 2001];
- (c) increasing the hole-size and changing the hole-shape into elliptical along the waveguide axis [Sigalas 2003];
- (d) increasing the hole-size for the two rows adjacent to the $W1$ waveguide [Adibi 2000];
- (e) changing the corrugation symmetry by shifting the PhC boundaries with half-period [Benisty 1996];
- (f) inserting air trenches on each side of a $W1$ waveguide [Lau 2002];
- (g) reducing the refractive index of a $W1$ waveguide core (e.g. by etching pores into it) [Søndergaard 2002b];
- (h) using hexagonal holes, in combination with triangular air inclusions [Bostan 2004a].

Several ways of tuning the band diagram have been proposed in order to obtain single-mode low-loss propagation (Figure 4.8).

Shifting PhC blocks destroys the periodicity of the original lattice and makes it more difficult to introduce bends and junctions. From this point of view approaches (a) and (e) are not convenient. Increasing the hole-size (c) can lead to higher losses if the mode profile has a significant overlap with the holes. In approach (d) the band diagram is complicated by the fact that the properties of three rows of holes are changed; some acceptor-type modes are usually pulled up into the gap from the lower gap edge and can spoil the single-mode condition.

Only approaches (e) and (f), have solved the DBR problem in line defect waveguides. Lau and Fan [Lau 2002] applied structural tuning without lattice distortion. The structure is a normal ridge waveguide embedded in a photonic crystal with trenches that cut through the adjacent rows of holes. The trench width is a design parameter, which helps eliminating the surface states from the region of interest. The DBR effect is eliminated in this case, but this structure would have in practice a low mechanical stability and rigidity without a solid bottom cladding.

Adibi and co-workers [Adibi 2001a] have shown that the most important role in the behavior of a line defect waveguide is played by the adjacent rows of PhC boundaries that modulate the waveguide width. In the case of circular holes, the waveguide edges will always be curved, whereas in the case of hexagonal holes, the edges can be straight. Hexagonal holes, in combination with triangular air inclusions (approach (h)) can make linear defect waveguides that resemble ridge waveguides, without using lattice distortion. In the next section we will concentrate on this type of PhC-based line defect waveguide.

4.6. Waveguides in hexagon-type photonic crystals

4.6.1 Two-dimensional calculations based on effective index approximation

In the following we consider line defect waveguides along Γ -K direction. Therefore the band diagram of the original perfect periodic lattice has to be projected along Γ -K. Qualitative design rules can be obtained from a 2D calculation [Søndergaard 2002a] combined with the light-line of a cladding that restricts the ω - k range available for guided modes in the actual 3D case. Here we are using the effective index approximation introduced previously for PCS's in section 3.2.6. The vertical index distribution is replaced by a homogeneous medium with an index equal to the effective index of the fundamental guided mode for a given polarization. This approximation is valid when the slab thickness is below the cutoff value for single-mode waveguiding. The effective indices of H and E guided modes considered here are the same as those in section 3.2.6: $n_{eff}^H = 2.924$ and $n_{eff}^E = 2.24$.

In order to calculate the projected band diagrams of line defect waveguides, we used a supercell (see e.g. Figure 4.9) containing 8 rows of holes and the line defect in the middle with the length of a (the periodicity along Γ -K).

In actual experiments one is using finite-sized samples. Their behavior cannot be readily expressed in terms of Bloch modes and an important role is played by evanescent modes and reflections from the boundaries. Therefore, in order to crosscheck with the results obtained using the supercell approach, we performed a 2D finite-element (FEM) simulation using FEMLAB. FEM has the advantage of providing the stationary field profiles, so that one can quantify the field energy localization and power flow directionality. Because it is a frequency-domain method, FEM can deal with dispersion easily.

The computational domain is finite, with transparent ('low reflecting') boundary conditions. At the waveguide input a constant amplitude field is applied. Power outflow is monitored at the other end of the waveguide. Transmittance is given by the ratio between the power outflow at the output boundary and power inflow at the input boundary (it is influenced by the coupling of the input field with the waveguide modes). Frequency is scanned in the gap range $u=a/\lambda=0.23\dots0.42$ with 200 steps.

In principle, the hexagon's rotation angle θ can be used for designing a waveguide that does not have a central axis of symmetry. But, when the symmetry is preserved, the modes can be classified as 'even' or 'odd' with respect to the central axis, and these classes have theoretically zero cross-coupling. Then, the fundamental mode of an input ridge waveguide can preferentially excite the lowest order mode of the line defect waveguide.

Taking into account these considerations, we focus on waveguides with a central symmetry axis, namely two waveguide types:

- **Type A:** lattice orientation $\theta=0^\circ$; waveguide width is reduced to $1.23a$ and air inclusions are equilateral triangles with side $0.9a$ (see Figure 4.9 left panel)
- **Type B:** lattice orientation $\theta=30^\circ$; lattice is undistorted and air inclusions are isosceles triangles with 120° apex angle and equal sides $1.1a$ (see Figure 4.11 left panel).

Reducing the waveguide width is necessary for type A waveguides in order to tune the band diagram significantly (otherwise, the projected band diagram would look very similar to that of a W1 waveguide).

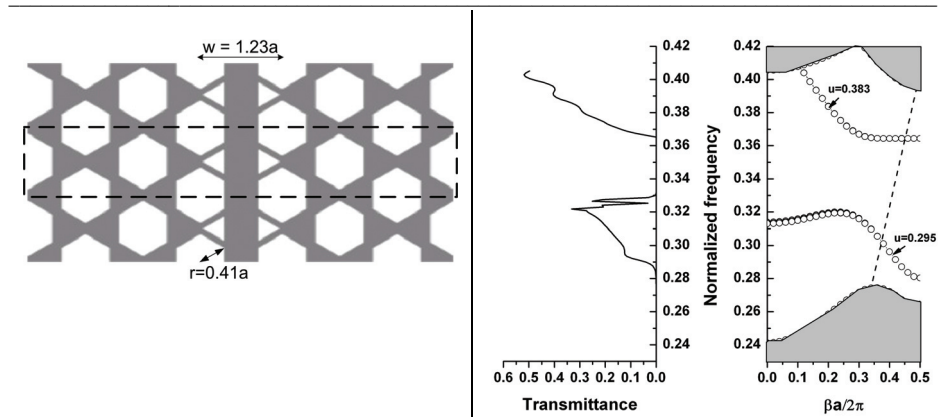


Figure 4.9 Type A line defect waveguide: left – domain geometry and supercell (dashed line); right – correspondence between dispersion curves of guided modes and spectral transmittance (the light line is the dashed line)

For a type A waveguide there is a single-mode branch below the light line for $u=0.28\dots0.3$, which has a high group velocity ($0.2c$). There is also a large mode gap for $u=0.32\dots0.363$, and that coincides with a drastic drop in transmittance in this range (see Figure 4.9 right panel). This mode gap might be used for filtering, but it is a disadvantage in applications that require broadband transmission.

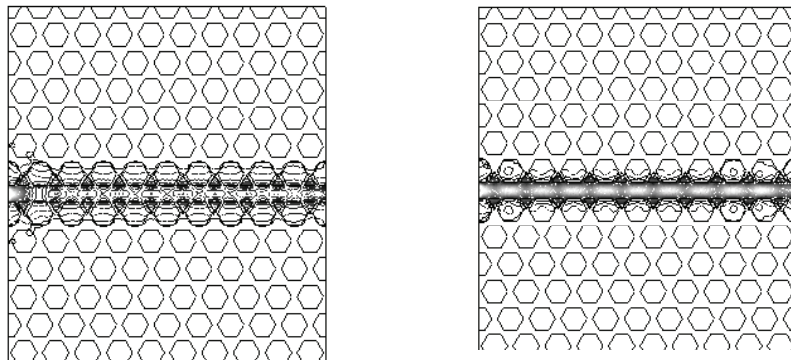


Figure 4.10 Contour plots of the Poynting vector amplitude for two H modes in type A waveguides at normalized frequencies indicated in Figure 4.9 right panel: $u=0.295$ (left) and $u=0.383$ (right)

Figure 4.10 shows Poynting vector amplitude plots of two modes. Both modes are localized in the 'defect', but the mode at $u=0.295$ has a greater expansion into the neighboring holes, and this can increase its losses in 3D. Although situated above the light line, the mode at $u=0.383$ has a better localization in the high-index 'defect' and this might imply low propagation losses in practice.

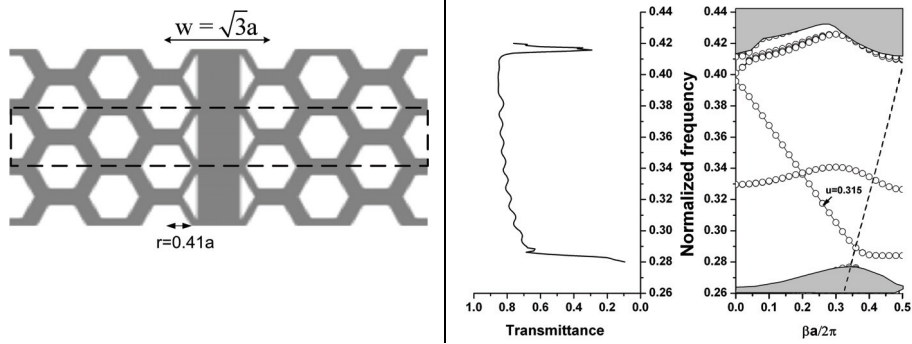


Figure 4.11 Type B line defect waveguide: left – domain geometry and supercell (dashed line); right – correspondence between dispersion curves of guided modes and spectral transmittance (the light line is the dashed line)

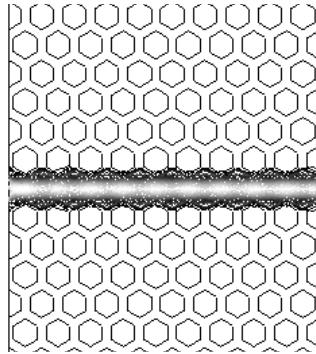


Figure 4.12 Contour plot of the Poynting vector amplitude for a H mode in type B waveguide at normalized frequency $u=0.315$ (indicated in Figure 4.11)

For the type B waveguide we focus our attention on the lower guided mode (even) in Figure 4.11-right panel. This is in fact the fold-back of the index-guided mode at the edge of the line defect Brillouin zone. This mode undergoes an anticrossing with another even mode from the lower edge of the gap (around $\beta a/2\pi=0.36$). As consequence, the spectral region below the light line of the even mode is very limited ($u=0.284\dots0.29$) and the group velocity is small. However, the even mode covers a broad range of frequencies above the light line. Even for modes situated above the light line the propagation losses might be low in practice. For $u=0.29\dots0.326$ there is a single mode region, covered by the even mode that has a high group velocity ($v_g=0.31c$).

The transmittance through the type B waveguide (Figure 4.11-right panel) has a broad band, with a small ripple. The contour plot of the Poynting vector for an H mode at normalized frequency $u=0.315$ is shown in Figure 4.12.

4.6.2 Three-dimensional FDTD calculations of spectral transmittance

High-index contrast systems require full 3D calculations of the band structure and further optimization of structural parameters. Therefore, we have analyzed by 3D FDTD a type B waveguide. The lattice constant is $a=0.315\lambda_0$, where $\lambda_0=1.55\mu\text{m}$ is the central wavelength of the spectrum of interest. The normalized frequency $u=0.315$ is below the bulk states for the quasi E-like modes and in the gap of quasi H-like modes (see Figure 3.13). The waveguide length is $14a$ and discretization is 16 points/ a . ‘Perfectly matched layers’ (PMLs) that approximate well the transparent boundary conditions surround the computational domain. The input wave is a Gaussian pulse with central wavelength λ_0 and width $0.5\lambda_0$. The source is located at the center point of the S_i line waveguide and has a Gaussian spatial distribution resembling the fundamental mode of the ridge. The input power is normalized to unity. Power flow is monitored at the waveguide output (integrated over a detector with an area equal to the waveguide core). Through a ‘fast Fourier transform’ of the temporal response, the spectral transmittance of the waveguide (shown in Figure 4.13), normalized with respect to the input spectrum, is obtained at the end of a single run. We have considered both H-like and E-like excitations, to account for the possible mode mixing. Both polarizations show quite large bandwidth of high transmittance. However, it is still unclear which factor, mode mismatch or out-of-plane losses, has more weight in these results. Mode mismatch occurs at the source location. If the spatial profile of the source is similar to that of an eigenmode of the line defect waveguide, the mode mismatch can be minimized. In order to quantify the losses for λ_0 , we performed another series of calculations using a continuous wave excitation. After reaching the steady state, the optical power was evaluated at several cross-sections of the waveguide, allowing us to make a distinction between coupling loss and propagation loss.

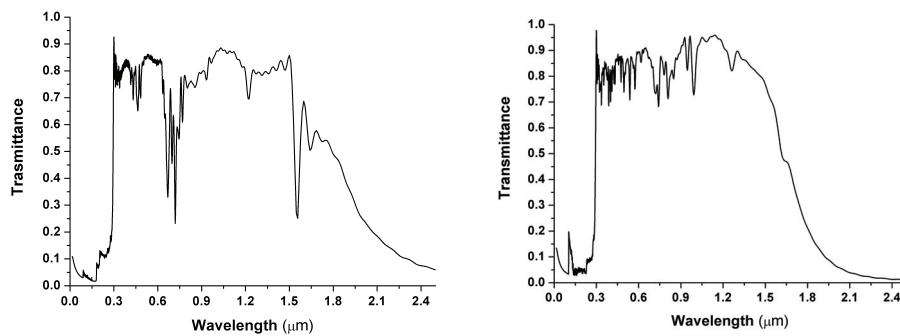


Figure 4.13 Transmittance* of a type B waveguide calculated by 3D FDTD; left: H-like excitation (TE); right: E-like excitation

* This figure is rather theoretical since silicon is not transparent for wavelengths lower than 1100 nm

It turned out that, for the present set of parameters, the losses at 1550 nm are about 15 dB/mm for H-like excitation and 200 dB/mm for E-like excitation. The high losses in the E-like excitation case are due to coupling to the bulk states for this polarization. At the same time, the coupling between the H-like excitation and E-like bulk modes is quite low. The results presented here may not provide the lowest losses achievable in these structures. Further optimization would have required extensive calculations and these were not pursued because of time constraints.

4.7. Bends and Y-junctions

Line defect waveguides can be combined to form bends and branches. Connecting two or three line defect waveguides at an angle (e.g. 60° in a triangular lattice) makes a bend or a Y-junction, respectively. The main role of the PhC is to prohibit the in-plane bend losses, and allow curvature radii as small as the wavelength. The translational symmetry of straight waveguide is broken when introducing a bend or a Y-junction; then, even and odd modes can couple to each other. The following phenomena that occur at a normal bend are detrimental to the transmission: (a) strong back-reflections; (b) increased out-of-plane losses; (c) relatively poor matching between the guided modes of the straight sections (because the bend is usually multimode). On the other hand, the transmission along a bend can be higher than in a line defect waveguide, in the ministop bands of the latter.

Several designs of bends and Y-junctions have been proposed, targeting minimization of back-reflections and improvement of mode-matching: (1) place small holes in the center of the constituent W1 waveguides [Chutinan 2002] or at the connection point of a Y-junction [Boscolo 2002]; (2) displace holes from the inner to the outer corner of the bend [Benisty 2002]; (3) introduce an intermediate short section at half of the bend angle [Benisty 2002], [Mekis 1996]; (4) reduce the corner angle in a polycrystalline PhC made by dislocating lattice blocks [Sharkawy 2003]; (5) deform the lattice in and around the bend [Ntakakis 2004]; (6) modify the lattice topology by connecting several holes at the corner [Jensen 2004].

Resonant elements incorporated in the waveguide (e.g. displaced holes that act as resonators) can give an increased transmission for certain wavelengths but, most of the time, do not provide a large bandwidth. Lattice deformation can be effective, but then the concept of PhC is somewhat obscured. In a naïve ray picture, an intermediate short section at half of the bend angle acts as a corner mirror that directs an incident ray from the input to the output branch of a bend. This intuitive argument proved to be effective [Benisty 2002], [Mekis 1996], therefore we applied it in our designs [Bostan 2004b], aiming also at keeping the resemblance with ridge waveguides. When using $\theta=30^\circ$, the inner edge of a short intermediate waveguide section at 30° appears naturally, without the need to change any hole. Some modifications of the PhC structure are needed to obtain the proper outer edge of the intermediate waveguide section. For a bend, half of the hexagonal corner hole is filled and

the hole-shape is changed into a trapezium (Figure 4.14-right panel). For a Y-junction, an extra equilateral triangle is introduced at the connection point (Figure 4.15-right panel). In this way, one can achieve good mode matching among input and output branches and intermediate sections.

The transmittance through the line defect waveguide is considered as a reference for assessing the efficiency of bends and Y-junctions. We define the relative transmittance (T_r) as the ratio between the transmittance through the bend or Y-junction and the transmittance through the straight line-defect waveguide.

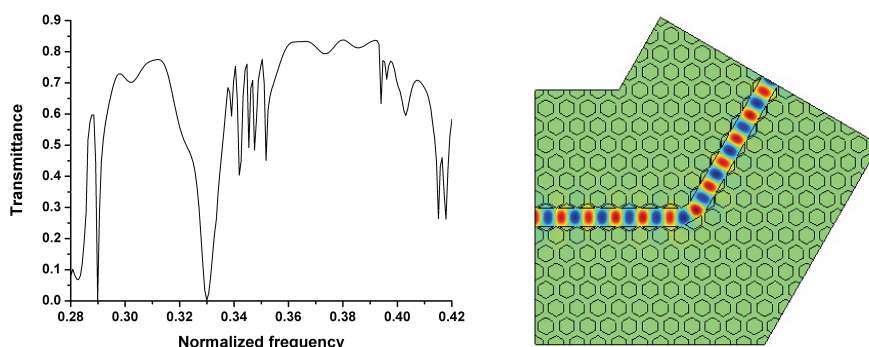


Figure 4.14 Left: spectral transmittance through a bend; Right: the H field distribution at normalized frequency $u=0.315$

We consider a bend and a Y-junction with almost the same length as the line-defect waveguide (Figure 4.14, Figure 4.15-right panels). For the bend in Figure 4.14-right panel, $T_r > 89\%$ in the range $u=0.302\dots0.316$ (Figure 4.14-left panel). For the Y-junction in Figure 4.15-right panel, $T_r > 63\%$ in the range $u=0.302\dots0.32$ (Figure 4.15-left panel). Both the bend and the Y-junction are characterized by resonances of the corner cavities ($u=0.33$ for the bend, $u=0.373$ for the Y-junction). Then light is ‘trapped’ at the corner instead of being transmitted through and the transmittance is close to zero. The separation in even and odd modes is not possible anymore in a bend or Y-junction, and this leads to mode mixing. The mixing between two modes can be seen in the transmittance, in the form of rapidly oscillating spikes in the range $u=0.338\dots0.352$ (Figure 4.14, Figure 4.15-left panels).

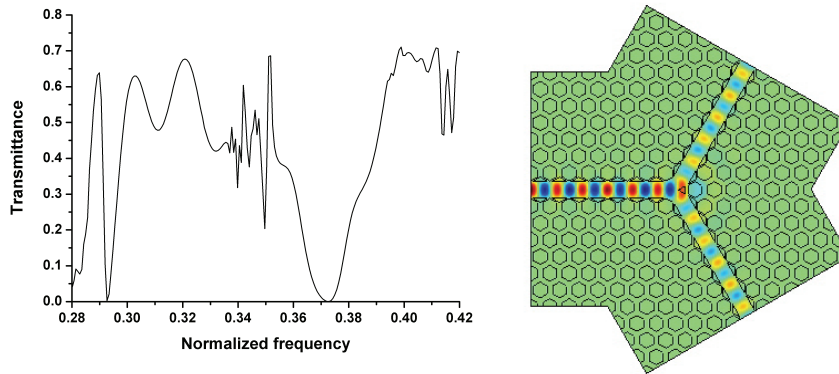


Figure 4.15 Left: total spectral transmittance through a Y-junction (sum of the two branches); Right: the H field distribution at normalized frequency $u=0.315$

4.8. Conclusions and discussion

Telecom applications of line defect waveguides in PhC's are considered in this thesis. The waveguide should act as a 'light pipe' for directional transmission of signals. Engineering the line defects proved to be necessary in order to achieve the desired characteristics: broad bandwidth, single-mode, low-losses. These are traits of usual ridge waveguides. Therefore, we opted for a novel hybrid design (hexagonal holes plus triangular inclusions) in which the PhC waveguide resembles closely a ridge waveguide. The size and positions of these inclusions modify the effective index of the waveguide independently of the lattice constant (in some cases without lattice distortion) and also minimize the effect of boundary corrugations. The transmission window used lies between the projected bands for E-like and H-like modes where losses on the order of 15 dB/mm for H-like excitation are obtained.

The waveguides can be combined to form efficient bends and Y-junctions. The bends and Y-junctions include intermediate short waveguide sections at half the bend angle playing the role of corner 'mirrors'. For hexagons with $\theta=30^\circ$ rotation angle, the inner edge of these waveguide sections is straight, and this opens the possibility to make them resemble ridge waveguides, too. In this way, one can achieve good mode matching among input and output branches and intermediate sections.

PhC's may be a good way for obtaining small high-Q resonators or sensing elements, which should be coupled to the outside world through waveguides. For combining several of these basic devices, possibly in MZI-configurations, bends and Y-junctions are needed. In principle, these could be made almost as small using conventional high-index waveguides. An important reason for implementing them with PhC waveguides is the problem of matching conventional waveguides to PhC waveguides (probably a lot of those transitions result in larger overall loss and larger size than implementing the entire circuit in PhC). In this case the coupling efficiency with in/out ridge

waveguides has a more prominent role than radiation losses. One has also to consider the wavelength dependency of the transmission, due to DBR and Fabry-Perot effects (these depend on the length of line defect arms).

It seems very hard to obtain polarization-independent functioning in these devices.

To conclude, we should mention that the design of a PhC bend is a difficult task requiring a lot of computational effort. When comparing the end result with the performance of a 'photonic wire', one should take into account not only the bending losses, but also the transmission bandwidth.

For high-contrast materials, the bending loss of conventional waveguides is very low down to radii of only a few microns. Therefore, for the purpose of pure signal transport, a photonic wire will always win. PhC waveguides can probably only be motivated by their combination with other functions (e.g. resonators, nonlinear optics, sensor structures).

Chapter 5 Fabrication technologies for SOI photonic crystal components

5.1. Overview of technologies

By introducing ‘defects’ in a PCS in a controlled manner, one is able to implement passive and active building blocks (e.g. filters [Villeneuve 1996], lasers [Noda 2001]). These can then be combined to form large-scale complex architectures. The fabrication of such structures requires lithographic technology with accuracy at the 10 nm level. For mass production, the current state of deep UV lithography, as used in microelectronics seems to be a promising option for PCS with circular holes [Bogaerts 2002b]. Since this technology, using large (300 mm), wafers involves high mask costs and long turn-around times, it is less suitable for research and development of the basic functional photonic crystal structures. For characterizing these individual components only a relatively small PCS area (100-1000 μm^2) is needed which must be precisely aligned with respect to in/out coupling structures. Also, the fabrication of novel PCS structures using non-circular holes [Bostan 2002a] requires a resolution that cannot yet be provided by current optical lithography methods.

Several lithography techniques for photonic crystal devices have been proposed. Deep UV laser lithography [Bogaerts 2002b] is parallel, fast and expensive (requires steppers). However, it cannot reproduce sharp corners (because of optical diffraction) and proximity effects need to be compensated at the mask design level. Laser interference lithography (LIL) [Vogelaar 2001] is fast, cheap and suitable for large area PCS. On the downside, it is difficult to introduce defects precisely aligned with other integrated optical components (e.g. ridge waveguides used for light in/out coupling). E-beam lithography (EBL) [Krauss 1994], [Xu 2001], is the most popular method for fabricating PCS. It is very precise (typical resolution 5 nm) but it is serial, hence slow, and needs proximity correction. For large design areas, stitching errors may become noticeable. Usually it is necessary to transfer the pattern from resist to another material, more resistant to reactive ion etching (RIE). The first realisation of a 2D photonic crystal structure in GaAs/AlGaAs for optical frequencies has been reported by Krauss and co-workers [Krauss 1994]. They fabricated patterns with a maximum void-filling ratio of 65% (wall thickness of ~30nm and period of 160nm). Focused ion beam (FIB) has been applied for bulk micromachining of macroporous silicon in order to fabricate 3D Yablonovite-like photonic crystals [Chelnokov 2000]. Another recent application of FIB has been fabrication of quasi-1D photonic crystals by etching 1D gratings into freestanding multilayer membranes [Wang 2003]. FIB has a resolution close to E-beam, and does not need proximity correction if

used on conducting surfaces. Moreover, it provides direct transfer of the pattern into an etch resistant mask (metal) or even is able to perform high aspect-ratio local etching without any additional process and can be integrated with conventional optical lithography.

After the lithography step, one has to transfer the pattern into the device layer. This can be done through a process of anisotropic etching. Photonic crystal applications impose stringent requirements: the etching profile should have minimal surface roughness and vertical sidewalls. Moreover, the etching depth should be controlled accurately. Several etching techniques have been developed. Venkataraman et al. [Venkataraman 2003] have used deep reactive etching (DRIE) involving alternating sidewall polymer passivation and silicon etching. High aspect ratio (up to 8:1) structures using a photoresist mask have been realized. Tuning the process parameters can minimize the size of resulting sidewall ripples. Chemically assisted ion beam etching (CAIBE) is a highly directional etching technique [Avary 2002] that can be used to produce high quality structures. Although it is quite an old technique, standard reactive ion etching (RIE) can be successfully applied for obtaining PCS structures with high anisotropy and low sidewall roughness. The process tuning can be done with the help of diagrams pertaining to the “black silicon method” [Jansen 1995].

In this chapter we present fabrication results obtained using LIL, RIE and FIB.

5.2. Laser interference lithography (LIL)

5.2.1 Principle of LIL, design parameters and implementation

The basic idea of LIL is to create an interference pattern in space between at least two coherent laser beams. This interference pattern is transferred into a photosensitive material changing locally, through the absorbed dose, its chemical properties; for example, regions that have absorbed a dose above a threshold value, become soluble in a developer solution (positive photoresist). In this way, one can create a material with spatially periodic topography.

LIL is preferred in fabrication of periodic structures for the following reasons:

- it can be scaled to accommodate large exposure fields – diffraction gratings with areas as large as 40x40 cm² can be produced by LIL;
- it eliminates concerns about discontinuous phase errors (stitching errors);
- the depth of field is essentially unlimited on the scale of planar devices (because the coherence length of the laser is of the order of meters); this makes LIL well-suited for applications where substrate flatness and topography are critical issues
- the exposure times are orders of magnitude shorter than EBL and FIB;

- it is simple, flexible and low cost; no mask stepper is needed, only simple and inexpensive optics; the LIL setup can be easily tuned for providing a large range of grating periods;

It is important to keep in mind that the advantages of LIL are gained at the expense of pattern complexity, which is limited to periodic structures with relatively simple shapes. This means that it is difficult to introduce e.g. line defect waveguides and structures for coupling light into or out of such waveguides. However, by combining LIL with focused ion beam processing, it is possible to locally modify the LIL pattern so that more complex structures can be fabricated [Vogelaar 2001].

The most straightforward implementation of LIL consists in a 2-beam interferometer in which two coherent wave fronts are combined to form a sinusoidal interference pattern in space. By exposing a layer of resist to this pattern, a simple one-dimensional grating can be generated. We used a simple yet stable Lloyd's mirror set-up where an approximately plane wave reaches a photosensitive layer (photoresist) on a substrate both directly and via a mirror which is oriented perpendicular to the substrate (Figure 5.1).

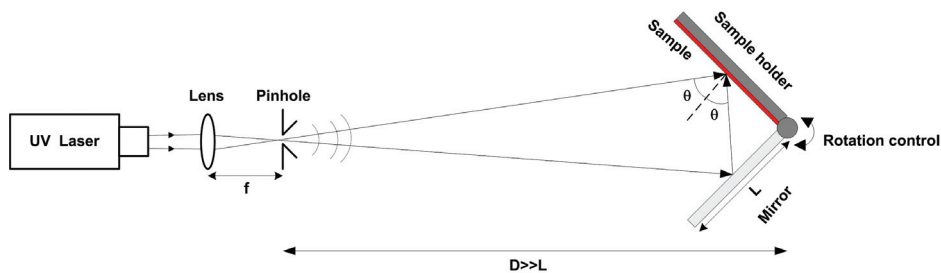


Figure 5.1 Lloyd's mirror interferometer set-up; the variable pinhole is placed in the focus of the lens; the distance between the pinhole and the sample holder (D) is much larger than the mirror size (L), to ensure good beam uniformity over the sample surface

To produce a (quasi) plane wave, linearly polarized light of a UV laser is spatially filtered and expanded by focusing it onto a variable pinhole that selects the central part of the beam. The distance between the pinhole and the sample holder is much larger than the mirror size, in order to ensure good beam uniformity over the sample surface. The laser beam is aimed at the center of the sample holder so that one half illuminates the sample and the other half the mirror. The beam reflected by the mirror interferes on the substrate surface with the beam directly incident on the substrate, forming a line interference pattern. Ideally, the mirror should give 100% reflection, so that both beams have equal intensity.

The angle of incidence θ , and thus the periodicity of the interference pattern, is easily adjusted by rotating the substrate+mirror assembly as a whole with respect to the exposure beam. During this project two LIL-setups have been used, each having a different UV laser (different wavelengths) and a different lens/pinhole combination. The choice of lens/pinhole combination depends on the laser wavelength through the parameters of a Gaussian beam waist in

focus and the depth of focus. A schematic overview of the parameters of the two LIL setups is presented in Table 5.1[Tijssen 2003].

By overlaying multiple exposures or by combining more than two beams, more complex two-dimensional (2D) structures can be patterned including square and triangular arrays of dots or holes.

Table 5.1 Schematic overview of the parameters of the two LIL setups

	LIL1	LIL2
<i>Laser specifications</i>		
Wavelength (nm)	364.8 (I-line)	266 (DUV)
Stable after power on	> 2 h	> 0.5 h
Power fluctuations (specified)	< 0.5 %	< 2 %
Power fluctuations (practice)	> 5 %	< 2 %
<i>Lens/Pinhole specifications</i>		
Focal length (mm)	15	11.53
Pinhole thickness (μm)	50	15.24
Pinhole diameter (μm)	10 ±1	10 ±1

Here we consider a LIL process involving the overlap of two exposures oriented at 60° with respect to each other (see Figure 5.2). Our aim is to use the photoresist pattern as a template for fabricating a 2D photonic crystal slab with a triangular lattice of cylindrical holes in a silicon PCS.

For the second exposure the angle of incidence θ remains the same but the substrate is rotated about the surface normal over an angle $\alpha=60^\circ$. Both linear gratings have the same periodicity:

$$d = \frac{\lambda_0}{2 \sin \theta} \quad (3.12)$$

where λ_0 is the free-space wavelength of the exposure radiation. It can be seen that the smallest theoretical period ($\lambda_0/2$) is achieved for grazing incidence; for example, the deep UV wavelength $\lambda_0 = 266$ nm gives a theoretical lower limit $d = 133$ nm; however, this is not a practical case, since in that case the incident irradiance will be zero. The lattice constant of the triangular lattice will be:

$$a = \frac{d}{\sin 60^\circ} \quad (3.13)$$

From the point of view of PCS applications, there are two important aspects: (1) the periodicity of the lattice should be perfect, and (2) the ‘filling factor’ should be uniform over a large area.

The first requirement is easily satisfied, being an intrinsic property of LIL. The second one is a challenge, because it is related to the geometry of the photoresist template obtained after the development process. It requires fine-tuning of the photolithographic parameters (e.g. irradiance, exposure time).

In order to get a starting point in the design of the LIL process we performed calculations of the electromagnetic dose recorded in the photoresist layer [Bostan 2002c], taking into account the geometrical and optical properties of the materials involved. A detailed discussion, including derivations is presented in Appendix D, here we only summarize the main formulas. Photoresist is an absorbing material with a refractive index $n_f \cong 1.7$ and an extinction coefficient $k_f \cong 0.02$. Common photoresist materials show ‘bleaching’, i.e. saturation of absorption as electromagnetic radiation is absorbed (k_f decreases during the exposure process, typically by one order of magnitude).

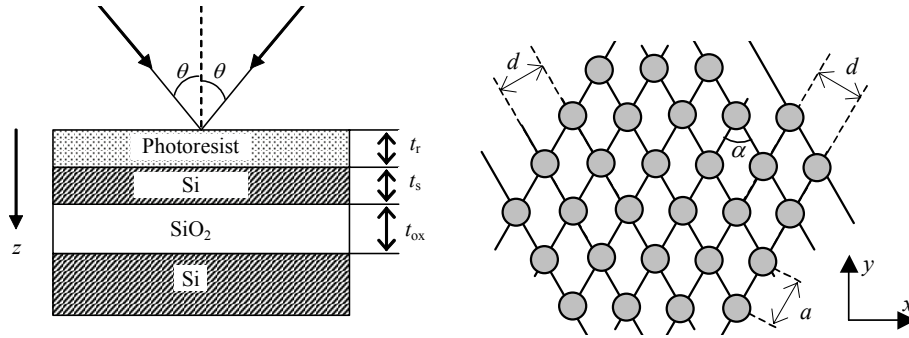


Figure 5.2 *Lithography scheme. Left: cross-section of a silicon wafer with a high-refractive index slab on a buffer layer, with photoresist on top. Right: top view of the 2D periodic structure resulting from superimposing two LIL exposures.*

The interference pattern in the photoresist layer is more complicated than suggested by equation (3.12). There is also a standing wave pattern perpendicular to the substrate plane, caused by multiple reflections at the interfaces between layers. The photoresist layer can be regarded as an asymmetric Fabry-Perot etalon, bounded by air at one side and by the multilayer stack at the other.

The recorded dose in the photoresist can be calculated from the **irradiance distribution** $I(x, y, z)$, given as:

$$I(x, y, z) = I_0 \cos \theta f_1(x, y) f_2(z) \quad [\text{W m}^{-2}] \quad (3.14)$$

where I_0 is the irradiance of the exposure beam in air for normal incidence, θ the angle of incidence, f_1 and f_2 are dimensionless periodic distribution functions, with $f_1(x, y)$ the periodic effective in-plane distribution due to the cumulative effect (sum) of the two exposures, and $f_2(z)$ the vertical distribution due to interfering reflections. Taking into account that $k_f \ll n_f$, we can approximate the spatial period Λ_z of $f_2(z)$ as:

$$\Lambda_z = \frac{\lambda_0}{2n_f \cos \theta_f} \quad (3.15)$$

where θ_f is the refraction angle at the air-photoresist interface.

The **absorbed energy density** in photoresist can be calculated by considering the conservation of energy using Poynting's theorem [Flagello 1997], leading to:

$$Q(x, y, z) = 2k_0 n_f k_f I(x, y, z) \quad [\text{W m}^{-3}] \quad (3.16)$$

where $k_0 = 2\pi/\lambda_0$.

Finally, the **recorded dose density** is obtained by integrating the absorbed energy Q in time:

$$D(x, y, z) = 2k_0 n_f \int_0^{t_{ex}} I(x, y, z, t) k_f(t) dt \quad [\text{J m}^{-3}] \quad (3.17)$$

where t_{ex} is the exposure time. The irradiance distribution $I(x, y, z, t)$ is time-dependent due to bleaching, which affects the extinction coefficient k_f , while the refractive index n_f is unchanged.

The exposure process was simulated with a computer program based on a mathematical model and taking as inputs: a) the parameters of the UV laser exposure; b) the geometry of the 2D periodic lattice; c) the thicknesses and optical properties of the materials involved. The output of the program is the 3D spatial distribution of the electromagnetic dose recorded in photoresist. Calculation results of absorbed dose distributions and comparison with experimental results are shown in Figure 5.4. The recorded dose is useful for estimating the relief of photoresist remaining after development. However, this estimation can only be qualitative, a full simulation of the photolithographic process requires detailed modeling of baking and development processes. This is a very complex task and was not pursued in this thesis. Still, the modeling of exposure process alone provides useful guidelines for experiments.

5.2.2 Fabrication processes and results

There are several possibilities to create a pattern of holes in resist, given by the combinations of resist types (positive or negative) and exposure dose. With a positive resist, there are two ways to make a pattern of holes:

- (a) using a small dose so that the holes will be developed only at the superposition of intensity maxima and use subsequent etching steps to transfer the pattern into the silicon layer;
- (b) using a higher dose so that the development leaves a pattern of freestanding dots; the diameter of these dots decreases when the dose increases; the dots can be converted to holes through a lift-off process;

Process (b) has a larger process window and a higher spatial contrast than process (a) [Fernandez 1997], therefore it was considered in our experiments. The lift-off step can be avoided by using a negative or image reversal resist.

In the framework of this project, two fabrication processes using the two different LIL setups described in Table 5.1 have been studied:

1. using positive resist and setup LIL1 , combined with lift-off (see Figure 5.3) [van Dorssen 2001];
2. using image reversal resist and setup LIL2, without lift-off [Tijssen 2003]

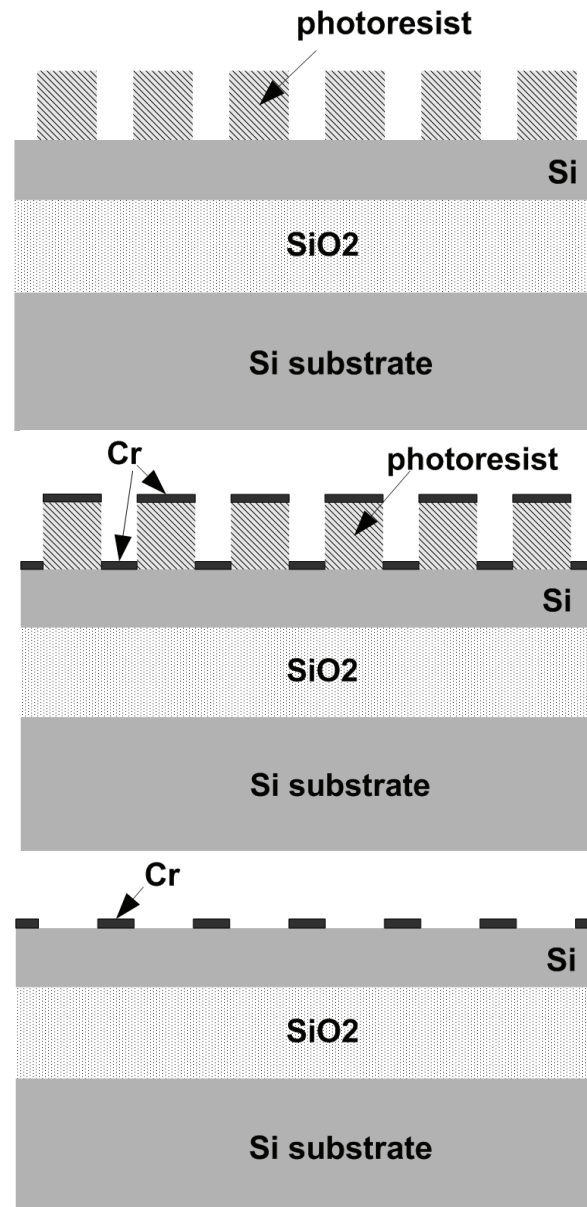


Figure 5.3 Lift-off process: developed resist pattern (top); chromium deposited on top of the resist pattern (middle); resist removed, showing remaining inverted chromium pattern (bottom)

The role of the Cr layer is twofold: (a) hard mask for reactive ion etching (see section 5.3), (b) conducting working surface for modifying the LIL-generated structure using FIB processing [Vogelaar 2001].

Detailed description of fabrication recipes are presented in Appendix E.

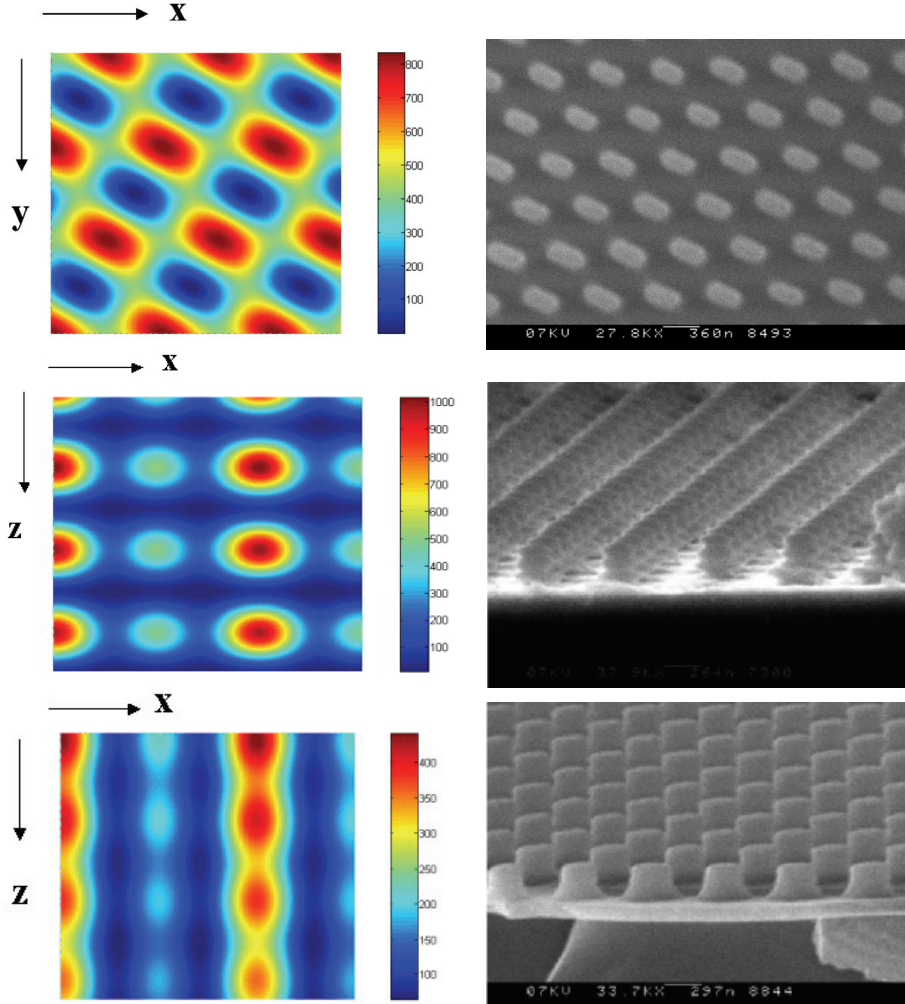


Figure 5.4 Comparison between theoretical calculations of dose distribution (left column) and experimentally observed patterns (right) in positive photoresist. Top: top view showing elliptical “dots” arising from double exposure for a triangular lattice with $a = 560$ nm lattice constant). Middle: vertical modulation after 80 s exposure, without antireflection coating (ARC). Bottom: strongly reduced vertical modulation due to using an ARC, 110 s exposure time. For all exposures the wavelength was $\lambda_0 = 364.8$ nm (I-line), the beam intensity $I_0 = 89 \mu\text{W cm}^{-2}$, and the exposure angle $\theta = 22.1^\circ$

It was found that the strong UV reflection at the silicon-resist interface caused a vertical standing wave pattern, resulting in a vertical modulation of the diameter of the resist pillars produced using process 1, see Figure 5.4,

middle right. In case of a positive photoresist an undercut resist profile results if the maximum of the standing wave occurs at the resist/substrate interface. Such a profile would be suitable for lift-off, but unfortunately is usually mechanically unstable. In order to be able to later invert the resist pattern (holes instead of pillars) using lift-off, the resist should be completely removed from the Si-interface. This leads to a tendency of over-exposure or over-development of the resist, resulting in weak low-diameter sections in the pillars, where they may easily break. Also, if there is a significant thickness non-uniformity of the resist layer, a vertical standing wave pattern can result in large variations in the developed line widths.

To minimize the effect of the standing wave pattern there are two solutions: (1) use an antireflection coating (ARC) between the photoresist and silicon layers, and (2) use a resist thickness of less than half the wavelength of the standing wave pattern ($\Lambda_z = 100\text{ nm}$, in our case), in order to obtain more robust pillars. ARC layers can be either absorptive (based on organic materials) or interferential (based on dielectrics). The interference type filter approach is an attempt to *optimize* the interference phenomenon, while the “bottom antireflection coating” (BARC) relies on absorption to reduce substrate reflection and therefore *eliminates* interference effects. Using an organic ARC can cause problems since it needs to be removed before depositing a metal layer for lift-off in the next processing step. An additional dielectric layer is also a technological complication. It was decided to use an organic ARC, but, unfortunately, the lift-off process was unsuccessful [van Dorsen 2001]; a suitable process for removing the ARC layer without affecting the photoresist pillars was not found.

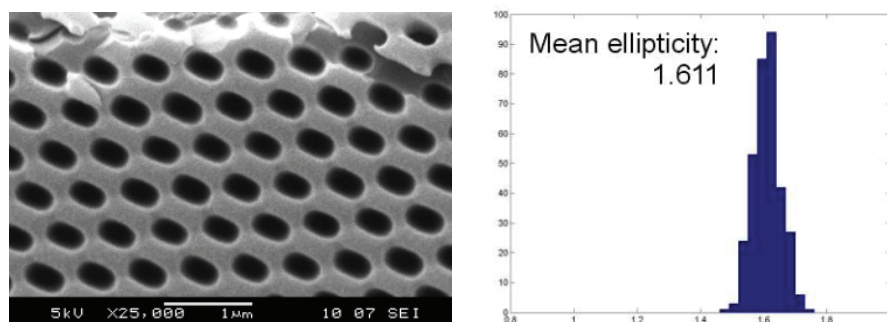


Figure 5.5 SEM picture of a sample with triangular lattice of elliptical holes in resist, fabricated using process 2 (see text for details)-left; Ellipticity distribution for this sample – right [Tijssen 2003]

Process 2 has been used by Tijssen [Tijssen 2003] who analyzed thoroughly the resulting hole patterns by means of image processing algorithms applied to SEM-pictures. The aim was to find a relationship among different process parameters (laser irradiance, exposure time, development time, etc.) and geometrical parameters (size and shape of holes) that are important for photonic crystal applications. Another important aspect investigated was the process reproducibility. After a large set of experiments using different

combinations of dose and exposure time, the best samples produced still had a non-uniform distribution of holes (see Figure 5.5). Besides, it turned out that the process was barely reproducible. This can be attributed with quite high probability to various process steps that are critical and very difficult to control (e.g. image reversal bake performed on a hotplate) and to environmental conditions (e.g. humidity, temperature).

5.2.3 Possible further developments

As can be seen from theoretical and experimental results (Figure 5.4 top and Figure 5.5 left), the shape of the recorded dose distribution due to the double exposure method will be elliptical. In principle, circular shapes can be produced by adding a third exposure after turning the substrate another 60°, but in practice this cannot be accomplished since the third exposure should be well-aligned with respect to the pattern resulting from the first two exposures. A better approach is to generate an interference pattern of three coherent beams. A very elegant way of generating these beams has been theoretically described by Berger et al. [Berger 1997] and applied experimentally for fabrication of photonic crystals [Chelnokov 1999], [Divliansky 2003]. It involves using a collimated laser beam incident on a mask containing three diffraction gratings positioned on the sides of an equilateral triangle. The first-order diffracted waves interfere in the wafer's plane (which is parallel to the plane of the mask) producing a triangular lattice.

The three-wave interference approach has several interesting features: (1) single-step exposure, (2) circular shape of the resist pattern, (3) increased spatial dose contrast which may allow direct creation of a hole pattern in positive resist without the need of lift-off, (4) lattice constant depending only on the mask grating pitch (not on wavelength or mask-substrate distance). The latter feature is a mixed blessing: it provides for a very stable process, but it also reduces experimental flexibility (for each lattice constant a different grating structure should be fabricated). For this reason, the method has not been used in the work described here.

Recently, LIL has gained ground as a viable technique for fabricating photoresist templates for 3D photonic crystals by combining 4 coherent beams [Campbell 2000]. The setups used are complex, involving precise control of polarization and sophisticated means of ensuring stability.

5.3. Reactive ion etching (RIE)

The aim of RIE is to faithfully transfer the pattern created by lithography to the underlying substrate with precise dimensional control. As a result of RIE, one would like to obtain smooth and vertical sidewalls (i.e. high anisotropy) and avoid any sample damage.

The RIE process can be briefly described as a synergetic interplay between chemical reaction(s) and ion bombardment. Chemical etching is usually isotropic, and, in order to prevent the lateral etching and achieve high

anisotropy, an inhibitor (passivating) layer is needed on the sidewalls. On the other hand, this layer has to be removed from the horizontal surface to allow the etching to proceed further. The physical bombardment with ion species removes the passivating layer from the exposed area.

RIE is a vast research topic. Therefore, no attempt was made to treat it exhaustively. The interested reader is referred to the work of Oehrlein [Oehrlein 1990]. In this section we discuss briefly the main mechanisms and we underline the main points to be considered when designing a RIE process for photonic crystal applications.

5.3.1 RIE mechanism for Si

The RIE process for Si has been studied in detail by Jansen et al [Jansen 1996] This work was the author's main source of inspiration in this subject.

A chemical etchant in gaseous form for silicon is *sulphur hexafluoride* (SF_6). In a plasma SF_6 produces F^* radicals which react spontaneously with Si forming volatile products SiF_x (there is practically no energy barrier for this reaction). Using SF_6 alone is not a good option because of the isotropic character of etching. One possibility to create a passivating layer is to add *oxygen* (O_2) which produces O^* radicals. These compete with F^* for adsorption on active sites on the Si surface and passivate it with a thin layer of *silicon oxyfluoride* (SiO_xF_y).

Adding O_2 to the gas mixture has several effects:

- The sidewalls are quite rough and positively tapered (i.e. hole-diameter is decreasing with depth), while the bottom of trenches in the Si layer are rounded;
- The etch rate decreases drastically with increasing the O_2 content (for example, an increase of O_2 concentration from 25% to 50% leads to a decrease in the Si etch rate by a factor of 10)

Therefore, to achieve the goal of vertical and smooth sidewalls, another gas has to be added to the mixture. *Trifluoromethane* (CHF_3) gives negatively tapered sidewalls and this can compensate for the effect of O_2 . Moreover, CF_x species produced by CHF_3 tend to scavenge the O^* radicals which are an ingredient of the passivating layer. As a result, the sidewall roughness can be reduced significantly. Nevertheless, the correct balance between CHF_3 and O_2 is important for achieving high anisotropy and good smoothness.

The potential developed between the plasma and the powered electrode is called DC-bias and determines the ion energy (the ion energy is proportional to the DC-bias). The DC-bias decreases when the RF power level decreases or the pressure increases. O_2 and CHF_3 give rise to high DC-bias whereas SF_6 has an opposite effect. A low DC-bias, on the order of tens of volts, prevents substrate damage and mask erosion and makes it easy to change the etched profile. A high DC-bias will give the off-normal ions enough energy to etch the sidewalls (see Figure 5.9 top left). In conclusion, a low DC-bias is needed for obtaining etching profiles with high anisotropy. This can be obtained for a $\text{SF}_6/\text{CHF}_3/\text{O}_2$ gas mixture at high pressure and medium RF power.

5.3.2 RIE mechanism for SiO₂

RIE of SiO₂ can be achieved in a CHF₃ based plasma, optionally adding small quantities of inert gases (e.g. argon, helium).

Energetic electron collisions produce reactive species such as F atoms, CF₂ radicals, and CHF₂⁺ ions. These species are absorbed at the substrate surface and react with the substrate forming products like SiF₄, CO₂, COF₂ and water [Paul 2002]. The reactions at the substrate surface are enhanced by the energetic ion bombardment that also prevents the polymerization of COF₂ on the oxide surface.

5.3.3 RIE experimental results

RIE has been performed in an Electrotech, Plasmafab 310-340 parallel-plate system with an RF generator operating at 13.56 MHz. For etching Si we applied a recipe based on SF₆/CHF₃/O₂ = 30/10/12 sccm* gas mixture and a pressure of 100 mTorr, tuned for high anisotropy and low roughness by varying the power level. Etching SiO₂ was performed in a CHF₃/O₂ = 25/5 sccm gas mixture and 10 mTorr pressure.

Chromium has been chosen as mask material for the following reasons: (1) it is etch resistant (it is not sputtered for ion energies up to 200 eV), thus preventing substrate contamination and micromasking; (2) it provides a conductive working surface for FIB etching, avoiding charging problems.

Etching tests have been performed on Si substrates, thermally oxidized Si wafers and SOI wafers. The test mask used consists of lines with 2.5 μm width.

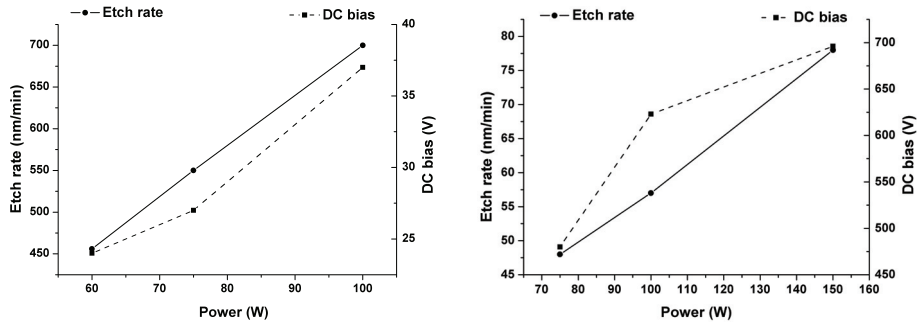


Figure 5.6 Variations of etch rate and DC bias as function of RF power for RIE etching of Si (left) and SiO₂ (right)

The etch rates and DC bias values for etching Si and SiO₂ are shown in Figure 5.6. Etching of Si is characterized by small values of DC bias, but etching of SiO₂ with this combination of gases leads to large values of DC bias which can sputter away the Cr mask. Sputtering of the Cr mask was not

* flow unit, commonly used in specifications of technological equipment, meaning ‘standard cubic centimeter’

observed for the relatively broad lines, but it became clear when etching the array of sub-micron holes of PCS (see Figure 5.7).

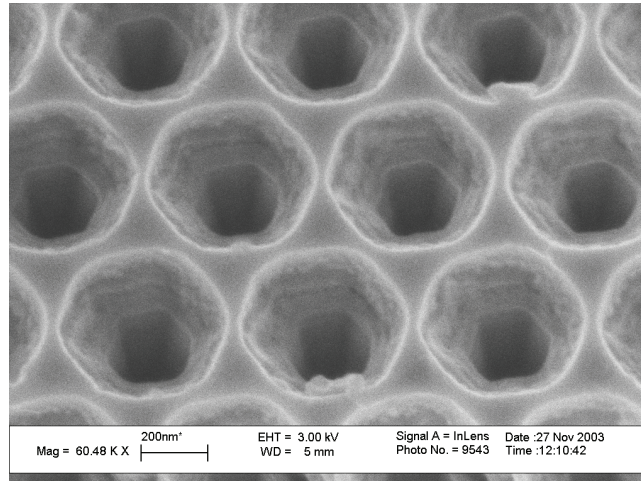


Figure 5.7 SOI-PCS detailed view after a two-step RIE process; etching SiO_2 with a combination of gases CHF_3/O_2 roughened the sidewalls of Si layer and sputtered the Cr mask at holes' edge, leading to a hole enlargement and shape distortion

The etch rate of SiO_2 is quite small and increases slowly with the RF power. This implies longer etch times, that make mask sputtering even more critical. This is exactly the opposite of our wish. A suitable solution for RIE of SiO_2 , considering the equipment available in MESA+ clean-room was not found. This prevented the fabrication of a high-quality structure with holes deeply etched into the SiO_2 layer of a SOI wafer. In fact, etching of SiO_2 is not absolutely necessary for fabricating a workable PCS structure, although at the expense of a smaller photonic bandgap and increased out-of-plane radiation.

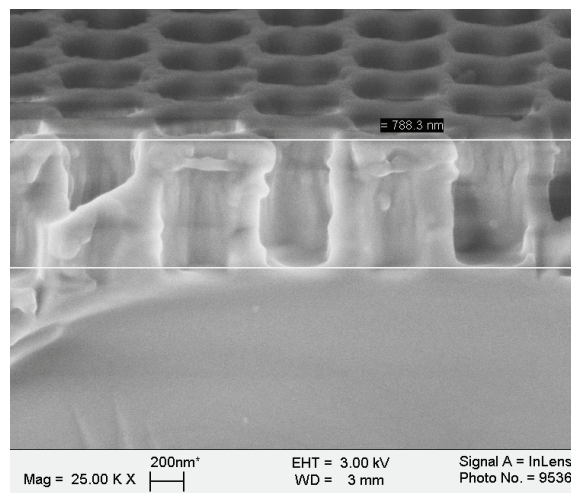


Figure 5.8 SEM picture of a cleaved cross-section showing the profile of Si/ SiO_2 layers after RIE

A cross-section picture of the sample from Figure 5.7 is shown in Figure 5.8. We have cleaved the sample and this has led to serious damaging of the small holes situated at the edge. However, the sidewall roughness is still visible in Figure 5.8. In section 5.4.4 we will show a high-performance cross-sectioning technique, based on local focused ion beam milling.

The etching profiles have been checked by scanning electron microscopy (SEM). The results for RIE of Si and SiO₂ with the recipes mentioned above, at different levels of RF power are shown in Figure 5.9 and Figure 5.10, respectively.

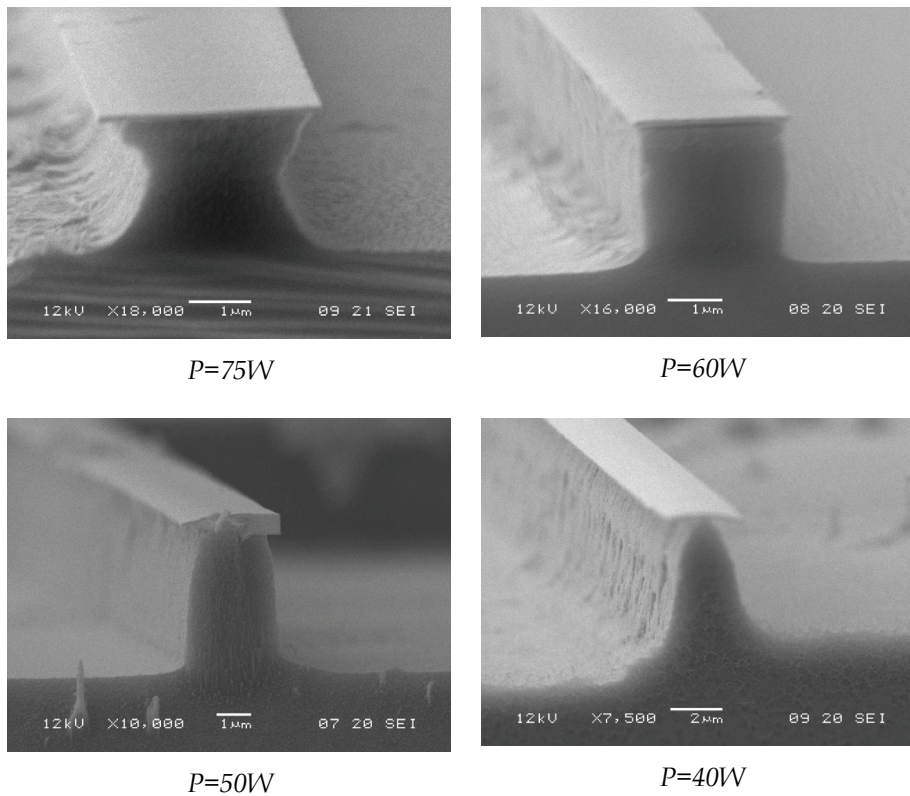


Figure 5.9 Etching profiles in Si as function of RF power: isotropic ($P=75W$); highly anisotropic ($P=60W$); small mask undercut, smooth sidewalls ($P=50W$); large mask undercut rough sidewalls ($P=40W$)

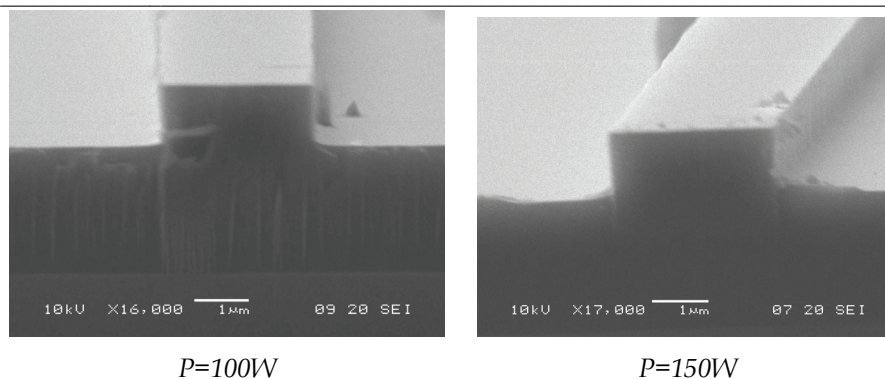


Figure 5.10 Etching profiles in SiO_2 as function of RF power; profiles are highly anisotropic with smooth sidewalls

It is clear that the etching profile in Si can be tuned as function of RF power; the optimum anisotropy and sidewall smoothness is around $P = 60 \text{ W}$. On the other hand, the etching profile in SiO_2 is independent of RF power, being mostly a physical process driven by ion bombardment.

5.4. Combining conventional lithography with focused ion beam (FIB)

5.4.1 Introduction

In this section we discuss briefly the main components and the working principle of a FIB machine and we also address the applications of FIB in nanotechnology.

The FIB machine is made of several building blocks: vacuum chamber, ion column, command and control electronics and computer workstation with user interface. A typical ion column is shown in Figure 5.11. The liquid ion metal source consists of a sharp tungsten needle that is wetted with gallium metal. The needle is heated up by passing a large current through it and Ga becomes liquid. A very intense electric field is applied at the sharp tip of the needle and this produces ionization of Ga and extraction of Ga^+ ions. The Ga^+ ions are then accelerated by a high voltage and focused by a system of electrostatic lenses down to a nanometer-sized spot. This spot is directed onto a substrate and can be precisely scanned across it.

When Ga^+ ions with high kinetic energy hit the surface of a solid sample they lose energy to the electrons of the solid as well as to its atoms. Then, several physical effects take place, the most important being:

- (a) sputtering of substrate atoms (substrate milling);
- (b) generation of charged secondary particles- ions and electrons (this effect enables imaging);

- (c) displacement of atoms in the solid (induced damage);
- (d) emission of phonons (heating).

Most of the Ga^+ ions that arrive at the sample surface enter the sample; thus ion implantation occurs. The depth of this implanted region depends on the ion energy and the angle of incidence.

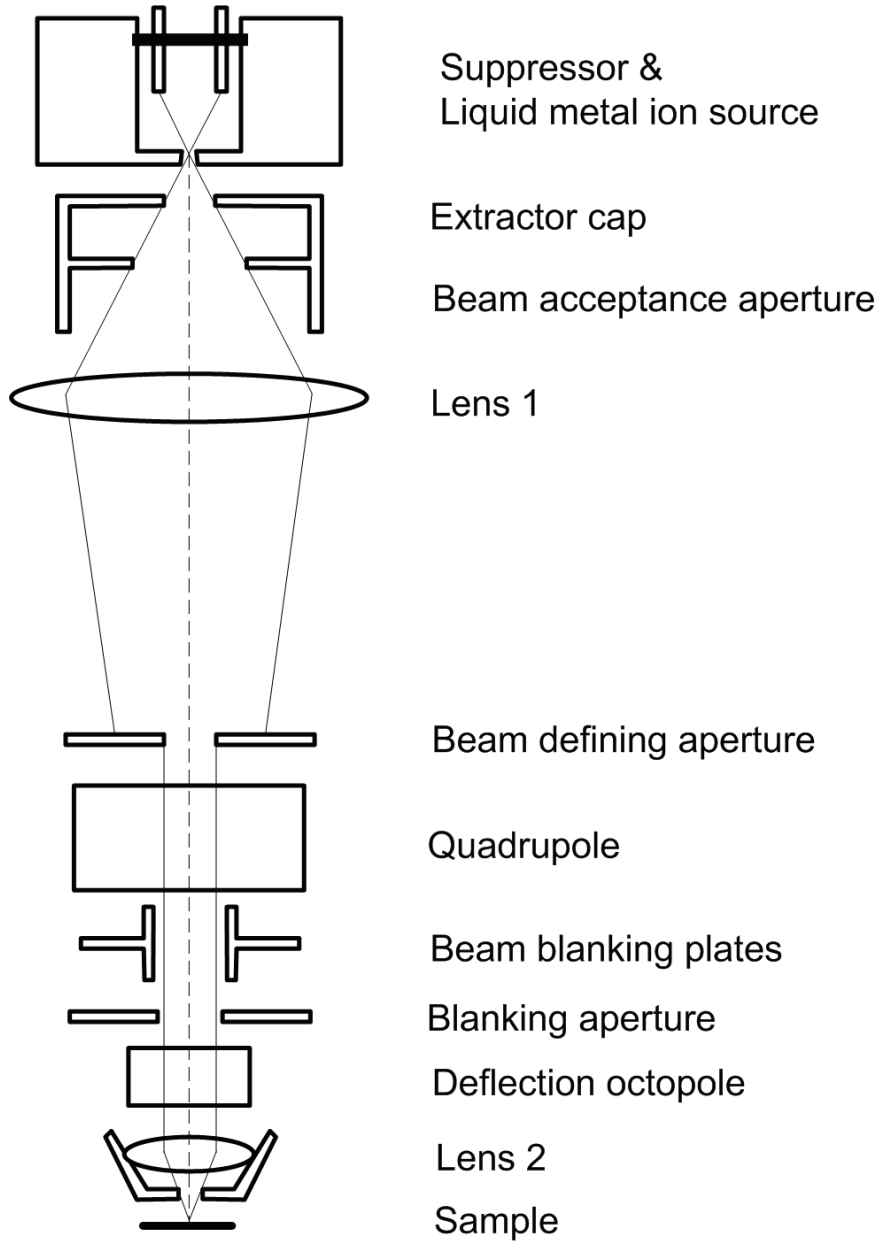


Figure 5.11 Schematic view of typical ion column [Gadgil 2004]

The ion current has a broad range of variation (typically from 1 pA to more than 10 nA). Small currents are used for fine polishing of the sample surface or imaging, while high currents are used for fast and rough milling of the sample material. A lower beam current gives a smaller beam diameter, hence a better resolution, at the expense of a longer processing time.

Secondary electrons or ions leaving the sample can be collected on a biased detector (micro-channel plate), depending on the detector bias. This allows imaging the sample surface and monitoring the milling process. In a single-beam FIB there are two main drawbacks of using the imaging mode: (a) etching takes place while imaging even when working with the minimum available current; (b) image resolution is lower than that of a good scanning electron microscope (SEM). These two problems are solved in dual-beam machines that include a separate SEM column.

The milling process is monitored through the 'end-point detection'; this is a realtime graph of the average brightness in the milling area that can tell the user what layer is currently milled in a multilayer structure.

FIB has a high depth of focus (e.g. 300 μm for 100 nm resolution) that allows the production of high-resolution patterns without refocusing or changing sample height; it also allows the patterning of curved substrates.

From the applications point of view, FIB is a well-established technique with the unique capabilities to locally sputter, ion implant, deposit metals and insulators with a feature size on the order of nanometers, without the need of a mask [Reyntjens 2001]. FIB is a valuable tool for process characterization as well. For example, FIB can be used for precise cross-sectioning of structures having sub-micron features (see Figure 5.15) with a damage that can be of only very limited extent. In this case, cleaving would be very difficult. In optoelectronics, FIB has been applied for fabrication of micro-optical components with low surface roughness [Fu 2001] and defining the end facet mirrors for conventional semiconductor lasers [Ito 1997]. Besides the traditional applications, FIB can be used for 'lithography', for planar definitions of patterns.

5.4.2 FIB milling parameters

In this section we provide a brief review of the FIB parameters related to the milling process and that can be controlled via the computer user interface. It is important to choose these parameters judiciously, in direct relationship with the required resolution for the pattern to be milled and the material the sample is made of. A schematic view of a rectangular milling area, illustrating some of the geometrical parameters is shown in Figure 5.12.

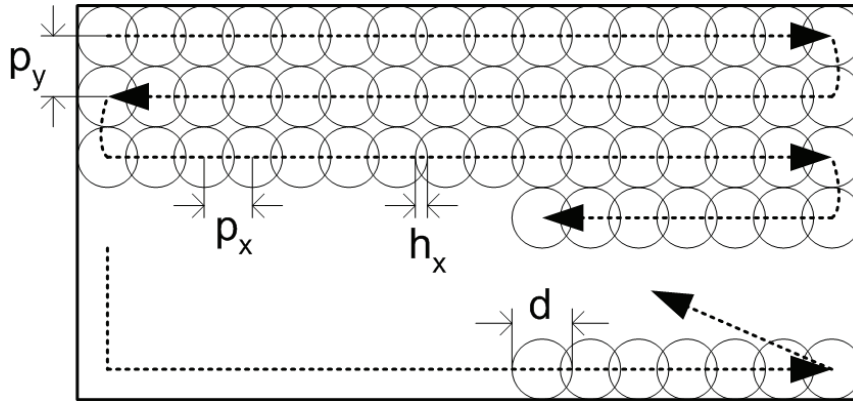


Figure 5.12 Schematic view of milling of a rectangular area in a serpentine scan; pixel sizes (p_x, p_y), beam diameter (d) and beam overlap (h_x) are indicated (see text)

- **Field of view (FOV)** = maximum area that can be scanned by the ion beam without translating the sample stage; the shape of this area is rectangular and its size depends on the magnification (see *Table 5.2*);
- **Pixel pitch (p_x, p_y)** = minimum area that can be addressed by the incident beam; the FOV is discretized in an array of typically 4096x4096 pixels (12-bit digital-to-analog converters drive the deflection octopole that controls the beam positioning); pixels are contiguous and rectangular, with dimensions:

$$p_x = \frac{FOV_x}{2^{12}}; \quad p_y = \frac{FOV_y}{2^{12}}$$

- **Dwell time (pixel time - t_p)** = the time the beam is stationary on a given pixel and mills that specific pixel; in general, the dwell time can be programmed to vary from pixel-to-pixel;
- **Pattern** = sub-domain of the FOV with arbitrary shape, which is milled by multiple loops (i.e. raster scans or frames) of the ion beam (a rectangular pattern is shown in Figure 5.12);
- **Loop time (t_l)** = time elapsed between two consecutive exposures of the same pixel to the ion beam; it depends on the size of the pattern (i.e. number of pixels in a pattern);
- **Retrace time (t_r)** = delay time before re-scanning; the ion beam is blanked off between successive scans; for a pattern made of N pixels with equal dwell times, the loop time is $t_l = Nt_p + t_r$;
- **Beam diameter (d)** = full-width at half-maximum of the incident ion beam that has a Gaussian profile; it increases with the ion current;
- **Beam overlap (h_x, h_y)** = ratio of the overlap of two adjacent pixels divided by the diameter of the ion beam; if the beam overlap is “+50%,” it means that there is an overlap equal to the beam radius between two adjacent beam locations (center to center); a “-50%” beam overlap indicates that the gap between two pixels is equal to one half of the beam diameter;

- **Stream file (.str)** = file in text format containing the coordinates and dwell times of each pixel in a pattern and the number of loops;
- **Sputtering yield (Y)** = number of atoms removed from the sample per incident ion; Y is dependent on many parameters: beam energy, substrate temperature, dwell time, target density, angle of incidence;
- **Milling rate** = volume of material removed per unit of current and unit of time; can be deduced from the sputtering yield and number of atoms per unit volume for a given material

Table 5.2 Relationship between several magnifications, FOV and pixel pitch for FEI FIB 200 machine

Magnification	Field of View ($FOV_x \times FOV_y$)	Pixel pitch ($p_x \times p_y$)
2500	86.3 μ m \times 84.2 μ m	21.07nm \times 20.55nm
3500	61.6 μ m \times 60.1 μ m	15.04nm \times 14.67nm
5000	43.1 μ m \times 42.2 μ m	10.52nm \times 10.3nm
10000	21.6 μ m \times 21.1 μ m	5.27nm \times 5.15nm

The FIB system used in our experiments is a FEI FIB 200 single beam workstation with Ga⁺ liquid metal ion source. The ion acceleration energy is 30 keV. A beam current of 70pA – which gives a beam diameter of about 12nm – has been selected. The magnification used was 5000X, which leads to a pixel size of about 10nm. This means that there was a slight overlap between adjacent pixels that is known to produce a better surface finish.

In our experiments, a dwell time of 10 μ s has been found to provide a good trade-off between high sputtering yield and minimum re-deposition. The pattern to be milled was programmed in a .str file. The .str files were generated automatically through an external application, and then loaded from the FIB control panel. The parameters of a PhC pattern containing a line defect are: (1) lattice constant; (2) number, size and type of scattering elements; (3) width of line defect. The pattern generated is positioned in the middle of the FOV, in order to ease the alignment procedure. A hardware limitation in the obsolete computer system controlling our FIB restricts the number of pixels in a .str file to a maximum of 262144. However, in order to write bigger patterns in a single FOV, one can load several .str files without the risk of stitching errors that occur when translating the sample stage. This restriction is lifted in modern computer systems that have much larger memory capabilities.

Numerical values for sputtering yield given in the literature cannot be taken for granted, because they are very much dependent on experimental conditions. Therefore we did a series of experiments in order to determine the milling time necessary to remove a given amount of material. Milling times for the patterns shown in Figure 5.13 and Figure 5.17 are 7-10 minutes.

5.4.3 Basic idea of our approach

Practical photonic crystal-based photonic integrated circuits would contain both broad and fine features: waveguides (few millimeters long and microns wide) and fiber coupling sections on the one hand and photonic crystal arrays (with lattice constants around 500 nm) on the other hand.

Writing the broad features using E-beam is expensive and time-consuming, especially from the replication point of view. Broad features can be easily and fast transferred to the wafer level by using optical lithography. Photonic crystals for optical frequencies require nm resolution, which can be obtained with FIB. In our view, the combination of moderate resolution optical lithography and FIB etching provides an excellent tool for fast prototyping of PCS-based devices.

We have investigated two fabrication approaches:

- (A) transfer the pattern into a thin metal layer and subsequently use reactive ion etching (RIE) to transfer it into the device layer;
- (B) directly etch the PCS area with FIB into a free-standing membrane.

Approach A is applicable for fabricating asymmetric PCSs (with either solid [Shinya 2002] or patterned bottom cladding [Jamois 2002]) while approach B is applicable for symmetric air-bridge type PCS [Loncar 2000].

The air-bridge PCS has the best theoretical performance because of the following reasons [Johnson 1999]: (a) it has mirror symmetry with respect to the middle plane bisecting the slab, and this makes possible a large gap in even modes; (b) the air light cone gives the largest frequency range available for lossless wave propagation. From a practical point of view, an air-bridge PCS can have a few shortcomings: (a) it is fragile, thus it cannot cover a large area and might need supporting beam structures; (b) optical transitions between dielectric channel waveguides with and without a supporting substrate might give undesired reflections and mode conversions. However, by choosing a relatively small PCS area and carefully designing the waveguide transitions one can overcome these problems.

Our approach uses FIB as a 'lithographic' tool. This means that we are etching shallow holes, and the common problem of tapered sidewalls that occurs when the aspect ratio is bigger than one is eliminated here. Another phenomenon that takes place in FIB etching is implantation of Ga^+ ions into the substrate. In our processes, the 'contaminated' layer is removed during the dry etching process (RIE in approach A and FIB in approach B).

Here we apply FIB milling either into a metal (Cr) or semiconductor (Si). Therefore, by proper sample grounding the charging effect is not an issue. On the other hand, the technology presented here can be applied also for dielectric materials by using an additional charging neutralizing device (like an electron gun).

5.4.4 Fabrication processes and results

Our materials system of choice is silicon-on-insulator (SOI), based on available technology. The starting substrate is a commercially available SOI wafer [S.O.I.TEC] with a 340nm Si device layer on top of a 3.3 μ m SiO₂ layer. The fabrication processes, combining the definition of a coarse pattern (of input and output waveguides and the PCS area between them) and the fine structure (of sub-micron holes aligned with the coarse pattern) are outlined below (detailed description of process recipes is deferred to Appendix E):

Approach A

- sputtering of a thin Cr layer;
- optical lithography for defining the coarse pattern ;
- pattern transfer into the Cr layer;
- FIB etching of sub-micron holes;
- reactive ion etching (RIE) of the Si and SiO₂ layers using a two-step process;
- removing the Cr mask;
- sample inspection.

Approach B

- optical lithography for defining the coarse pattern in Si;
- RIE of top Si layer;
- optical lithography for defining the etch window for the PCS area;
- sacrificial etching the bottom SiO₂ layer;
- FIB etching of sub-micron holes;
- sample inspection.

End-point detection is not critical in approach A, because the Si material will be removed anyway in the subsequent RIE. On the other hand, the end point is easily detectable in approach B: the secondary electron current suddenly changes as soon as the ion beam breaks through the membrane and propagates through empty space shielded by the remaining membrane.

Figure 5.13 shows a structure where a conventional mask with about 1 μ m resolution and wet chemical etching have defined the outlines of the dielectric access waveguides and PCS areas in a metal layer. The FIB-etched hole pattern is aligned with respect to the access waveguides, and the figure shows that FIB resolution is suitable for defining non-circular holes.

The resolution of the laser pattern generator used for making the mask translates into roughness at the edges of Cr pattern on the wafer level; besides, the wet chemical etching of Cr layer produces rounding of sharp corners (see Figure 5.14). The roughness of the coupling waveguides on the mask level will be transferred into the Si layer after the RIE procedure. This will most likely induce very high optical losses of the resulting ridge waveguides. Using a mask made by E-beam can solve this problem.

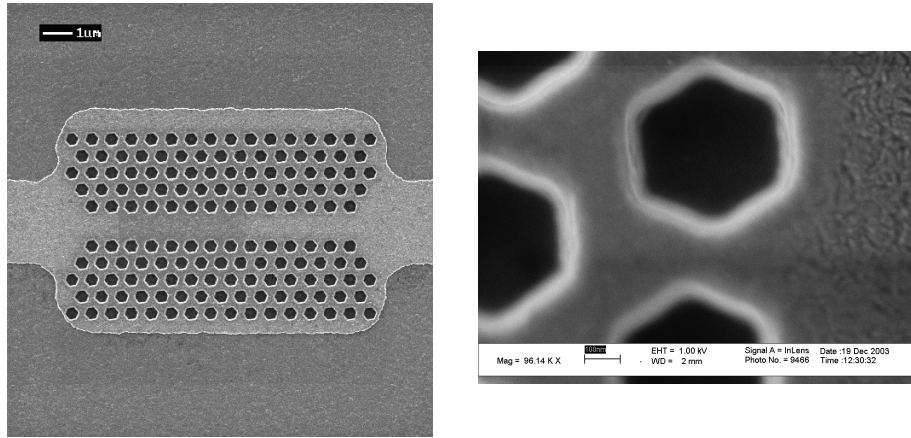


Figure 5.13 *Left: FIB-etched hexagon-type photonic crystal pattern, aligned with waveguide pattern defined by conventional lithography in chromium; Right: detailed view (high-resolution SEM)*

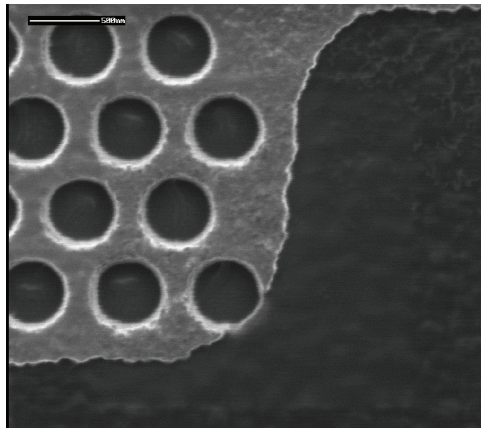


Figure 5.14 *Detailed view of a pattern made of circular holes in a Cr layer; roughness and corner rounding can be seen on the coarse pattern defined by optical lithography (see text); on the other hand, the quality of FIB-etched holes is very good*

Unfortunately, as discussed in section 5.3.3, it turned out that etching of SiO_2 with available RIE gases roughened significantly the Si sidewalls and even sputtered the Cr mask at the holes' edge, leading to a hole enlargement and shape distortion (see Figure 5.7). Sidewall roughness and hole-size variations are very critical issues in photonic crystal applications, therefore RIE of SiO_2 involved in approach A, was discarded and we only considered RIE of Si layer.

Since cleaving can lead to damaging of the interface (see Figure 5.8), FIB was also used for locally characterizing the etch profile obtained in previous etching steps. A cross-sectional view is created by etching a deep slit at a carefully selected position (Figure 5.15). The procedure used for making this slit is similar to the one used for preparing thin-slice specimens for

transmission electron microscopy. It involves several milling steps with different currents, the final step being a very fine polishing.

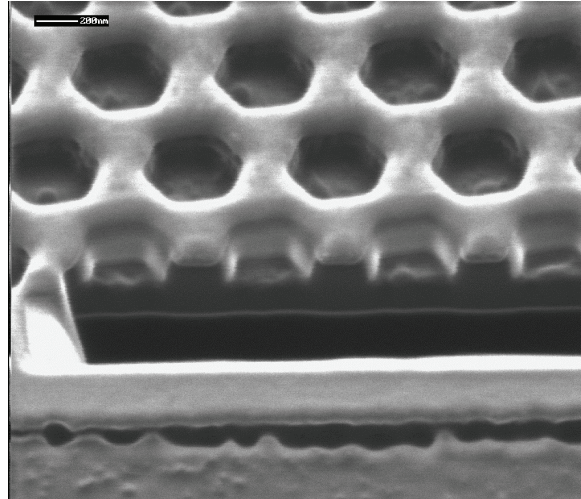


Figure 5.15 FIB cross-section showing the profile of top Si layer after RIE; in this particular case the etch depth was insufficient

Like in electronic circuits, one can use FIB for repairing or trimming the optical waveguides (Figure 5.16) in order to improve the optical coupling: (1) fine polishing of end-facets; (2) tapering the waveguides in the vicinity of connection point with PCS.

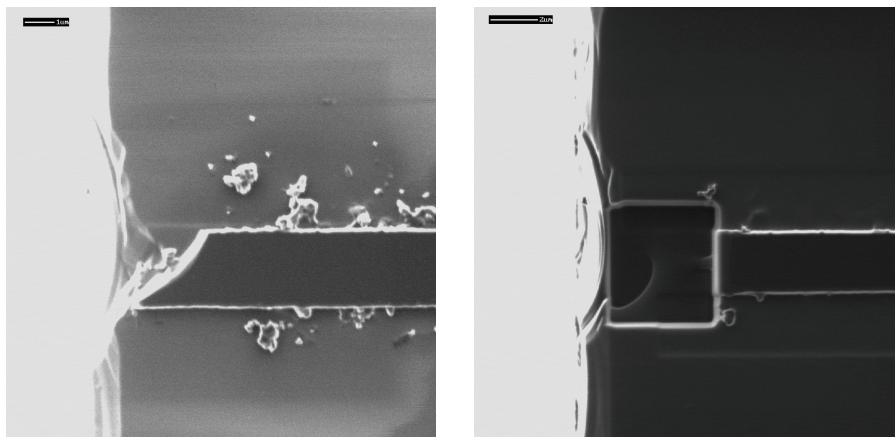


Figure 5.16 Using FIB for repairing a waveguide, fine polishing of end-facets and cleaning the debris produced by dicing; pictures show a sample before (left) and after (right) FIB procedure

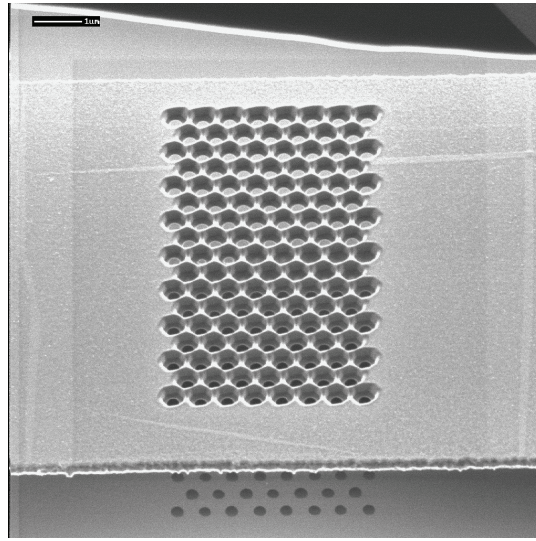


Figure 5.17 Free-standing Si membrane with PCS area directly etched through it by FIB; the projection of the PCS onto the substrate is clearly observable

Figure 5.17 shows a freestanding Si membrane with the PCS area directly etched through it by FIB. The projection of the PCS onto the substrate is clearly observable, demonstrating that the etching has been completed. Moreover, the projected holes are not much distorted and this is a proof of large depth-of-focus of the FIB.

5.5. Discussion

Two-beam LIL is a fast and cheap technology for producing large area PCS with perfect periodicity. However, it suffers from a number of shortcomings:

- (a) the 'filling factor' is not uniform over the exposure area and the hole shape is elliptical, which leads to a decrease of the bandgap size;
- (b) the rate of reproducibility is quite low because several process steps are critical and very difficult to control (these are sensitive to environmental conditions, too);
- (c) it is difficult to introduce defects precisely aligned with other integrated optical components.

FIB is an expensive technology that can be used for fabricating with high precision small area PCSs aligned with optical coupling structures. FIB can be combined with optical lithography for fast prototyping of PCS. Like EBL, FIB can suffer from stitching errors. Using an interferometric stage can alleviate this problem. However, stitching errors do not occur for PCS that fit a single FOV, and this size is large enough to incorporate functional devices. Unlike EBL, FIB does not need special measures for proximity correction if applied to a conductive substrate. Although it is expensive, FIB can combine three processes in one (lithography, etching, sample inspection) and can be applied

for polishing the end facets of optical waveguides. The main disadvantage of FIB for production is the slow processing and low throughput. A possible solution for low-cost mass production is to use embossing and nano-contact printing [Li 2003a] to replicate the structures formed using FIB lithography. The FIB used for the experiments performed in this thesis has another disadvantage: the alignment of the FIB pattern with respect to the coarse pattern obtained by optical lithography has to be done manually. This time-consuming procedure can be avoided in modern FIB machines that have pattern recognition capabilities than can be used for process automation.

Chapter 6 Preliminary characterization

In this short chapter some preliminary characterization measurements are presented that have been performed in the available time. The aim of these measurements is to investigate the PBG properties of the fabricated PCS components discussed in Chapter 5.

6.1. Experimental setup

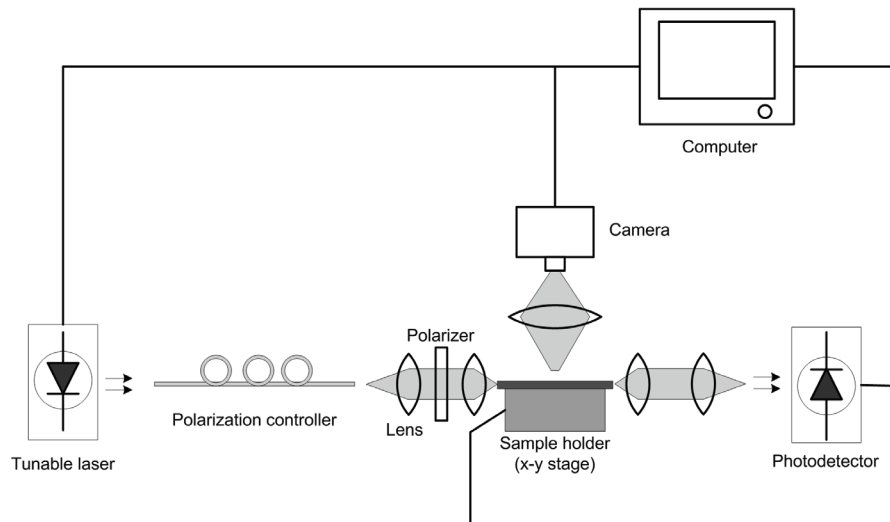


Figure 6.1 Simplified schematic of the experimental setup using end-fire coupling

The experimental setup, using end-fire coupling, is shown in Figure 6.1. The light source is a tunable laser (Hewlett-Packard HP8168C), with a wavelength range $\lambda=1500\text{-}1600\text{nm}$. The maximum output power is $P_{\max}=2.5\text{ mW}$. The light emitted by the source passes successively through a polarization controller (made of a few fiber coils), a collimating lens, a polarizer and a focusing lens. The focusing lens is a high numerical aperture lens (typical $\text{NA}=0.65$) that produces a small spot (diameter of the order of the wavelength) that is directed onto the input facet of the waveguide. Efficient incoupling is difficult to obtain as the height of the waveguide core is approximately 300 nm , much smaller than the spot size. In addition, there is a strong Fresnel reflection at the input facet, because of the large difference in the refractive indices between air and silicon. This Fresnel reflection reduces also the outcoupling. The overall coupling loss is estimated to be -20 dB .

The sample is placed on a vacuum chuck, which is fixed on a 2-axis translation stage that can be controlled with nanometer accuracy.

While passing through the sample, light is scattered in the vertical direction due to roughness of the waveguides' sidewalls and the diffraction loss from the PCS. The scattered light, collected by a camera placed above the sample, provides information about the quality of our sample (i.e. for a good sample the intensity of scattered light is small). Through appropriate image processing applied to the images acquired by the camera, quantitative information on the propagation losses can also be extracted [Tan 2003].

At the sample end facet, light is coupled out and focused onto a photodetector by using a lens system.

A computer system controls the wavelength setting of the tunable laser, the voltage applied to the piezoelectric nano-positioning system and the voltage applied to the motor-driven camera stage. At the same time, the computer system acquires data from the photodetector and images from the camera and saves them on disk.

6.2. Experimental procedure and results

First, a rough alignment is done manually using a visible light source (HeNe laser, $\lambda=633\text{nm}$). Then, the visible light source is switched off and the infrared light source is switched on. A fine alignment is done using the voltage-driven piezoelectric actuators, using as visual feedback the image captured by the camera placed above the input facet of the waveguide (see Figure 6.2). After obtaining a satisfactory alignment, we start the computer routine for automatic data acquisition that performs the following operations:

1. scanning the wavelength of the tunable laser, in small steps (0.1nm);
2. recording the signal from the photodetector for each wavelength;
3. recording the frames grabbed by the camera, for each wavelength and for several positions along the waveguide

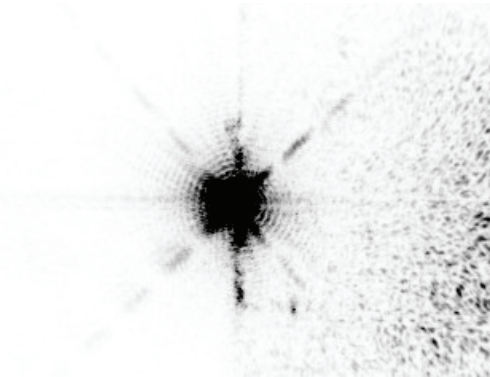


Figure 6.2 Image of the input facet captured by the IR camera (the grey scale has been inverted, for clarity)

In Figure 6.3 an example of an image captured by the camera is given, showing the propagation of infrared light from the input waveguide towards

the PCS area. Weak scattering from the sidewalls of the input waveguide can be seen, whereas the PCS area is a strong scatterer.

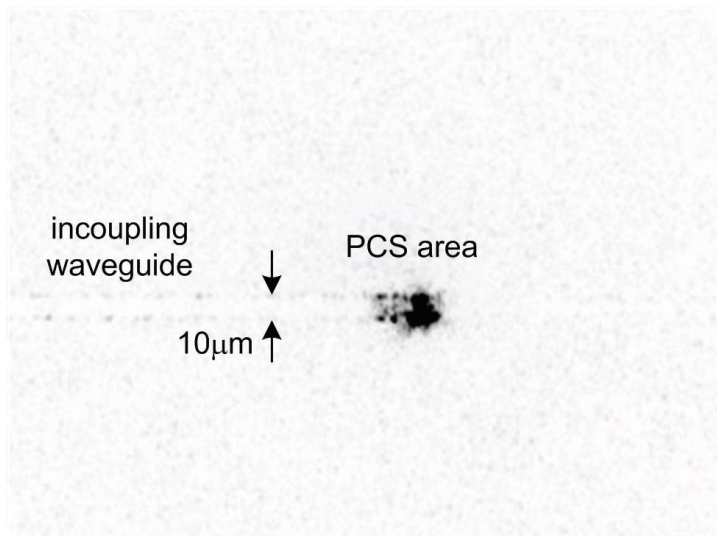


Figure 6.3 Propagation of infrared light ($\lambda_0=1.55\mu\text{m}$) from the input waveguide towards the PCS area (camera image)

The output power signal as a function of wavelength gives the transmittance spectrum. However, this spectrum is composed of several contributions: the spectrum of the input light, the spectral transmittance of the optical system, the spectral characteristics of in/out coupling, the spectral transmittance of our device and the spectral response of the photodetector. We would like to get meaningful information only about the spectral transmittance of the PCS structure, in order to identify and quantify the PBG region. Therefore, in order to minimize the effect of the other contributing factors, we consider a reference structure that consists of in/out coupling waveguides, without the PCS area. The transmittance spectrum of the device containing the PCS area is then normalized with respect to the transmittance spectrum of the reference structure.

Instead of using the signal provided by the photodetector, we can use a complementary method for determining the spectral transmittance. This method is based on a quantitative image analysis of the images acquired by the camera, as a function of wavelength [Tan 2003]. The method consists in calculating the average intensity over a spatial region of interest (e.g. PCS). The method relies on the assumption that the intensity of the scattered light is proportional to the local intensity of the electromagnetic field. When selecting the region of interest, it is recommended to avoid the sizable “scattering points” induced by fabrication imperfections. On the other hand, the amount of scattered light should be detectable by the camera (in other words, the structure should not be “perfect”, without any scattering losses). This condition is for our devices always fulfilled due to the high sensitivity of the camera.

Preliminary characterization

In the transmission measurements we encountered some unexpected problems. The output signal was very unstable and largely fluctuating over short periods of time (below 1s). The most probable reason is a fault in the translation stage used for outcoupling. Still, the incoupling was very stable, which made possible wavelength scans and camera image acquisitions for different wavelengths. However, because of lack of automation, the processing of these images requires an amount of work that couldn't be completed in the available time.

Chapter 7 Summary and conclusions

In this thesis we have presented design procedures, fabrication techniques and preliminary measurements of photonic-crystal based integrated optical components.

In Chapter 1 an attempt is made to present the basic concepts of photonic crystal physics in an intuitive way, while sacrificing the mathematical rigor as little as possible.

Chapter 2 contains an overview of most common computational methods and modeling tools applicable to photonic crystal (PhC) analysis and design. The emphasis is put on strengths and weaknesses of each method. In the design process of photonic crystals considered in this thesis, two kinds of problems have been addressed: band diagrams of unbounded photonic crystals with 2D periodicity, using the plane wave expansion method (PWEM) and wave propagation in finite-sized photonic crystals, including their coupling to the outside world (in 2D by using the finite-element method (FEM) and in 3D by finite-difference time-domain (FDTD)).

Chapter 3 contains calculation results for silicon on insulator (SOI)-based 2D PhCs and 3D photonic crystal slabs (PCS), and design and optimization criteria derived from them. An SOI-based PCS can be used as a platform for integrating “defects”, e.g. point-like cavities and line-defects. Depending on application, the design rules might differ. The choice of the lattice configuration depends on the application. With high air filling factors achieved by rotating the hexagonal “atoms” one can obtain absolute gaps in guided modes situated at higher frequencies in the band diagram. Then, a “defect” mode of a point-like cavity emitter will couple only to leaky and radiation modes and the extraction efficiency will be increased. For line-defect waveguides it is essential to keep the losses down to a level as low as possible. This asks for a low working frequency and a moderate filling factor. In this case, an absolute gap is not possible, and one has to rely on a partial gap (the region of the projected band diagram bounded by the fundamental E-like and H-like modes seems the most promising alternative). The slab thickness has an optimum value, which gives the best mode confinement in the PCS core layer. Vertical symmetry of a PCS is desirable because it allows more freedom in controlling mode coupling and selective mode excitation. The air-bridge PCS seems to have the best performance for all applications, despite its lower mechanical stability as compared to other types of PCS: the substrate leakage loss is minimum, it is vertically symmetric, and the transmission window is the largest achievable.

Chapter 4 refers to the design of line defect waveguides for the purpose of optical signal transport. Detailed engineering of the W1 line defects (defects produced by omitting a single line of holes from the lattice) proved to be necessary in order to achieve the desired characteristics: broad bandwidth,

single-mode, low-losses. We proposed a novel hybrid design (hexagonal holes plus triangular inclusions) in which the PhC waveguide resembles closely a ridge waveguide. The size and positions of these inclusions modify the effective index of the waveguide independently of the lattice constant (in some cases without lattice distortion) and also minimize the effect of boundary corrugations. Propagation losses on the order of 15 dB/mm for H-like excitation were obtained.

The waveguides can be combined to form efficient bends and Y-junctions. The bends and Y-junctions include intermediate short waveguide sections at half the bend angle playing the role of corner ‘mirrors’. PhC’s may be a good way for obtaining small high-Q resonators or sensing elements, which should be coupled to the outside world through waveguides. For combining several of these basic devices, possibly in Mach-Zehnder interferometer (MZI)-configurations, bends and Y-junctions are needed. In principle, these could be made almost as small using conventional high-index waveguides. An important reason for implementing them with PhC waveguides is the difficulty of matching conventional waveguides to PhC waveguides (probably a lot of those transitions result in larger overall loss and larger size than implementing the entire circuit in PhC). In this case the coupling efficiency with in/out ridge waveguides has a more prominent role than radiation losses. One has also to consider the wavelength dependency of the transmission, due to distributed Bragg reflection (DBR) and Fabry-Perot effects (these depend on the length of the line defect arms). For high-contrast materials, the bending loss of conventional waveguides can be very low for radii of only a few microns. Therefore, for the purpose of pure signal transport, a photonic wire will always win. PhC waveguides can probably only be motivated by their combination with other functions (e.g. resonators, nonlinear optics, sensor structures). It seems very hard to obtain polarization-independent functioning in these devices.

In Chapter 5 we presented fabrication techniques for photonic crystals. We discussed two patterning techniques with nanometer resolution, namely laser interference lithography (LIL) and focused ion beam (FIB) processing. Two-beam LIL is a fast and cheap technology for producing large area PCS with perfect periodicity. However, it suffers from a number of shortcomings:

- (d) the ‘filling factor’ is not uniform over the exposure area and the hole shape is elliptical, which leads to a decrease of the bandgap size;
- (e) the rate of reproducibility is quite low because several process steps are critical and very difficult to control (these are sensitive to environmental conditions, too);
- (f) it is difficult to introduce defects precisely aligned with other integrated optical components.

FIB is an expensive technology that can be used for fabricating with high precision small area PCS aligned with optical coupling structures. FIB can be combined with optical lithography for fast prototyping of PCS. Like electron-beam lithography (EBL), FIB can suffer from stitching errors, due to the limited area that is directly addressable by the beam, the field of view (FOV). Using an interferometric translation stage can alleviate this problem.

However, stitching errors do not occur for PCS that fit a single FOV, and this size is large enough to incorporate functional devices. Unlike EBL, FIB does not need special measures for proximity correction if applied to a conductive substrate. Although it is expensive, FIB can combine three processes in one (lithography, etching, sample inspection, even a local cross-section at a precisely determined position) and it can be applied for polishing the end facets of optical waveguides. The main disadvantage of FIB for production is slow processing and low throughput. A possible solution for low-cost mass production is to use embossing or nano-contact printing to replicate the structures formed using FIB lithography. The FIB used for the experiments performed in this thesis has another disadvantage: the alignment of the FIB pattern with respect to the coarse pattern obtained by optical lithography has to be done manually. This time-consuming procedure can be avoided in modern FIB machines that have pattern recognition capabilities than can be used for process automation.

Summary and conclusions

Samenvatting en conclusies

In dit proefschrift worden ontwerpprocedures en fabricagemethoden beschreven voor geïntegreerde optische componenten op basis van fotonische kristallen ("photonic crystals" - PhC's). Hoofdstuk 1 is een inleiding in de basisconcepten van de fysica van PhC's, waarin aansluiting wordt gezocht bij een intuïtief begrip zonder de wiskundige gestrengheid geweld aan te doen.

Hoofdstuk 2 bevat een overzicht van de meest gebruikelijke rekenmethoden en modelleringsgereedschappen die worden toegepast bij de analyse en het ontwerp van PhC's. Bijzondere aandacht wordt gegeven aan de sterke en zwakke punten van elke methode. Met betrekking tot het ontwerpproces van de fotonische kristallen die in dit proefschrift worden beschouwd, zijn twee soorten problemen behandeld: (1) banddiagrammen van onbegrensde, oneindig uitgestrekte fotonische kristallen met een tweedimensionale (2D) periodiciteit, berekend met een methode gebaseerd op een fourierontbinding van de periodieke brekingsindexstructuur en de veldoplossingen (de "plane wave expansion method" - PWEM), en (2) golfvoortplanting in eindige fotonische kristallen en de koppeling van deze golven naar de buitenwereld, berekend met enerzijds de methode der eindige elementen ("finite element method" - FEM) voor 2D-problemen en anderzijds de methode van eindige differenties in het tijddomein ("finite-difference time-domain" - FDTD) voor 3D problemen.

Hoofdstuk 3 bevat resultaten van berekeningen aan 2D PhC's in silicium en 3D berekeningen aan diëlektrische plaatgolfsgeleiders met een 2D periodieke perforatie (in het Engels beter bekend als "photonic crystal slabs" - PCS'en), die vervaardigd kunnen worden uit substraten die bestaan uit een dun laagje silicium op siliciumoxide (silicium op isolator - SOI). Uit deze berekeningen zijn criteria afgeleid voor ontwerp en optimalisatie van dergelijke structuren. Een PCS die gebaseerd is op SOI kan dienen als platform voor integratie van zogenaamde functionele defecten, punt- of lijnvormige verstoringen van de periodiciteit die kunnen dienen als trilholtte of golfsgeleider. Afhankelijk van de toepassing kunnen verschillende ontwerpregels van kracht zijn voor de configuratie van het periodieke rooster en de gaten die op dat rooster zijn gecentreerd. Er is gevonden dat zeshoekige gaten in een driehoekig rooster het mogelijk maken een structuur te realiseren waarin zoveel mogelijk silicium (een materiaal met een hoge brekingsindex) is vervangen door lucht terwijl toch het resterende silicium een verbonden netwerk blijft vormen. Een dergelijke structuur met een hoge "lucht-vulfactor" kan een absolute bandkloof vertonen in de geleide modi bij hogere genormaliseerde frequenties, d.w.z. dat er frequentiegebieden te vinden zijn waarin geen golven door de structuur geleid kunnen worden, onafhankelijk van de polarisatie van die golven. Een potentiële toepassing daarvan is het verhogen van het stralingsrendement van een lichtemitter in een puntdefect doordat deze

uitsluitend kan koppelen met niet-geleide (lekkende, Eng. "leaky") modi van de omringende structuur en stralingsmodi. Anderzijds moeten voor golfgeleiders gebaseerd op lijndefecten deze stralingsverliezen juist laag worden gehouden, wat leidt tot de keuze voor een matig hoge lucht-vulfactor en een lage genormaliseerde werkfrequentie. In dit geval is een absolute bandkloof niet mogelijk en moet men genoegen nemen met een partiële kloof (het meestbelovend is het gebied in het geprojecteerde banddiagram dat wordt begrensd door de fundamentele modi van de beide mogelijke polarisaties). Hieruit volgt de belangrijke conclusie dat functionele structuren in een PCS niet polarisatie-onafhankelijk kunnen worden ontworpen. Voor de dikte van het siliciumlaagje bestaat een optimale waarde waarbij het licht van een geleide modus maximaal wordt opgesloten in deze siliciumkern. Verticale symmetrie is een wenselijke eigenschap van een PCS omdat dit meer vrijheid geeft voor het beheersen van de koppeling tussen modi en het selectief aanslaan van een specifieke modus. Door het plaatselijk verwijderen van oxide onder het silicium ontstaat een luchtbrug met verticale symmetrie (brekingsindices boven en onder het silicium zijn gelijk). Ondanks de potentieel geringere mechanische stabiliteit van zo'n brug wordt hiervan toch de beste werking voor alle toepassingen verwacht omdat de structuur symmetrisch is, de verliezen naar het substraat worden geminimaliseerd en het bruikbare frequentiegebied maximaal is.

Hoofdstuk 4 behandelt het ontwerp van golfgeleiders voor optisch signaaltransport in een PCS. Een lijndefect, gevormd door het weglaten van een enkele rij gaten uit een PCS is bekend als een zogenaamde W1-golfgeleider. Gedetailleerd ontwerp van een dergelijke golfgeleider is noodzakelijk om een combinatie van gewenste eigenschappen te bereiken: geleiding van een enkele modus, grote optische bandbreedte en lage verliezen. Een nieuw hybride ontwerp wordt voorgesteld dat is opgebouwd uit zeshoekige gaten in combinatie met driehoekige "opvulgaten" om een golfgeleider te krijgen met zo recht mogelijke zijwanden. Hierdoor lijkt het kanaal op een klassieke diëlektrische golfgeleider. Door de keuze van afmetingen en positie van de opvulgaten kan de effectieve brekingsindex van de golfgeleider onafhankelijk van de roosterconstante van het PhC worden ingesteld (in sommige gevallen zonder vervorming van dit rooster), terwijl tevens het ongewenste effect van de periodieke verstoring van de zijwanden van het kanaal (veroorzaakt door het omringende periodieke rooster) kan worden geminimaliseerd. Voor modi met hun magnetische veldcomponent hoofdzakelijk loodrecht op het vlak van de PCS zijn theoretische voortplantingsverliezen van 15 dB/mm gevonden.

De golfgeleiders kunnen gecombineerd worden tot efficiënte bochten en tweesprongen (Y-juncties). Deze elementen bevatten zeer korte kanaalsecties op de halve afbuigingshoek, die kunnen worden opgevat als hoekspiegels.

Fotonische kristallen maken het wellicht mogelijk om zeer kleine resonatoren met hoge kwaliteitsfactor (Q) en zeer kleine optische sensoren te realiseren. Om deze elementen met de buitenwereld te verbinden en om samengestelde componenten ermee te kunnen maken (bijvoorbeeld in de vorm van een Mach-Zehnder interferometer) zijn golfgeleiders, bochten en

juncties nodig. In principe kunnen die elementen vrijwel net zo compact (en in veel gevallen met lagere verliezen) ook als klassieke diëlektrische golfgeleiders worden uitgevoerd in een systeem met een zeer hoog brekingsindexcontrast (zoals silicium/lucht of silicium/siliciumoxide). Een belangrijke reden om de elementen toch binnen het fotonisch kristal te realiseren is het probleem van een efficiënte koppeling tussen klassieke golfgeleiders en PhC-golfgeleiders. Herhaalde overgangen tussen PhC- en klassieke kanalen kunnen leiden tot een accumulatie van koppelverliezen en andere ongewenste effecten van misaanpassingen, zoals parasitaire Fabry-Perot resonanties, die een ongunstiger effect hebben op de eigenschappen van de samengestelde functie dan de hogere verliezen van PhC-kanalen.

In hoofdstuk 5 worden fabricagetechnieken voor planaire fotonische kristallen gepresenteerd. Er worden twee verschillende technieken besproken die een resolutie op nanometer-schaal bieden, laser-interferentielithografie (LIL) en bewerking met een gefocuseerde ionenbundel ("focused ion beam" - FIB). De LIL op basis van het interferentiepatroon van twee lichtbundels in het ultraviolet is een snelle en goedkope technologie voor het vervaardigen van PCS'en met een perfecte periodiciteit over een groot oppervlak. De methode heeft echter een aantal nadelen die de toepassing voor fotonische kristallen in de weg staan:

- a. de vulfactor is niet uniform over het belichte oppervlak en de vorm van de gaten in een driehoekig rooster (gedefinieerd door een dubbele belichting onder verschillende hoeken) is elliptisch, waardoor de bandkloof kleiner wordt;
- b. de reproduceerbaarheid van het proces is slecht doordat meerdere kritische processtappen zeer moeilijk beheersbaar zijn, mede door hun gevoeligheid voor omgevingsinvloeden;
- c. functionele defecten (zoals W1 golfgeleiders) zijn zeer lastig uit te lijnen op andere geïntegreerde optische structuren die noodzakelijk op andere wijze (conventionele lithografie) moeten worden gedefinieerd, bijv. golfgeleiders die de structuur met de buitenwereld moeten verbinden.

FIB is een technologie die hoge investeringskosten vergt, waarmee met zeer hoge nauwkeurigheid kleine PCS-structuren kunnen worden gemaakt die nauwkeurig zijn uitgericht op van te voren op andere wijze gedefinieerde geïntegreerde optische elementen. Doordat de technologie drie processen (lithografie, etsen en inspectie van het specimen) combineert kan de methode in combinatie met optische lithografie worden gebruikt om snel prototypen te vervaardigen. Doordat de ionenbundel slechts een beperkt gebied rechtstreeks kan bereiken is voor het vervaardigen van grote structuren tussentijdse verplaatsing van het substraat nodig. Evenals bij lithografie met elektronenbundels ("e-beam lithography" - EBL) kunnen dan zogenaamde weeffouten ontstaan (Eng.: "stitching errors") waarbij een doorlopend patroon niet goed aansluit. Doordat PCS-structuren wegens hun compactheid meestal in hun geheel binnen het "gezichtsveld" van de ionenbundel vallen, kunnen deze weeffouten in de praktijk worden vermeden. Anders dan bij EBL is het bij FIB niet nodig om te corrigeren voor bundelafwijkingen tengevolge van

opladingseffecten door de ionenbundel als de techniek wordt toegepast op een geleidend substraat zoals silicium of een metaalfilm. Een extra voordeel van FIB is dat lokaal een doorsnede van een deel van de structuur kan worden gemaakt en afgebeeld zonder de rest van het specimen te beschadigen. Tevens kan de methode worden gebruikt om optische eindvlakken te polijsten ten behoeve van een goede koppeling met de buitenwereld. Het belangrijkste nadeel van FIB is de geringe verwerkingssnelheid en doorvoercapaciteit, waardoor de methode ongeschikt is voor massaproductie. Een mogelijke oplossing hiervoor is het toepassen van een nano-contactafdrukmethode waarbij de matrijs of een voorloper daarvan gemaakt wordt met FIB.

De FIB machine die voor het hierbeschreven werk ter beschikking stond had de beperking dat de uitrichting van de fijnstructuur op de eerder vervaardigde grovere structuur met de hand moest worden uitgevoerd. In moderne FIB-machines die beschikken over de mogelijkheid om bestaande patronen op een substraat te herkennen kan deze tijdrovende procedure geautomatiseerd worden.

Appendix A Proof that $\hat{\Theta}_H$ operator is Hermitian

We use the vector identity:

$$\vec{\nabla} \cdot (\vec{A} \times \vec{B}) = (\vec{\nabla} \times \vec{A}) \cdot \vec{B} - \vec{A} \cdot (\vec{\nabla} \times \vec{B}) \quad (\text{A.1})$$

and the scalar product definition

$$\langle \vec{F}, \vec{G} \rangle = \int_{\Omega} d^3 r \vec{F}^*(\vec{r}) \cdot \vec{G}(\vec{r}) \quad (\text{A.2})$$

We will prove that the operator:

$$\hat{\Theta}_H \equiv \vec{\nabla} \times \frac{1}{\varepsilon_r(\vec{r})} \vec{\nabla} \times \quad (\text{A.3})$$

is Hermitian, when acting on Bloch functions which satisfy the quasi-periodicity condition $\vec{F}(\vec{r} + \vec{R}_l) = e^{i\vec{k}\vec{R}_l} \vec{F}(\vec{r})$. The following equality should be fulfilled: $\langle \hat{\Theta}_H \vec{F}, \vec{G} \rangle = \langle \vec{F}, \hat{\Theta}_H \vec{G} \rangle$.

We start with:

$$\langle \hat{\Theta}_H \vec{F}, \vec{G} \rangle = \int_{\Omega} d^3 r \left\{ \vec{\nabla} \times \left[\frac{1}{\varepsilon_r(\vec{r})} \vec{\nabla} \times \vec{F}^*(\vec{r}) \right] \cdot \vec{G}(\vec{r}) \right\} \quad (\text{A.4})$$

Applying (A.1) with $\vec{A} \equiv 1/\varepsilon_r(\vec{r}) \vec{\nabla} \times \vec{F}^*(\vec{r})$ and $\vec{B} \equiv \vec{G}(\vec{r})$ we get:

$$\langle \hat{\Theta}_H \vec{F}, \vec{G} \rangle = \int_{\Omega} d^3 r \vec{\nabla} \cdot \left[\left(\frac{1}{\varepsilon_r(\vec{r})} \vec{\nabla} \times \vec{F}^*(\vec{r}) \right) \times \vec{G}(\vec{r}) \right] + \int_{\Omega} d^3 r \frac{1}{\varepsilon_r(\vec{r})} (\vec{\nabla} \times \vec{F}^*(\vec{r})) \cdot (\vec{\nabla} \times \vec{G}(\vec{r})) \quad (\text{A.5})$$

For the first integral in (A.5) we apply Gauss' theorem:

$$\int_{\Omega} d^3 r \vec{\nabla} \cdot \left[\left(\frac{1}{\varepsilon_r(\vec{r})} \vec{\nabla} \times \vec{F}^*(\vec{r}) \right) \times \vec{G}(\vec{r}) \right] = \int_{\partial\Omega} d^2 r \left[\left(\frac{1}{\varepsilon_r(\vec{r})} \vec{\nabla} \times \vec{F}^*(\vec{r}) \right) \times \vec{G}(\vec{r}) \right] \cdot \hat{n} = 0 \quad (\text{A.6})$$

In (A.6) $\partial\Omega$ is the surface enclosing the volume Ω and \hat{n} is the unit normal to $\partial\Omega$ pointing outwards. The integrand is a periodic function (the phase factors cancel out), therefore the integral is null because contributions of the opposite boundaries cancel each other.

Then (A.5) becomes:

Proof that $\hat{\Theta}_H$ operator is Hermitian

$$\langle \hat{\Theta}_H \vec{F}, \vec{G} \rangle = \int_{\Omega} d^3r (\vec{\nabla} \times \vec{F}^*(\vec{r})) \cdot \frac{1}{\epsilon_r(\vec{r})} (\vec{\nabla} \times \vec{G}(\vec{r})) \quad (\text{A.7})$$

Applying (A.1) with $\vec{A} \equiv \vec{F}^*(\vec{r})$ and $\vec{B} \equiv 1/\epsilon_r(\vec{r}) \vec{\nabla} \times \vec{G}(\vec{r})$ in (A.7) we get:

$$\langle \hat{\Theta}_H \vec{F}, \vec{G} \rangle = \int_{\Omega} d^3r \vec{\nabla} \cdot \left[\vec{F}^*(\vec{r}) \times \left(\frac{1}{\epsilon_r(\vec{r})} \vec{\nabla} \times \vec{G}(\vec{r}) \right) \right] + \int_{\Omega} d^3r \vec{F}^*(\vec{r}) \cdot \left[\vec{\nabla} \times \frac{1}{\epsilon_r(\vec{r})} (\vec{\nabla} \times \vec{G}(\vec{r})) \right] \quad (\text{A.8})$$

Once again, we apply Gauss' theorem:

$$\int_{\Omega} d^3r \vec{\nabla} \cdot \left[\vec{F}^*(\vec{r}) \times \left(\frac{1}{\epsilon_r(\vec{r})} \vec{\nabla} \times \vec{G}(\vec{r}) \right) \right] = \int_{\partial\Omega} d^2r \left[\vec{F}^*(\vec{r}) \times \left(\frac{1}{\epsilon_r(\vec{r})} \vec{\nabla} \times \vec{G}(\vec{r}) \right) \right] \cdot \hat{n} = 0 \quad (\text{A.9})$$

Finally, (A.8) becomes:

$$\langle \hat{\Theta}_H \vec{F}, \vec{G} \rangle = \int_{\Omega} d^3r \vec{F}^*(\vec{r}) \cdot \left[\vec{\nabla} \times \frac{1}{\epsilon_r(\vec{r})} (\vec{\nabla} \times \vec{G}(\vec{r})) \right] = \langle \vec{F}, \hat{\Theta}_H \vec{G} \rangle \quad (\text{A.10})$$

which proves that operator $\hat{\Theta}_H$ is Hermitian

As a consequence, the Bloch functions form a complete orthonormal set. As noted by Sipe [Sipe 2000] the complete set should include the nonphysical fields $\vec{\nabla} \cdot \vec{H}(\vec{r}) \neq 0$ that correspond to static solutions. The Bloch functions can be used as basis for expanding the electromagnetic field in perfect periodic photonic crystals. Moreover, one can derive from the Bloch functions a set of Wannier functions [Busch 2003] that provide an efficient way of expressing the fields localized around 'defects' in photonic crystals.

Appendix B Derivation of the PWEM eigenvalue equation

In Chapter 2, the Fourier expansions for the inverse of dielectric constant $\varepsilon_r(\vec{r})$ and the $\vec{H}_{\vec{k}}(\vec{r})$ field were given:

$$1/\varepsilon_r(\vec{r}) = \sum_{\vec{G}, \vec{G}'} \varepsilon^{-1}(\vec{G} - \vec{G}') e^{i(\vec{G} - \vec{G}') \cdot \vec{r}} \quad (\text{B.1})$$

$$\vec{H}_{\vec{k}}(\vec{r}) = \sum_{\vec{G}} \vec{h}_{\vec{G}} e^{i(\vec{k} + \vec{G}) \cdot \vec{r}} \quad (\text{B.2})$$

The equation (B.1) is used in the *HCS method*.

Using the vector identity $\vec{\nabla} \times \vec{h}_{\vec{G}} e^{i(\vec{k} + \vec{G}) \cdot \vec{r}} = i e^{i(\vec{k} + \vec{G}) \cdot \vec{r}} (\vec{k} + \vec{G}) \times \vec{h}_{\vec{G}}$ we obtain:

$$\vec{\nabla} \times \vec{H}_{\vec{k}}(\vec{r}) = i \sum_{\vec{G}'} \left[(\vec{k} + \vec{G}') \times \vec{h}_{\vec{G}'} \right] e^{i(\vec{k} + \vec{G}') \cdot \vec{r}} \quad (\text{B.3})$$

We insert (B.2) and (B.3) in the wave equation (1.13)

$$\vec{\nabla} \times (1/\varepsilon_r(\vec{r}) \vec{\nabla} \times \vec{H}_{\vec{k}}(\vec{r})) = (\omega/c)^2 \vec{H}_{\vec{k}}(\vec{r}) :$$

$$\vec{\nabla} \times \left\{ \left[\sum_{\vec{G}, \vec{G}'} \varepsilon^{-1}(\vec{G} - \vec{G}') e^{i(\vec{G} - \vec{G}') \cdot \vec{r}} \right] i \sum_{\vec{G}'} \left[(\vec{k} + \vec{G}') \times \vec{h}_{\vec{G}'} \right] e^{i(\vec{k} + \vec{G}') \cdot \vec{r}} \right\} = \left(\frac{\omega}{c} \right)^2 \sum_{\vec{G}} \vec{h}_{\vec{G}} e^{i(\vec{k} + \vec{G}) \cdot \vec{r}} \quad (\text{B.4})$$

The left-hand side of (A.3) can be simplified to:

$$i \sum_{\vec{G}} \vec{\nabla} \times \left\{ \sum_{\vec{G}'} \left[(\vec{k} + \vec{G}') \times \vec{h}_{\vec{G}'} \right] \varepsilon^{-1}(\vec{G} - \vec{G}') e^{i(\vec{k} + \vec{G}') \cdot \vec{r}} \right\} \quad (\text{B.5})$$

From equations (B.3) and (B.5), by identification of Fourier coefficients we obtain:

$$\sum_{\vec{G}'} \left\{ \left[(\vec{k} + \vec{G}') \times \vec{h}_{\vec{G}'} \right] \times (\vec{k} + \vec{G}') \right\} \varepsilon^{-1}(\vec{G} - \vec{G}') = \left(\frac{\omega}{c} \right)^2 \vec{h}_{\vec{G}} \quad (\text{B.6})$$

The transversality of $\vec{H}_{\vec{k}}(\vec{r})$ field can be easily expressed in the PWEM:

$$\vec{\nabla} \cdot \vec{H}_{\vec{k}}(\vec{r}) = 0 \Rightarrow (\vec{k} + \vec{G}) \cdot \vec{h}_{\vec{G}} = 0 \quad (\text{B.7})$$

which means that $\vec{h}_{\vec{G}} \perp (\vec{k} + \vec{G})$ and $\vec{h}_{\vec{G}}$ can be expanded as:

$$\vec{h}_{\vec{G}} = h_{1\vec{G}} \hat{e}_{1\vec{G}} + h_{2\vec{G}} \hat{e}_{2\vec{G}} \quad (\text{B.8})$$

where $\{\hat{e}_{1\bar{G}}, \hat{e}_{2\bar{G}}, \hat{e}_{k\bar{G}} = \bar{k} + \bar{G}/|\bar{k} + \bar{G}|\}$ form a Cartesian right-handed triad (see Figure 2.1), satisfying the following relations:

$$\begin{aligned} (\bar{k} + \bar{G}) \times \hat{e}_{1\bar{G}} &= |\bar{k} + \bar{G}| \hat{e}_{2\bar{G}} \\ (\bar{k} + \bar{G}) \times \hat{e}_{2\bar{G}} &= -|\bar{k} + \bar{G}| \hat{e}_{1\bar{G}} \end{aligned} \quad (\text{B.9})$$

Using (B.9) and (B.8) we get:

$$(\bar{k} + \bar{G}') \times \bar{h}_{\bar{G}'} = |\bar{k} + \bar{G}'| (h_{1\bar{G}'} \hat{e}_{2\bar{G}'} - h_{2\bar{G}'} \hat{e}_{1\bar{G}'}) \quad (\text{B.10})$$

In the right hand side of (B.10) we perform a coordinate transformation:

$$h_{1\bar{G}'} \hat{e}_{2\bar{G}'} - h_{2\bar{G}'} \hat{e}_{1\bar{G}'} = \alpha \hat{e}_{1\bar{G}} + \beta \hat{e}_{2\bar{G}} \quad (\text{B.11})$$

where:

$$\begin{aligned} \alpha &= h_{1\bar{G}'} (\hat{e}_{2\bar{G}'} \cdot \hat{e}_{1\bar{G}}) - h_{2\bar{G}'} (\hat{e}_{1\bar{G}'} \cdot \hat{e}_{1\bar{G}}) \\ \beta &= h_{1\bar{G}'} (\hat{e}_{2\bar{G}'} \cdot \hat{e}_{2\bar{G}}) - h_{2\bar{G}'} (\hat{e}_{1\bar{G}'} \cdot \hat{e}_{2\bar{G}}) \end{aligned} \quad (\text{B.12})$$

Then, we obtain successively:

$$\begin{aligned} (\alpha \hat{e}_{1\bar{G}} + \beta \hat{e}_{2\bar{G}}) \times (\bar{k} + \bar{G}) &= |\bar{k} + \bar{G}| (-\alpha \hat{e}_{2\bar{G}} + \beta \hat{e}_{1\bar{G}}) \\ [(\bar{k} + \bar{G}') \times \bar{h}_{\bar{G}'}] \times (\bar{k} + \bar{G}) &= |\bar{k} + \bar{G}'| |\bar{k} + \bar{G}| \left\{ \hat{e}_{1\bar{G}} [h_{1\bar{G}'} (\hat{e}_{2\bar{G}'} \cdot \hat{e}_{2\bar{G}}) - h_{2\bar{G}'} (\hat{e}_{1\bar{G}'} \cdot \hat{e}_{2\bar{G}})] + \right. \\ &\quad \left. + \hat{e}_{2\bar{G}} [-h_{1\bar{G}'} (\hat{e}_{2\bar{G}'} \cdot \hat{e}_{1\bar{G}}) + h_{2\bar{G}'} (\hat{e}_{1\bar{G}'} \cdot \hat{e}_{1\bar{G}})] \right\} \\ \sum_{\bar{G}'} |\bar{k} + \bar{G}'| |\bar{k} + \bar{G}| \varepsilon^{-1} (\bar{G} - \bar{G}') &\begin{bmatrix} \hat{e}_{2\bar{G}} \cdot \hat{e}_{2\bar{G}'} & -\hat{e}_{2\bar{G}} \cdot \hat{e}_{1\bar{G}'} \\ -\hat{e}_{1\bar{G}} \cdot \hat{e}_{2\bar{G}'} & \hat{e}_{1\bar{G}} \cdot \hat{e}_{1\bar{G}'} \end{bmatrix} \begin{bmatrix} h_{1\bar{G}'} \\ h_{2\bar{G}'} \end{bmatrix} = \left(\frac{\omega}{c}\right)^2 \begin{bmatrix} h_{1\bar{G}} \\ h_{2\bar{G}} \end{bmatrix} \end{aligned} \quad (\text{B.13})$$

Equation (B.13) is the eigenvalue formulation of the PWEM and can be written in a matrix form:

$$\llbracket M \rrbracket [h] = \left(\frac{\omega}{c}\right)^2 [h]$$

where $\llbracket M \rrbracket$ is a $(2N \times 2N)$ matrix obtained by assembling 4 block matrices with dimensions $(N \times N)$ and $[h]$ is a column vector containing the Fourier amplitudes of \vec{h} -field. The total number of plane waves is $N = N_1 N_2 N_3$, where N_j is the number of plane waves along axis 'j'.

Appendix C Example of script used in simulations with MPB program

```

; Compute band structure for a line-defect in a hexagon-type PCS
; Hexagonal holes can have an arbitrary rotation angle
; Calculation is 3D, combining 2 supercells (lateral and vertical)
; The line defect has a variable width
; Various parameters defined with 'define-param' are
; settable from the command-line (with mpb <param>=<value>):

(define-param eps 11.56)           ; dielectric constant of silicon
(define-param loweps 2.1)         ; dielectric constant of the substrate
(define-param r 0.48)            ; outer radius of hexagon
(define-param alpha 21)          ; rotation angle of the hexagon (deg)
(define-param w 0.68)            ; half-width of line defect
(define-param h1 0.6)            ; thickness of the slab core
(define-param m 2)
(define-param supercell-y (+ (* 2 w) (* m (sqrt 3)))) ; lateral supercell
(define-param supercell-z 4)     ; vertical supercell

(define h2 (* 0.5 (- supercell-z h1))) ; height of cladding
(define c2 (* 0.5 (+ h1 h2)))        ; center of the cladding
(define pi (* 4 (atan 1)))          ; pi= 3.14159...
(define x (* pi (/ alpha 180)))    ; rotation angle of the hexagon (rad)

; 3D rectangular computational domain
(set! geometry-lattice (make lattice (size 1 supercell-y supercell-z)))

(set! default-material air)
(set! geometry
  (list (make block (material (make dielectric (epsilon loweps)))
                    (center 0 0 c2)
                    (size infinity infinity h2))
        (make block (material (make dielectric (epsilon eps)))
                    (center 0) (size infinity infinity h1))))

; the following function constructs a hexagon by overlapping 3 rect. Blocks
(do ((l 0 (+ l 1))) ((= l 3) geometry)
  (set! geometry (append geometry
    (list
      (make block (material air)

```

Example of script used in simulations with MPB program

```
(center (vector3 0 (* -1 (+ (/ (sqrt 3) 2) w)) 0))
(size (* r (sqrt 3)) r supercell-z)
(e1 (* (cos (+ x (* 1 (/ pi 3)))) (* -1 (sin (+ x (* 1 (/ pi 3)))))) 0)
(e2 (* (sin (+ x (* 1 (/ pi 3)))) (* (cos (+ x (* 1 (/ pi 3)))))) 0)
(e3 0 0 1))

(list
  (make block (material air)
    (center (vector3 0 (* (+ (/ (sqrt 3) 2) w)) 0))
    (size (* r (sqrt 3)) r supercell-z)
    (e1 (* (cos (+ x (* 1 (/ pi 3)))) (* -1 (sin (+ x (* 1 (/ pi 3)))))) 0)
    (e2 (* (sin (+ x (* 1 (/ pi 3)))) (* (cos (+ x (* 1 (/ pi 3)))))) 0)
    (e3 0 0 1))))))

(set! geometry (geometric-objects-duplicates (vector3 0.5 (/ (sqrt 3) 2) 0) -1 1
  geometry))

(define Gamma (vector3 0 0 0))
(define K' (lattice->reciprocal (vector3 0.5 0 0))) ; edge of Brillouin zone.
(set! k-points (interpolate 8 (list Gamma K')))
(set-param! resolution 16)

; the original bands are "folded" supercell-y times
; to get to the defect modes we have to consider this folding
(define-param extra-bands 5)
(set! num-bands (* (ceiling supercell-y) extra-bands))

(begin-time
  "total time for both odd and even bands: "
  (run-zodd
    (output-at-kpoint K' output-hpwr))
  (run-zeven
    (output-at-kpoint K' output-dpwr)))
```

Appendix D Calculation of the dose absorbed in photoresist during the LIL process

The layer stack with relevant parameters for the exposure in the LIL process is shown in Figure D.1

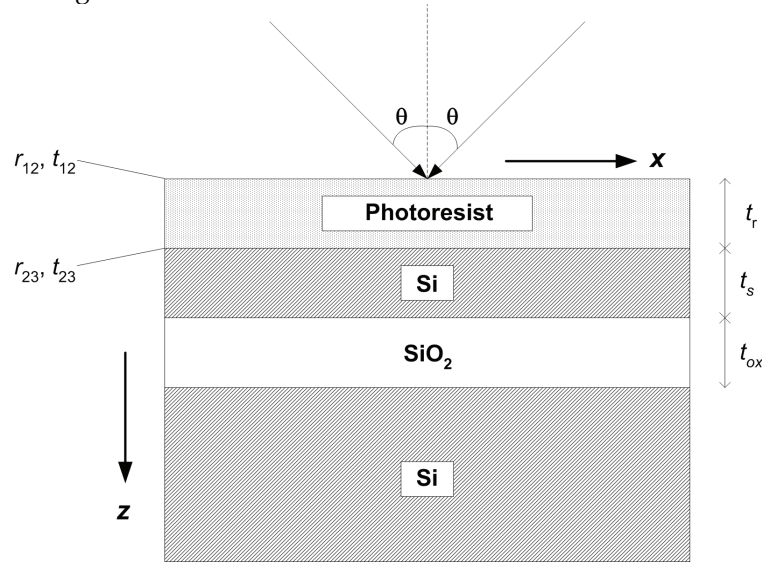


Figure D.1 Cross-section view of the layer stack used in our LIL process; r_{12}, t_{12} = Fresnel coefficients at air-resist interface; r_{23}, t_{23} = Fresnel coefficients at resist-multilayer (Si-SiO₂-Si) interface

The Fresnel coefficients depend on polarization (TE/TM) for oblique incidence. For calculating the multilayer properties we can apply the transfer or scattering matrix formalism.

For the second exposure the incidence angle remains the same (because we want the same period 'd'). The substrate is rotated; this is equivalent to a rotation of coordinate system with respect to the first exposure:

$$x' = x \cos \alpha + y \sin \alpha \quad (D.1)$$

where α is the rotation angle of the substrate between exposures.

The wave-vector of the incident wave (which is coming from air) can be split into two components, parallel and perpendicular, respectively, to the planar interface:

$$\begin{aligned} k_{||} &= k_x = k_0 \sin \theta \\ k_{\perp air} &= k_0 \cos \theta \end{aligned} \quad (D.2)$$

The tangential component $k_{||}$ is conserved and remains constant in all layers. The normal component changes its magnitude in each different layer according to:

$$k_{\perp} = k_0 \sqrt{\varepsilon_r - \sin^2 \theta} \quad (D.3)$$

where ε_r is the relative dielectric permittivity which in general can be complex. For example, photoresist has a relative dielectric permittivity:

$$\varepsilon_{rf} = (n_f + ik_f)^2$$

With n_f and k_f being the refractive index and extinction coefficient, respectively.

By inserting ε_{rf} in (D.3) one can see that k_{\perp} has an imaginary part in photoresist:

$$k_{\perp} = k'_{\perp} + ik''_{\perp} \quad (D.4)$$

By convention the imaginary part is taken as positive root, so that the wave $\exp(ik_{\perp}z) = \exp(-k''_{\perp}z)\exp(ik'_{\perp}z)$ is attenuated while propagating in the $z>0$ direction (physical solution).

The total field inside the photoresist layer can be described as a superposition of two waves propagating in opposite directions:

$$E_T = E_D e^{ik_{\perp}z} + E_U e^{-ik_{\perp}z} \quad (D.5)$$

where subscripts D and U stand for 'down' and 'up' respectively (in Figure D.1 'down' is in the $z>0$ direction).

The expression (D.5) has been used in an implementation of the matrix formalism for calculating the field distribution in a multilayer structure.

The irradiance in photoresist has a 3D distribution

$$I(x, y, z) = I_0 \cos \theta f_1(x, y) f_2(z) \quad (D.6)$$

where I_0 [Wm^{-2}] is the irradiance of the exposure beam in air for normal incidence, θ the angle of incidence, f_1 and f_2 are dimensionless periodic distribution functions, with $f_1(x, y)$ the periodic effective in-plane distribution due to the cumulative effect (sum) of the two exposures, and $f_2(z)$ the vertical distribution due to interfering reflections.

The in-plane distribution is given by the incoherent superposition of the two successive exposures $f_1(x, y) = f_1^1(x) + f_1^2(x, y)$, where $f_1^1(x)$ and $f_1^2(x, y)$ have the following expressions:

$$\begin{aligned} f_1^1(x) &= \left| \exp(ik_{||}x) + \exp(-ik_{||}x) \right|^2 = 4 \cos^2(k_{||}x) \\ f_1^2(x, y) &= 4 \cos^2(x \cos \alpha + y \sin \alpha) \end{aligned} \quad (D.7)$$

The vertical irradiance distribution is due to interference between multiple reflected waves inside the photoresist (which is seen as an asymmetric Fabry-Perot etalon, bounded by air on one side and by the multilayer stack on the other side):

$$f_2(z) = \rho \left| \exp(ik_{\perp}z) + r_{23} \exp(2ik_{\perp}t_r) \exp(-ik_{\perp}z) \right|^2$$

$$\rho = \left| \frac{t_{12}}{1 + r_{12}r_{23} \exp(2ik_{\perp}t_r)} \right|^2 \quad (\text{D.8})$$

The mean electromagnetic energy absorbed per unit volume per second in photoresist is:

$$Q = \frac{1}{2} \sigma_f |E|^2 \quad (\text{D.9})$$

where σ_f is the equivalent conductivity associated with absorption in photoresist:

$$\text{Im}(\varepsilon_f) = 2\varepsilon_0 n_f k_f = \frac{\sigma_f}{\omega} \Rightarrow \sigma_f = 2\omega \varepsilon_0 n_f k_f \quad (\text{D.10})$$

On the other hand, the irradiance in air of a normally incident plane wave is:

$$I = \left\langle \vec{S} \right\rangle = \frac{|E|^2}{2Z_0} \quad (\text{D.11})$$

where $Z_0 = \sqrt{\mu_0/\varepsilon_0}$ is the wave impedance of free space.

By inserting (D.11) and (D.10) in (D.9), the expression for the mean electromagnetic energy absorbed per unit volume per second in photoresist becomes:

$$Q = 2k_0 n_f k_f I \quad (\text{D.12})$$

The recorded dose is obtained by integrating the absorbed energy in time:

$$D = 2k_0 n_f \int_0^{t_{\text{ex}}} I(t) k_f(t) dt \quad (\text{D.13})$$

where t_{ex} is the exposure time.

In (D.13) the extinction coefficient is time-dependent, due to the 'bleaching' effect. The vertical distribution of the irradiance is time-dependent too, because it is a function of the extinction coefficient. The irradiance can also show fluctuations during the exposure time, but these are neglected here.

Appendix E Fabrication processes

□ LIL process 1

- ✓ Resist: Olin 907/12 diluted with EEP (Ethyl 3-ethoxypropionate) and MMP (Methyl 3-methoxypropionate) EEP: MMP: resist = 20% : 30% : 50%
- ✓ Spin-coat ARC (Brewer Science XHRi-11): 30s at 4000rot/min with 400rot/min² acceleration
- ✓ Bake: 4min. at 120° (hotplate)
- ✓ Spin-coat resist: 30s at 4000rot/min with 400rot/min² acceleration
- ✓ Soft bake: 30s at 95° (hotplate)
- ✓ Expose: $\lambda_0=364.8\text{nm}$, $I=89\mu\text{W}/\text{cm}^2$, 110s
- ✓ Develop: 10s in fresh OPD 4262
- ✓ Evaporate Cr: BAK 600, 15min (rate= $2\text{\AA}/\text{s}$)
- ✓ Lift-off: acetone beaker, ultrasonic bath, 30min.
- ✓ Etch ARC: Etske, $P=25\text{W}$, $p=7\text{mTorr}$, $T=10^\circ$, $\text{O}_2=7\text{sccm}$, 2min.
- ✓ Etch Si: Etske, $P=75\text{W}$, $p=10\text{mTorr}$, $T=10^\circ$, $\text{CHF}_3/\text{O}_2=25/5\text{sccm}$, rate= $37\text{nm}/\text{min}$
- ✓ Etch Cr: standard solution (HClO_4 60% 10ml, $\text{Ce}(\text{NH}_4)_2(\text{NO}_3)_6$ 33g, DI water 100ml), rate= $100\text{nm}/\text{min}$

□ LIL process 2

- ✓ Sputter Cr: Sputterke, $P=200\text{W}$, 3min. , rate= $10\text{nm}/\text{min}$
- ✓ Spin-coat resist (Clariant Ti-09XR): 30s at 4000rot/min
- ✓ Expose: $\lambda_0=266\text{nm}$, $I=200\mu\text{W}/\text{cm}^2$, 60s
- ✓ Image reversal bake: 60s at 135° (very critical)
- ✓ Flood exposure: Karl-Süss aligner, 40-80mJ (not critical)
- ✓ Develop: AZ-726MIF, 50s
- ✓ Etch ARC: Etske, $P=25\text{W}$, $p=7\text{mTorr}$, $T=10^\circ$, $\text{O}_2=7\text{sccm}$, 2min.

- ✓ Etch Cr: standard solution diluted with DI water (1:3), rate=25nm/min

□ **FIB process A**

- ✓ Sputter Cr: Sputterke, P=200W, 8min., rate=10nm/min
- ✓ Spin-coat resist (Olin 907/17): 30s at 4000rot/min
- ✓ Soft bake: 60s at 95° (hotplate)
- ✓ Expose: Karl-Süss aligner, mask broad waveguides, hard contact, 5.3s (timer)
- ✓ Post bake: 60s at 120° (hotplate)
- ✓ Develop: beaker 1=30s + beaker 2=18s
- ✓ Etch Cr: standard solution, 50s
- ✓ Strip resist: Karl-Süss aligner, 'lamp test', 1min, develop 1min.
- ✓ Etch Si: Etske, clean chamber, styros electrode, P=75W, p=100mTorr, T=10°, SF₆/CHF₃/O₂=30/10/12 sccm, 450nm/min
- ✓ FIB etching: Cr, 7-9min. at 70pA, 5000x
- ✓ Etch Si: same as previous
- ✓ Etch SiO₂: Etske, styros electrode, P=100W, p=10mTorr, T=10°, CHF₃/O₂=25/5 sccm, 60nm/min

□ **FIB process B**

- ✓ Standard lithography (spin-coat resist, soft bake, expose, post bake, develop): same as in FIB process A, mask 1 with broad waveguides
- ✓ Etch Si: same as FIB process A
- ✓ Standard lithography: same as previous, mask 2 with etch windows, align with respect to waveguides
- ✓ Etch SiO₂: BHF, rate=65nm/min
- ✓ FIB etching: free standing Si membrane, same FIB parameters as in process A

References

- [Adibi 2000] Adibi, A., Lee, R. K., Xu, Y., Yariv, A. and Scherer, A., "Design of photonic crystal optical waveguides with singlemode propagation in the photonic bandgap", *Electronics Letters*, **36**, pp. 1376-1378, 2000
- [Adibi 2001a] Adibi, A., Xu, Y., Lee, R. K., Loncar, M., Yariv, A. and Scherer, A., "Role of distributed Bragg reflection in photonic-crystal optical waveguides", *Physical Review B*, **64**, art. no. 041102, 2001
- [Adibi 2001b] Adibi, A., Xu, Y., Lee, R. K., Yariv, A. and Scherer, A., "Guiding mechanisms in dielectric-core photonic-crystal optical waveguides", *Physical Review B*, **64**, art. no.033308, 2001
- [Agió 2001] Agió, M. and Soukoulis, C. M., "Ministop bands in single-defect photonic crystal waveguides", *Physical Review E*, **64**, art. no. 055603, 2001
- [Anderson 1997] Anderson, C. M. and Giapis, K. P., "Symmetry reduction in group 4mm photonic crystals", *Physical Review B*, **56**, pp. 7313-7320, 1997
- [Astratov 1999] Astratov, V. N., Whittaker, D. M., Culshaw, I. S., Stevenson, R. M., Skolnick, M. S., Krauss, T. and De La Rue, R., "Photonic band-structure effects in the reflectivity of periodically patterned waveguides", *Physical Review B*, **60**, pp. R16255-R16258, 1999
- [Avary 2002] Avary, K., Reithmaier, J. P., Klopff, F., Happ, T., Kamp, M. and Forchel, A., "Deeply etched two-dimensional photonic crystals fabricated on GaAs/AlGaAs slab waveguides by using chemically assisted ion beam etching", *Microelectronic Engineering*, **61-2**, pp. 875-880, 2002
- [Baba 2002] Baba, T. and Nakamura, M., "Photonic crystal light deflection devices using the superprism effect", *IEEE Journal of Quantum Electronics*, **38**, pp. 909-914, 2002
- [Benisty 1996] Benisty, H., "Modal analysis of optical guides with two-dimensional photonic band-gap boundaries", *J. Appl. Phys.*, **79**, pp. 7483-7492, 1996

References

- [Benisty 2000] Benisty, H., Labilloy, D., Weisbuch, C., Smith, C. J. M., Krauss, T. F., Cassagne, D., Beraud, A. and Jouanin, C., "Radiation losses of waveguide-based two-dimensional photonic crystals: Positive role of the substrate", *Applied Physics Letters*, **76**, pp. 532-534, 2000
- [Benisty 2002] Benisty, H., Olivier, S., Weisbuch, C., Agio, M., Kafesaki, M., Soukoulis, C. M., Qiu, M., Swillo, M., Karlsson, A., Jaskorzynska, B., Talneau, A., Moosburger, J., Kamp, M., Forchel, A., Ferrini, R., Houdre, R. and Oesterle, U., "Models and measurements for the transmission of submicron-width waveguide bends defined in two-dimensional photonic crystals", *IEEE Journal of Quantum Electronics*, **38**, pp. 770-785, 2002
- [Bérenger 1994] Bérenger, J. P., "A perfectly matched layer for the absorption of electromagnetic waves", *J. Comp. Phys.*, **114**, pp. 185-200, 1994
- [Berger 1997] Berger, V., GauthierLafaye, O. and Costard, E., "Photonic band gaps and holography", *Journal of Applied Physics*, **82**, pp. 60-64, 1997
- [Bhat 2001] Bhat, N. A. R. and Sipe, J. E., "Optical pulse propagation in nonlinear photonic crystals", *Physical Review E*, **64**, art. no. 056604, 2001
- [Bienstman] CAvity Modeling FRamework - CAMFR,
<http://camfr.sourceforge.net>
- [Bienstman 2001] Bienstman, P. and Baets, R., "Optical modelling of photonic crystals and VCSELs using eigenmode expansion and perfectly matched layers", *Optical and Quantum Electronics*, **33**, pp. 327-341, 2001
- [Bienstman 2002] Bienstman, P. and Baets, R., "Advanced boundary conditions for eigenmode expansion models", *Optical and Quantum Electronics*, **34**, pp. 523-540, 2002
- [Bogaerts 2002a] Bogaerts, W., Bienstman, P., Taillaert, D., Baets, R. and De Zutter, D., "Out-of-plane scattering in 1-D photonic crystal slabs", *Optical and Quantum Electronics*, **34**, pp. 195-203, 2002
- [Bogaerts 2002b] Bogaerts, W., Wiaux, V., Taillaert, D., Beckx, S., Luyssaert, B., Bienstman, P. and Baets, R., "Fabrication of photonic crystals in silicon-on-insulator using 248-nm deep UV lithography", *IEEE Journal of Selected Topics in Quantum Electronics*, **8**, pp. 928-934, 2002
- [Bogaerts 2003] Bogaerts, W., Bienstman, P. and Baets, R., "Scattering at sidewall roughness in photonic crystal slabs", *Optics Letters*, **28**, pp. 689-691, 2003

-
- [Boscolo 2002] Boscolo, S., Midrio, M. and Krauss, T. F., "Y junctions in photonic crystal channel waveguides: high transmission and impedance matching", *Optics Letters*, **27**, pp. 1001-1003, 2002
- [Bostan 2002a] Bostan, C. G. and de Ridder, R. M., "Design of photonic crystal slab structures with absolute gaps in guided modes", *Journal of Optoelectronics and Advanced Materials*, **4**, pp. 921-928, 2002
- [Bostan 2002b] Bostan, C. G. and de Ridder, R. M., "Modeling of 2D photonic crystals using the layer-by-layer method and 'fast Fourier factorization' rules", *Advanced Topics in Optoelectronics, Microelectronics and Nanotechnologies*, Bucharest, Romania, edited by O. Iancu, A. Manea and D. Cojoc, Proceedings of SPIE **5227**, pp. 205-212, 2002
- [Bostan 2002c] Bostan, C. G., de Ridder, R. M., van Dorssen, I., van Wolferen, H. A. G. M., Kuipers, L. and van Hulst, N. F., "Modeling and Process Design for Laser Interference Lithography Used in Fabricating Two-Dimensional Periodic Structures", *ICTON-2002 Conference Proceedings*, Warsaw, Poland, edited by M. Marciniak and M. Jaworski, pp. 61, 2002
- [Bostan 2004a] Bostan, C. G., de Ridder, R. M., Gadgil, V. J., Kelderman, H., Kuipers, L. and Driessen, A., "Design and fabrication of line-defect waveguides in hexagon-type SOI photonic crystal slabs", *Photonic Crystal Materials and Nanostructures-Photonics Europe 2004*, Strasbourg - France, edited by R. De La Rue, P. Viktorovitch, C. M. Sotomayor-Torres and M. Midrio, SPIE **5450**, 2004
- [Bostan 2004b] Bostan, C. G., de Ridder, R. M., Kelderman, H. and Driessen, A., "Waveguides, Bends and Y-junctions with Improved transmission and Bandwidth in Hexagon-Type SOI Photonic Crystal Slabs", *ATOM-N 2004*, Bucharest, Romania, 2004
- [Botten 2001] Botten, L. C., Nicorovici, N. A., McPhedran, R. C., de Sterke, C. M. and Asatryan, A. A., "Photonic band structure calculations using scattering matrices", *Physical Review E*, **64**, art. no. 046603, 2001
- [Busch 1998] Busch, K. and John, S., "Photonic band gap formation in certain self-organizing systems", *Physical Review E*, **58**, pp. 3896-3908, 1998
- [Busch 2003] Busch, K., Mingaleev, S. F., Garcia-Martin, A., Schillinger, M. and Hermann, D., "The Wannier function approach to photonic crystal circuits", *Journal of Physics-Condensed Matter*, **15**, pp. R1233-R1256, 2003
- [Campbell 2000] Campbell, M., Sharp, D. N., Harrison, M. T., Denning, R. G. and Turberfield, A. J., "Fabrication of photonic crystals for the visible spectrum by holographic lithography", *Nature*, **404**, pp. 53-56, 2000

References

- [Cassagne 1996] Cassagne, D., Jouanin, C. and Bertho, D., "Hexagonal photonic-band-gap structures", *Physical Review B*, **53**, pp. 7134-7142, 1996
- [Chelnokov 1999] Chelnokov, A., Rowson, S., Lourtioz, J. M., Berger, V. and Courtois, J.-Y., "An optical drill for the fabrication of photonic crystals", *Journal of Optics A-Pure and Applied Optics*, **1**, pp. L3-L6, 1999
- [Chelnokov 2000] Chelnokov, A., Wang, K., Rowson, S., Garoche, P. and Lourtioz, J. M., "Near-infrared Yablonovite-like photonic crystals by focused-ion-beam etching of macroporous silicon", *Applied Physics Letters*, **77**, pp. 2943-2945, 2000
- [Chutinan 2002] Chutinan, A., Okano, M. and Noda, S., "Wider bandwidth with high transmission through waveguide bends in two-dimensional photonic crystal slabs", *Applied Physics Letters*, **80**, pp. 1698-1700, 2002
- [Comsol] FEMLAB, <http://www.femlab.com>
- [Dansas 1998] Dansas, P. and Paraire, N., "Fast modeling of photonic bandgap structures by use of a diffraction-grating approach", *J. Opt. Soc. Am. A*, **15**, pp. 1586-1598, 1998
- [Desieres 2002] Desieres, Y., Benyattou, T., Orobitchouk, R., Morand, A., Benech, P., Grillet, C., Seassal, C., Letartre, X., Rojo-Romeo, P. and Viktorovitch, P., "Propagation losses of the fundamental mode in a single line-defect photonic crystal waveguide on an InP membrane", *Journal of Applied Physics*, **92**, pp. 2227-2234, 2002
- [Divliansky 2003] Divliansky, I., Mayer, T. S., Holliday, K. S. and Crespi, V. H., "Fabrication of three-dimensional polymer photonic crystal structures using single diffraction element interference lithography", *Applied Physics Letters*, **82**, pp. 1667-1669, 2003
- [Fan 2002] Fan, S. H. and Joannopoulos, J. D., "Analysis of guided resonances in photonic crystal slabs", *Physical Review B*, **65**, pp. 235112, 2002
- [Fernandez 1997] Fernandez, A., Decker, J. Y., Herman, S. M., Phillion, D. W., Sweeney, D. W. and Perry, M. D., "Methods for fabricating arrays of holes using interference lithography", *Journal of Vacuum Science & Technology B*, **15**, pp. 2439-2443, 1997
- [Ferrini 2003] Ferrini, R., Houdre, R., Benisty, H., Qiu, M. and Moosburger, J., "Radiation losses in planar photonic crystals: two-dimensional representation of hole depth and shape by an imaginary dielectric constant", *J. Opt. Soc. Am. B*, **20**, pp. 469-478, 2003

-
- [Flagello 1997] Flagello, D. G. and Milster, T. D., "High-numerical-aperture effects in photoresist", *Applied Optics*, **36**, pp. 8944-8951, 1997
- [Fu 2001] Fu, Y. and Bryan, N. K. A., "Experimental study of microcylindrical lenses fabricated using focused-ion-beam technology", *Journal of Vacuum Science & Technology B*, **19**, pp. 1259-1263, 2001
- [Gadgil 2004] Gadgil, V. J. and Morrissey, F. *Applications of Focused Ion Beam in Nanotechnology*, in *Encyclopedia of Nanoscience and Nanotechnology*, edited by H. S. Nalwa, American Scientific Publishers, 2004
- [Halevi 1999] Halevi, P., Krokhin, A. A. and Arriaga, J., "Photonic crystal optics and homogenization of 2D periodic composites", *Physical Review Letters*, **82**, pp. 719-722, 1999
- [Hielt 2002] Hielt, B. P., *Photonic Crystal Modelling using Finite Element Analysis*, PhD Thesis, University of Southampton, Faculty of Engineering and Applied Science, 2002
- [Ho 1990] Ho, K. M., Chan, C. T. and Soukoulis, C. M., "Existence of a photonic gap in periodic dielectric structures", *Physical Review Letters*, **65**, pp. 3152-3155, 1990
- [Ito 1997] Ito, T., Ishikawa, H., Egawa, T., Jimbo, T. and Umeno, M., "Fabrication of flat end mirror etched by focused ion beam for GaN-based blue-green laser diode", *Japanese Journal of Applied Physics Part 1*, **36**, pp. 7710-7711, 1997
- [Jamois 2002] Jamois, C., Wehrspohn, R. B., Schilling, J., Muller, F., Hillebrand, R. and Hergert, W., "Silicon-based photonic crystal slabs: Two concepts", *IEEE Journal of Quantum Electronics*, **38**, pp. 805-810, 2002
- [Jansen 1995] Jansen, H., de Boer, M., Burger, J., Legtenberg, R. and Elwenspoek, M., "The Black Silicon Method 2. The Effect of Mask Material and Loading on the Reactive Ion Etching of Deep Silicon Trenches", *Microelectronic Engineering*, **27**, pp. 475-480, 1995
- [Jansen 1996] Jansen, H., Gardeniers, H., deBoer, M., Elwenspoek, M. and Fluitman, J., "A survey on the reactive ion etching of silicon in microtechnology", *Journal of Micromechanics and Microengineering*, **6**, pp. 14-28, 1996
- [Jensen 2004] Jensen, J. S. and Sigmund, O., "Systematic design of photonic crystal structures using topology optimization: Low-loss waveguide bends", *Applied Physics Letters*, **84**, pp. 2022-2024, 2004

References

-
- [Joannopoulos 1995] Joannopoulos, J. D., Meade, R. D. and Winn, J. N., *Photonic crystals: Molding the flow of light*, Princeton University Press, 1995
- [Johnson] MIT Photonic Bands, <http://ab-initio.mit.edu/mpb>
- [Johnson 1999] Johnson, S. G., Fan, S. H., Villeneuve, P. R., Joannopoulos, J. D. and Kolodziejski, L. A., "Guided modes in photonic crystal slabs", *Physical Review B*, **60**, pp. 5751-5758, 1999
- [Johnson 2001] Johnson, S. G. and Joannopoulos, J., "Block-iterative frequency-domain methods for Maxwell's equations in a planewave basis", *Optics Express*, **8**, pp. 173-190, 2001
- [Johnson 2002] Johnson, S. G., Ibanescu, M., Skorobogaty, M. A., Weisberg, O., Joannopoulos, J. and Fink, Y., "Perturbation theory for Maxwell's equations with shifting material boundaries", *Physical Review E*, **65**, art.no. 066611, 2002
- [Johnson 2003] Johnson, S. G. and Joannopoulos, J., *Introduction to photonic crystals: Bloch's theorem, band diagrams and gaps*, MIT, 2003
- [Krauss 1994] Krauss, T., Song, Y. P., Thoms, S., Wilkinson, C. D. W. and De La Rue, R., "Fabrication of 2-D photonic bandgap structures in GaAs/AlGaAs", *Electronics Letters*, **30**, pp. 1444-1446, 1994
- [Lalanne 1998] Lalanne, P., "Effective properties and band structures of lamellar subwavelength crystals: Plane-wave method revisited", *Physical Review B*, **58**, pp. 9801-9807, 1998
- [Lalanne 2000] Lalanne, P. and Silberstein, E., "Fourier-modal methods applied to waveguide computational problems", *Optics Letters*, **25**, pp. 1092-1094, 2000
- [Lalanne 2001] Lalanne, P. and Benisty, H., "Out-of-plane losses of two-dimensional photonic crystals waveguides: Electromagnetic analysis", *Journal of Applied Physics*, **89**, pp. 1512-1514, 2001
- [Lau 2002] Lau, W. T. and Fan, S. H., "Creating large bandwidth line defects by embedding dielectric waveguides into photonic crystal slabs", *Applied Physics Letters*, **81**, pp. 3915-3917, 2002
- [Leung 1990a] Leung, K. M. and Liu, Y. F., "Photon band structures: The plane wave method", *Physical Review B*, **41**, pp. 10188-10190, 1990

-
- [Leung 1990b] Leung, K. M. and Liu, Y. F., "Full vector wave calculation of photonic band structures in face-centered-cubic dielectric media", *Physical Review Letters*, **65**, pp. 2646-2649, 1990
- [Li 2003a] Li, H.-W., Kang, D. J., Blamire, M. G. and Huck, W. T. S., "Focused ion beam fabrication of silicon print masters", *Nanotechnology*, **14**, pp. 220-223, 2003
- [Li 1996] Li, L., "Use of Fourier series in the analysis of discontinuous periodic structures", *J. Opt. Soc. Am. A*, **13**, pp. 1870-1876, 1996
- [Li 2003b] Li, Z. Y. and Ho, K. M., "Light propagation through photonic crystal waveguide bends by eigenmode examinations", *Physical Review B*, **68**, art. no. 045201, 2003
- [Loncar 2000] Loncar, M., Doll, T., Vuckovic, J. and Scherer, A., "Design and fabrication of silicon photonic crystal optical waveguides", *Journal of Lightwave Technology*, **18**, pp. 1402-1411, 2000
- [Loncar 2001] Loncar, M., Vuckovic, J. and Scherer, A., "Methods for controlling positions of guided modes of photonic-crystal waveguides", *Journal of the Optical Society of America B-Optical Physics*, **18**, pp. 1362-1368, 2001
- [Luo 2002] Luo, C., Johnson, S. G., Joannopoulos, J. D. and Pendry, J. B., "All-angle negative refraction without negative effective index", *Physical Review B*, **65**, pp. 201104, 2002
- [Maystre 1994] Maystre, D., "Electromagnetic study of photonic band gaps", *Pure Appl. Opt.*, **3**, pp. 975-993, 1994
- [Meade 1993] Meade, R. D., Rappe, A. M., Brommer, K. D. and Joannopoulos, J., "Accurate theoretical analysis of photonic band-gap materials", *Physical Review B*, **48**, pp. 8434-8437, 1993
- [Meade 1994] Meade, R. D., Devenyi, A., Joannopoulos, J., Alerhand, O. L., Smith, D. A. and Kash, K., "Novel applications of photonic band gap materials: Low-loss bends and high Q cavities", *Journal of Applied Physics*, **75**, pp. 4753-4755, 1994
- [Mekis 1996] Mekis, A., Chen, J. C., Kurland, I., Fan, S. H., Villeneuve, P. R. and Joannopoulos, J. D., "High transmission through sharp bends in photonic crystal waveguides", *Physical Review Letters*, **77**, pp. 3787-3790, 1996

References

- [Miyai 2001] Miyai, E. and Sakoda, K., "Quality factor for localized defect modes in a photonic crystal slab upon a low-index dielectric substrate", *Optics Letters*, **26**, pp. 740-742, 2001
- [Moll 2003] Moll, N. and Bona, G. L., "Comparison of three-dimensional photonic crystal slab waveguides with two-dimensional photonic crystal waveguides: Efficient butt coupling into these photonic crystal waveguides", *Journal of Applied Physics*, **93**, pp. 4986-4991, 2003
- [Noda 2001] Noda, S., Yokoyama, M., Imada, M., Chutinan, A. and Mochizuki, M., "Polarization mode control of two-dimensional photonic crystal laser by unit cell structure design", *Science*, **293**, pp. 1123-1125, 2001
- [Notomi 2001] Notomi, H., Shinya, A., Yamada, K., Takahashi, J., Takahashi, C. and Yokohama, I., "Singlemode transmission within photonic bandgap of width-varied single-line-defect photonic crystal waveguides on SOI substrates", *Electronics Letters*, **37**, pp. 293-295, 2001
- [Notomi 2002] Notomi, M., Shinya, A., Yamada, K., Takahashi, J., Takahashi, C. and Yokohama, I., "Structural tuning of guiding modes of line-defect waveguides of silicon-on-insulator photonic crystal slabs", *Ieee Journal of Quantum Electronics*, **38**, pp. 736-742, 2002
- [Ntakis 2004] Ntakis, I., Pottier, P. and De La Rue, R. M., "Optimization of transmission properties of two-dimensional photonic crystal channel waveguide bends through local lattice deformation", *Journal of Applied Physics*, **96**, pp. 12-18, 2004
- [Ochiai 2001] Ochiai, T. and Sakoda, K., "Nearly free-photon approximation for two-dimensional photonic crystal slabs", *Physical Review B*, **64**, art. no. 045108, 2001
- [Oehrlein 1990] Oehrlein, G. S. *Reactive Ion Etching*, in *Handbook of Plasma Processing Technology*, edited by S. M. Rossnagel, 1990
- [Ohfuti 1997] Ohfuti, Y., Fukutome, H. and Cho, K., "New method of photonic band calculation and its application", *J. of Luminescence*, **72-74**, pp. 867-868, 1997
- [Ohtaka 1996] Ohtaka, K. and Tanabe, Y., "Photonic band using vector spherical waves. 1. Various properties of Bloch electric fields and heavy photons", *Journal of the Physical Society of Japan*, **65**, pp. 2265-2275, 1996

-
- [Padjen 1994] Padjen, R., Gerard, J. M. and Marzin, J. Y., "Analysis of the filling pattern dependence of the photonic bandgap for two-dimensional systems", *Journal of Modern Optics*, **41**, pp. 295-310, 1994
- [Paul 2002] Paul, A. K., Dimri, A. K. and Bajpai, R. P., "Plasma etch models based on different plasma chemistry for micro-electro-mechanical-systems application", *Vacuum*, **68**, pp. 191-196, 2002
- [Pendry 1992] Pendry, J. B. and MacKinnon, A., "Calculation of photon dispersion relations", *Physical Review Letters*, **69**, pp. 2772-2775, 1992
- [Pendry 1996] Pendry, J. B., "Calculating photonic band structure", *J. Phys.: Condens. Matter*, **8**, pp. 1085-1108, 1996
- [Popov 2000] Popov, E. and Nevière, M., "Grating theory: new equations in Fourier space leading to fast converging results for TM polarization", *J. Opt. Soc. Am. A*, **17**, pp. 1773-1784, 2000
- [Popov 2002] Popov, E., Neviere, M., Gralak, B. and Tayeb, G., "Staircase approximation validity for arbitrary-shaped gratings", *J. Opt. Soc. Am. A*, **19**, pp. 33-42, 2002
- [Pottage 2001] Pottage, J. M., Silvestre, E. and Russell, P. S., "Vertical-cavity surface-emitting resonances in photonic crystal films", *J. Opt. Soc. Am. A*, **18**, pp. 442-447, 2001
- [Qiu 2001] Qiu, M., Azizi, K., Karlsson, A., Swillo, M. and Jaskorzynska, B., "Numerical studies of mode gaps and coupling efficiency for line-defect waveguides in two-dimensional photonic crystals", *Physical Review B*, **64**, art. no. 155113, 2001
- [Qiu 2002a] Qiu, M., "Band gap effects in asymmetric photonic crystal slabs", *Physical Review B*, **66**, art. no. 033103, 2002
- [Qiu 2002b] Qiu, M., "Effective index method for heterostructure-slab-waveguide-based two-dimensional photonic crystals", *Applied Physics Letters*, **81**, pp. 1163-1165, 2002
- [Reynolds] Translight,
<http://www.elec.gla.ac.uk/~areynolds/Software/SoftwareMain.htm>
- [Reyntjens 2001] Reyntjens, S. and Puers, R., "A review of focused ion beam applications in microsystem technology", *Journal of Micromechanics and Microengineering*, **11**, pp. 287-300, 2001
- [S.O.I.TEC] Silicon on Insulator technologies, <http://www.soitec.com>

References

- [Sakoda 1995] Sakoda, K., "Symmetry, degeneracy, and uncoupled modes in two-dimensional photonic lattices", *Physical Review B*, **52**, pp. 7982-7986, 1995
- [Sakoda 2001] Sakoda, K., *Optical properties of photonic crystals*, Springer Verlag, 2001
- [Sharkawy 2003] Sharkawy, A., Pustai, D., Shi, S. Y. and Prather, D. W., "High transmission through waveguide bends by use of polycrystalline photonic-crystal structures", *Optics Letters*, **28**, pp. 1197-1199, 2003
- [Shen 2002] Shen, L. F. and He, S. L., "Analysis for the convergence problem of the plane-wave expansion method for photonic crystals", *Journal of the Optical Society of America A-Optics Image Science and Vision*, **19**, pp. 1021-1024, 2002
- [Shen 2003] Shen, L. F., Ye, Z. and He, S., "Design of two-dimensional photonic crystals with large absolute band gaps using a genetic algorithm", *Physical Review B*, **68**, art. no. 035109, 2003
- [Shinya 2002] Shinya, A., Notomi, M., Yokohama, I., Takahashi, C., Takahashi, J. I. and Tamamura, T., "Two-dimensional Si photonic crystals on oxide using SOI substrate", *Optical and Quantum Electronics*, **34**, pp. 113-121, 2002
- [Sigalas 2003] Sigalas, M. M. and Chow, E., "Elliptical air hole waveguides in slab photonic crystals", *Journal of Applied Physics*, **93**, pp. 10125-10127, 2003
- [Sipe 2000] Sipe, J. E., "Vector k p approach for photonic band structures", *Physical Review E*, **62**, pp. 5672-5677, 2000
- [Søndergaard 2002a] Søndergaard, T., Arentoft, J. and Kristensen, M., "Theoretical analysis of finite-height semiconductor-on-insulator-based planar photonic crystal waveguides", *Journal of Lightwave Technology*, **20**, pp. 1619-1626, 2002
- [Søndergaard 2002b] Søndergaard, T. and Lavrinenko, A., "Large-bandwidth planar photonic crystal waveguides", *Optics Communications*, **203**, pp. 263-270, 2002
- [Sözüer 1992] Sözüer, H. S., Haus, J. W. and Inguva, R., "Photonic bands: convergence problems with the plane-wave method", *Physical Review B*, **45**, pp. 13962-13972, 1992
- [Suzuki 1995] Suzuki, T. and Yu, P. K. L., "Tunneling in photonic band structures", *J. Opt. Soc. Am. B*, **12**, pp. 804-820, 1995

-
- [Taflove 1995] Taflove, A., *Computational Electrodynamics – The Finite-Difference Time-Domain Method*, Artech House, 1995
- [Tan 2003] Tan, F. S., Klunder, D. J. W., Geuzebroek, D. H., Sengo, G., Kelderman, H., Hoekstra, H. J. W. M. and Driessen, A., "Characterization of vertically coupled waveguide-microring resonators by means of quantitative image analysis", *Journal of Nonlinear Optical Physics and Materials*, **12**, pp. 205-212, 2003
- [Tanaka 2003] Tanaka, Y., Asano, T., Akahane, Y., Song, B. S. and Noda, S., "Theoretical investigation of a two-dimensional photonic crystal slab with truncated cone air holes", *Applied Physics Letters*, **82**, pp. 1661-1663, 2003
- [Tijssen 2003] Tijssen, R., *Analysis of submicron periodic patterns fabricated by Laser Interference Lithography, for photonic crystal applications*, Master Thesis, University of Twente, Lightwave Devices Group, 2003
- [Tikhodeev 2002] Tikhodeev, S. G., Yablonskii, A. L., Muljarov, E. A., Gippius, N. A. and Ishihara, T., "Quasiguided modes and optical properties of photonic crystal slabs", *Physical Review B*, **66**, art. no. 045102, 2002
- [van Dorssen 2001] van Dorssen, I., *Fabrication of Submicron Photonic Crystal Structures in Silicon using Laser Interference Lithography*, Master Thesis, University of Twente, Lightwave Devices Group, 2001
- [Venkataraman 2003] Venkataraman, S., Murakowski, J., Adam, T. N., Kolodzey, J. and Prather, D. W., "Fabrication of high-fill-factor photonic crystal devices on silicon-on-insulator substrates", *Journal of Microlithography Microfabrication and Microsystems*, **2**, pp. 248-254, 2003
- [Villeneuve 1994] Villeneuve, P. R. and Piché, M., "Photonic bandgaps: what is the best numerical representation of periodic structures?" *Journal of Modern Optics*, **41**, pp. 241-256, 1994
- [Villeneuve 1996] Villeneuve, P. R., Fan, S. and Joannopoulos, J., "Microcavities in photonic crystals: Mode symmetry, tunability, and coupling efficiency", *Physical Review B*, **54**, pp. 7837-7842, 1996
- [Vogelaar 2001] Vogelaar, L., Nijdam, W., van Wolferen, H. A. G. M., de Ridder, R. M., Segerink, F. B., Fluck, E., Kuipers, L. and van Hulst, N. F., "Large area photonic crystal slabs for visible light with waveguiding defect structures: Fabrication with focused ion beam assisted laser interference lithography", *Advanced Materials*, **13**, pp. 1551-1554, 2001

References

- [Wang 2003] Wang, K., Filloux, P., Paraire, N., Cabarrocas, P. R. I. and Bulkin, P., "Two-dimensional photonic crystals by focused-ion-beam etching of multilayer membranes", *Journal of Vacuum Science & Technology B*, **21**, pp. 966-969, 2003
- [Wang 2001] Wang, R., Wang, X.-H., Gu, B.-Y. and Yan, G.-Z., "Effects of shapes and orientations of scatterers and lattice symmetries on the photonic band gap in two-dimensional photonic crystals", *J. Appl. Phys.*, **90**, pp. 4307-4313, 2001
- [Wang 1993] Wang, X., Zhang, X.-G., Yu, Q. and Harmon, B. N., "Multiple scattering theory for electromagnetic waves", *Physical Review B*, **47**, pp. 4161-4167, 1993
- [Whittaker 1999] Whittaker, D. M. and Culshaw, I. S., "Scattering-matrix treatment of patterned multilayer photonic structures", *Physical Review B*, **60**, pp. 2610-2618, 1999
- [Wu 2003] Wu, L., Mazilu, M., Gallet, J. F. and Krauss, T. F., "Square lattice photonic-crystal collimator", *Photonics and Nanostructures - Fundamentals and Applications*, **1**, pp. 31-36, 2003
- [Xu 2001] Xu, Y., Sun, H. B., Ye, J. Y., Matsuo, S. and Misawa, H., "Fabrication and direct transmission measurement of high-aspect-ratio two-dimensional silicon-based photonic crystal chips", *Journal of the Optical Society of America B-Optical Physics*, **18**, pp. 1084-1091, 2001
- [Yamada 2001] Yamada, K., Morita, H., Shinya, A. and Notomi, M., "Improved line-defect structures for photonic-crystal waveguides with high group velocity", *Optics Communications*, **198**, pp. 395-402, 2001
- [Yamada 2002] Yamada, K., Notomi, M., Shinya, A., Takahashi, C., Takahashi, J. and Morita, H., "Singlemode lightwave transmission in SOI-type photonic-crystal line-defect waveguides with phase-shifted holes", *Electronics Letters*, **38**, pp. 74-75, 2002
- [Yariv 1984] Yariv, A. and Yeh, P., *Optical Waves in Crystals*, Wiley, 1984
- [Yee 1966] Yee, K. S., "Numerical solution of initial boundary value problems involving Maxwell's equations in isotropic media", *IEEE Transactions on Antennas and Propagation*, **AP-14**, pp. 302-307, 1966

Acknowledgements

Here I would like to take the opportunity to thank the people who contributed directly or indirectly to this work. And I hope to not accidentally omit someone...So, a big "Thank You!" goes to:

- Prof. Alfred Driessen and Dr. ir. René de Ridder for the attention they have paid to the manuscript of my thesis and for the suggestions for improvement they have made. Many times René and I ended up discussing for a couple of hours (not only photonic crystal related matters...), after I was unexpectedly popping up into his office with a "brief question". Thanks René for translating the summary into Dutch.
- Dutch Technology Foundation (STW) and MESA+ for the financial support of this project.
- Prof. Kobus Kuipers for being so "contagiously" enthusiastic about photonic crystals and for teaching me very useful tips and tricks. Thanks Kobus for the idea of using direct FIB milling for fabricating photonic crystals.
- Prof. Paul Lambeck for his valuable ideas and his critical spirit expressed during the brief period of time he was involved in the photonic crystal project.
- Prof. Richard De La Rue (University of Glasgow) for pointing out an essential missing reference.
- All the members of my graduation committee for their willingness to examine this thesis.
- Henry Kelderman for all his help with mask design, lithography, dicing...and all the refreshing discussions we had...Henry, you are one of my true friends.
- Dr. Steven Johnson (MIT) for freely sharing the MPB program, for maintaining the discussion list and for kindly answering my questions.
- Dr. Vishwas Gadgil, Ferdi Meijer (Maser Engineering), Frans Segerink and Koen Klein-Koerkamp for their contributions to the FIB-related work.
- Anton Hollink and Henk van Wolferen for keeping my computer(s) alive and for technical assistance with the optical setups.
- Dr. Henri Jansen, Meint de Boer, Gabriel Sengo and Erwin Berenschot for advice on RIE.
- Robert Wijn, Meindert Dijkstra and Lucie Hilderink for advice on general cleanroom procedures.
- All the cleanroom staff for their expertise and for making MESA+ an excellent working environment.
- Mark Smithers and Bert Otter for taking some of the high-resolution SEM pictures presented in this thesis.

- My former students Inge van Dorssen, Paul Ubbink and Robin Tijssen for their work on photonic crystal fabrication.
- Arne Leinse, Edwin Klein and Douwe Geuzebroek for advice on measurement procedures.
- Ronald Dekker for sharing his measurement automation program.
- Joris van Lith for patiently answering my questions related to the PhD graduation procedure.
- Geert Altena for teaching me some basic Unix commands.
- Rita ter Weele, Simone Heideman and Ingrid Boers, the present and former secretaries of IOMS (LDG) group, for very good administrative support.
- My officemate and friend Mohamed Gamar Hussein for all the things we have shared during the past 4 years...
- Sami Musa, Freddy Tan and Henri Uranus for many pleasant and useful discussions (ranging from technology to cultural differences...).
- All the members of IOMS (students and staff) for all the “gezellige” moments (trips, coffee & cake breaks, “borrels”...)
- Prof. Susumu Noda (Kyoto University) for a very interesting discussion and for his very kind words.
- Dr. Mircea Modreanu (formerly at IMT Bucharest) for recommending me the University of Twente and Dr. Kerstin Wörhoff for directing my application to the photonic crystal project leader.
- All my former professors in engineering/physics/mathematics subjects for building the foundations I needed in my “struggle” with photonic crystals.
- Prof. Dan Dascălu, Florin Crăciunoiu and Viorel Avramescu (IMT Bucharest) for granting me permission for a temporary leave of more than 4 years to The Netherlands, to pursue this PhD.
- Dr. Wim Bogaerts (Ghent University-IMEC) for help with mask design in the PICCO project cooperation (the fabrication results are not presented here, though)
- All my Romanian friends that I met in The Netherlands, especially Diana, Violeta, Liviu and Oxana, Dela and Loredana, Aurelian, Victor, Octav, Sorin and Maria, Cristi. Thank you for all the nice moments.

A special “Thank You!” is conveyed to my family in Romania, for all the moral support they provided during the past years.

My dear wife Diana, I dedicate this thesis to you, for your love, care, support and patience. I promise that after completing this work we will have more time to explore the beauties of our country.

Cazimir Gabriel Bostan
 Enschede, January 2005